



GARCIA

Center for Polymers at
Engineered Interfaces() {
Stony Brook University
};

2021



Research Scholars



Foreword:

Each summer the Garcia Center holds a design competition for the logo which best represents the students for that summer. This year the students selected this composition which best illustrates the world opening up to them after the abrupt closure due to the Covid pandemic. Pictured are a microscope and test tube, symbolizing hands on

research, for those fortunate few students were able to come in person, while the computer screen paid tribute to the large majority of students which were still only able to participate virtually. In this hybrid learning mode, the students divided their efforts efficiently, where the characters within the screen represent machine learning programs, popular with the students at the remote locations. The Logo was designed by Leann Tai who wrote: *"... By thinking out of the box and integrating both digital and in-person components, Garcia 2021 will always be one of the most memorable experiences of our lives. From computer simulations to laboratory experiments and everything in between, we were able to explore a variety of fields in materials sciences. Thank you to Garcia, which gifted us with irreplaceable knowledge, experiences, and opportunities."*

We are very proud of our students, who used this summer to build friendships, forge international collaborations, and through outstanding team work produce a significant body of research with impact on mobility devices for the handicapped, deep fake video detection, explaining and possibly remediating Covid induced thrombogenesis, sustainable energy generation, and many more outlined in this book of abstracts.

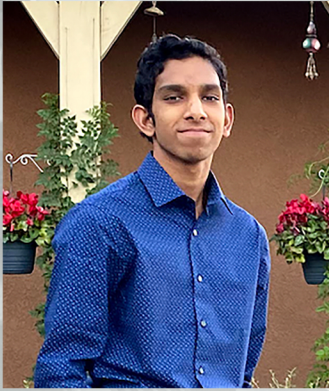
The Garcia Center for Polymers at Engineered Interfaces was founded in 1996 and is named after the late Queens College professor, Narciso Garcia, who was a pioneer in the integration of education and research. The Center focuses on the broad application of materials research to engineering, medicine, energy, nanocomposites, additive manufacturing, and recently, AI and machine learning. The Center also supports innovation through entrepreneurship and has multiple collaborations with industry and national laboratories: <https://www.stonybrook.edu/commcms/garcia/>. In the research program, high school students work together with undergraduates, PhD , post PhD and faculty who collaborate in addressing challenges at the cutting edge of modern science. The students are encouraged to publish in refereed scientific journals, present their results at national conferences, and develop patents to protect their intellectual property. Our goal is to convey to the students the excitement we enjoy daily in research and provide for them a supportive network within the scientific community. Research is a lifelong experience and we hope to remain a resource to our students long after "graduation".

Sincerely,

Miriam H. Rafailovich and
Co-Directors, Garcia Center

Jonathan Sokolov

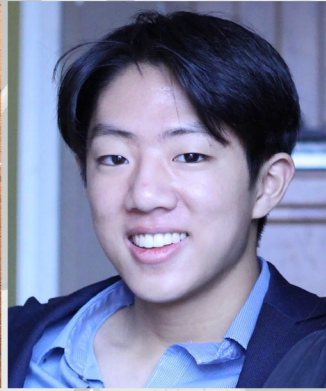
High School Students



Agarwal, Yash



Agrawal, Ayush



Ahn, Andrew



Alam, Sabreen



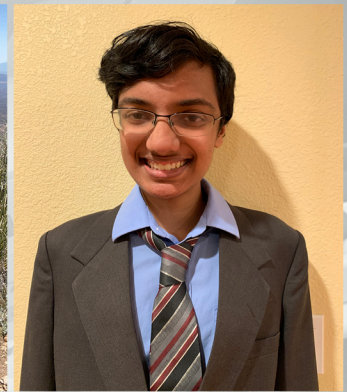
Alao, Ifeoluwatobi



Baratta, Leigh



Basu, Neha



Bharadwaj, Anirudh



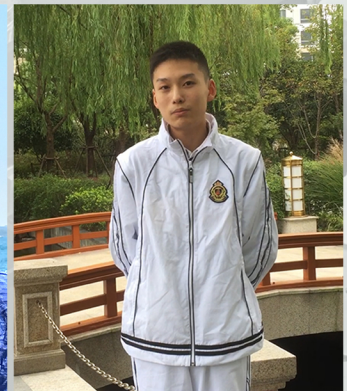
Cai, Sophia



Cheng, Shiqi



Dhori, Aishik



Dong, Sicheng



Dong, Tianyu (Tina)



Flickinger, Erika



Gabriel, Nicole

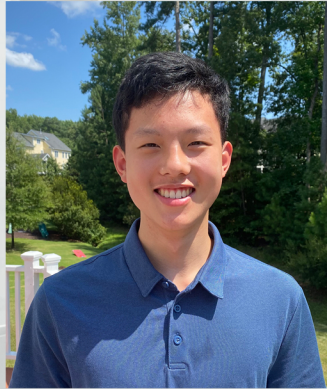


Garcia, Matthew

High School Students



Ghosh Dastidar, Prabuddha



Guan, Eric



Guo, Jessica



Ho-Chen, Forest



Hofflich, Dyllan



Hong, Qianhui



Hurwitz, Rebecca



Jain, Krish



Kaplan, Josh



Kugler, Jack



Kurtulus, Emirhan



Li, Joanna



Liao, Yifan



Lim, Chloe



Lim, Matt



Liu, Qiaru

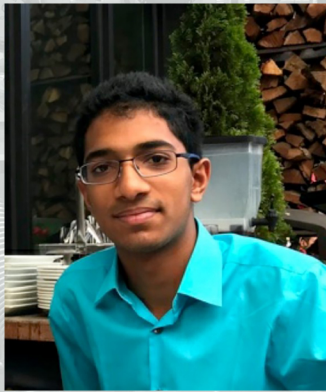
High School Students



Liu, Shuhe



Liu, Yaqi Lydia



Lolla, Satvik



Luo, Steven



Madabhushi, Abhinav



Malik, Raaghav



Mehrotra, Aarushi



Mehta, Nikhil



Morse, Katherine (Lulu)



Mosca, Chiara



Moskowitz, Adin



Noy, Eyal



Pereira, Ethan



Popova, Katerina



Ramrajvel, Nathra



Reinholdt, Timothy

High School Students



Reiss, Ezra



Richter, Claire



Rosovsky, Mira



Roy, Aryan



Saks, Hannah



Savov, Emma



Shaffer, Layla



Sheth, Aayush



Shnyder, Justin



Strutton, Will



Sun, Jia Lu (Angela)



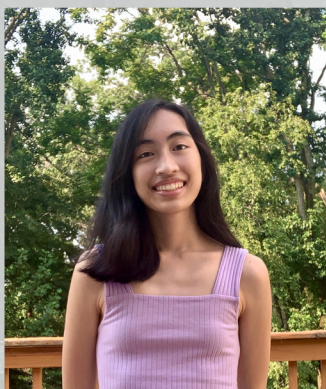
Sunder, Sneha



Tai, LeAnn



Tam, Albert



Tao, Hannah



Tarrab, David

High School Students



Vangipuram, Abhishek



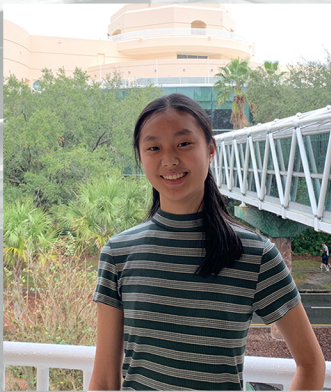
Vaysman, Emily



Vendhan, Maya



Wang, Elizabeth



Wang, Grace



Wang, Lydia



White, Francis



Wong, Audrey



Wong, Grace Kyoko



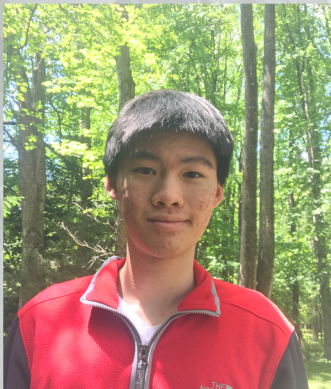
Wong, Jansen



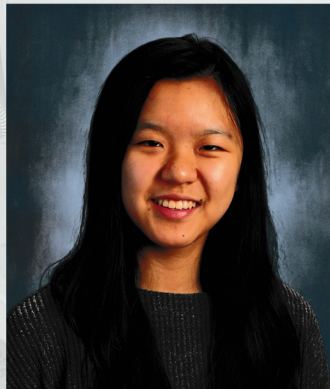
Xiao, Emily



Xie, Daniel



Xie, Junzhi



Xiong, Robin



Xu, Haojun (Amanda)



Yang, Claire

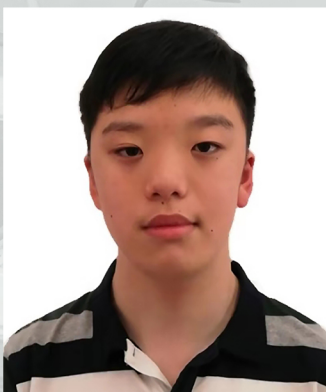
High School Students



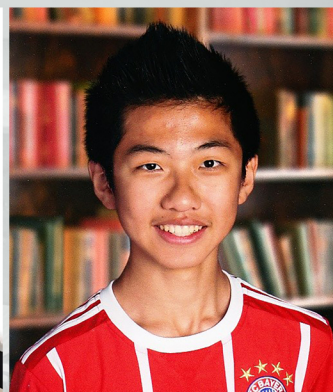
Yang, Serena



Yu, Lauren



Yuan, Ivan



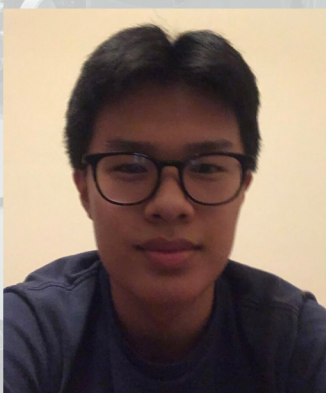
Yuen, Andrew



Zerykier, Jacob



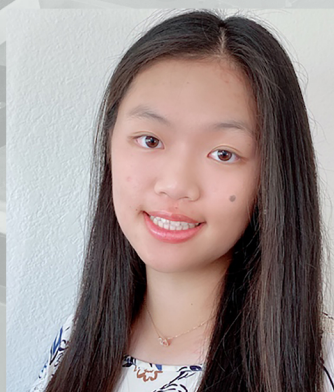
Zhan, Jiner



Zhang, Alex



Zhang, Elizabeth



Zhou, Emily



Zhou, Leon Lee



Zhu, Alan



Zhu, Eric



Zhu, Guanchen



Zu, Wenxu



Zuo, Ethan

Research Experience for Undergraduates (REUs)



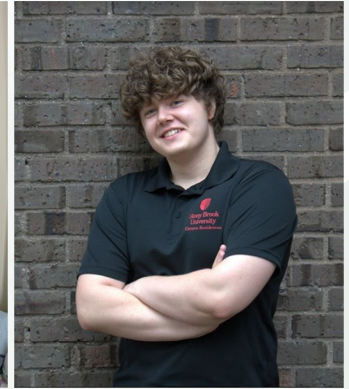
Calderon, John



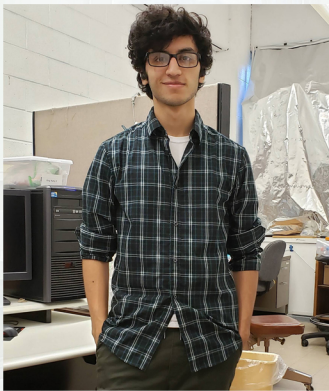
Chavre, Bharvi



Cho, Anna



Christie, Olias



Del Valle, Anthony



Deluxe, Tony



Essuman, Bernard



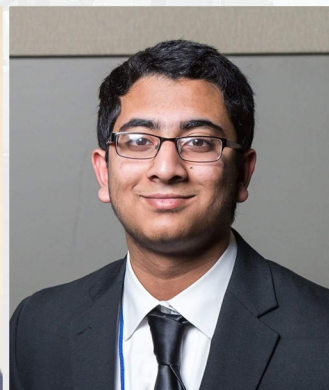
Gopal, Megha



Lone, Ayman



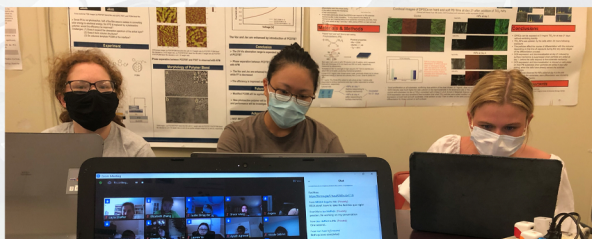
Max, Rena



Nimmagadda, Varun



Patel, Krish



Research Experience for Undergraduates (REUs)



Persaud, Vikash



Rai-Gersappe, Diya



Rosshirt, Hugh



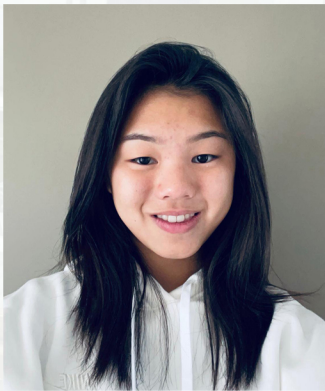
Rosshirt, Kathryn



Shern, Tyler



Um, Christopher



Wang, Annie



Zhang, Jeffrey



Graduate Students



Agrawal, Shubham



Chaturvedi, Nilesh



Fang, Haoyan



Fang, Yiwei



Fu, Shi



Hofflich, Jessica



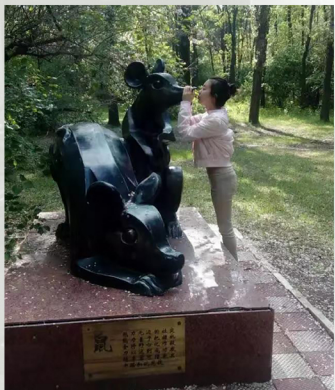
Lee, Wonil



Li, Kao



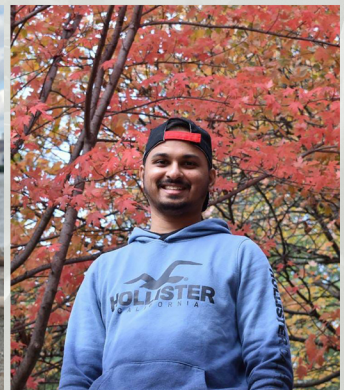
Lin, Yu-Chung



Liu, Haijiao



Mahalingam, Dasharadhan



Raut, Aniket



Saha, Shoumik



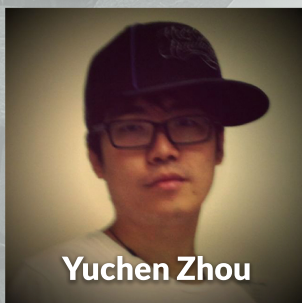
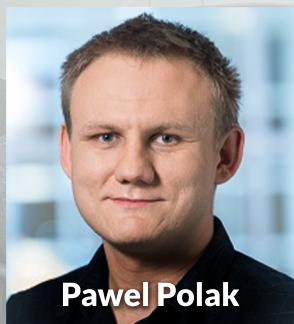
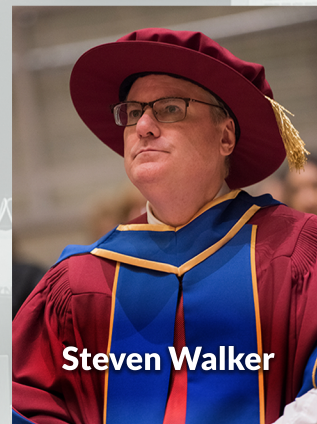
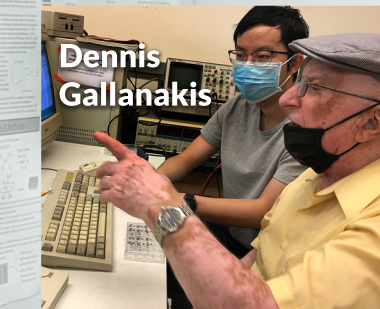
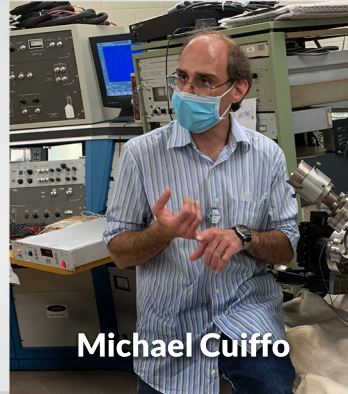
Wong, Robert



Yin, Yifan



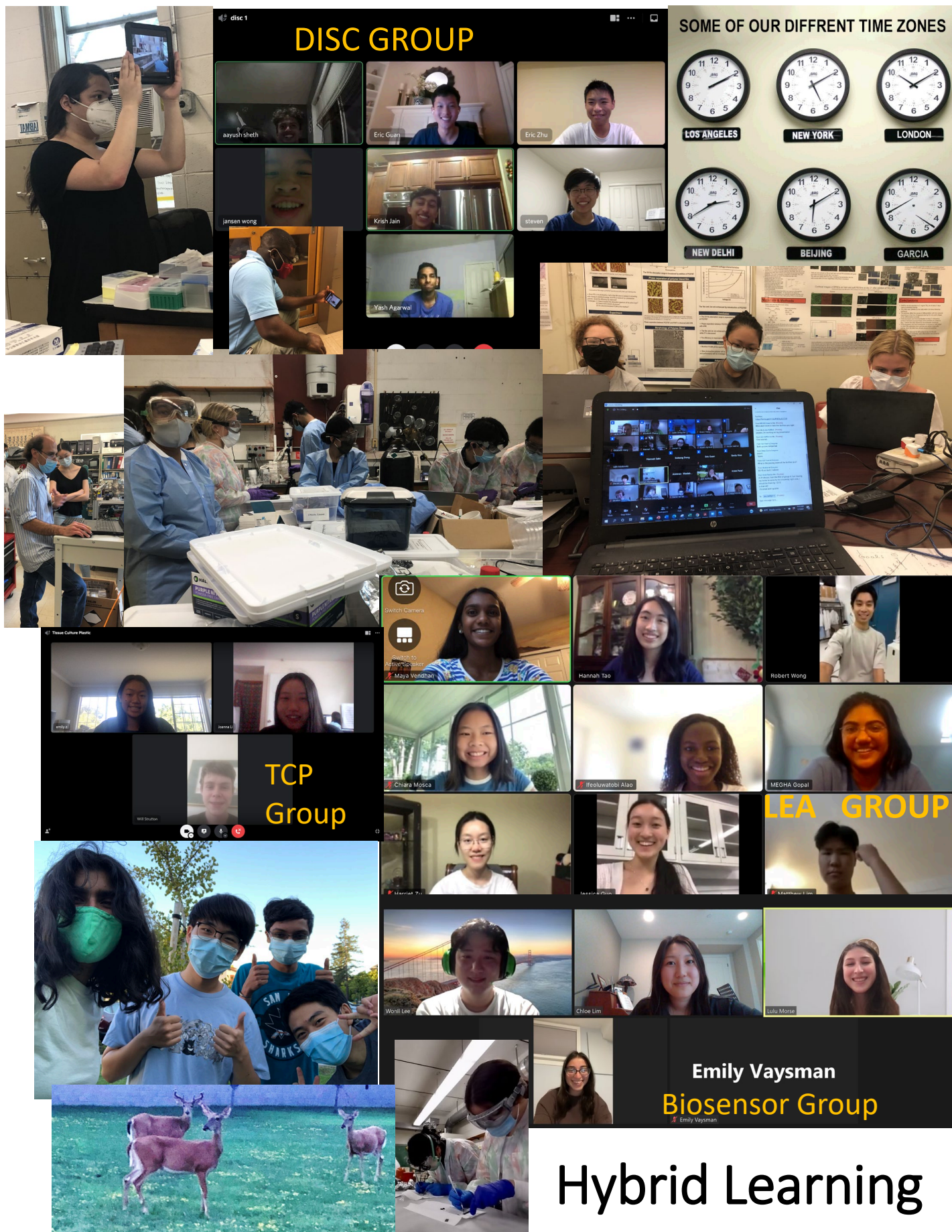
Faculty & Staff



Guest Speakers!

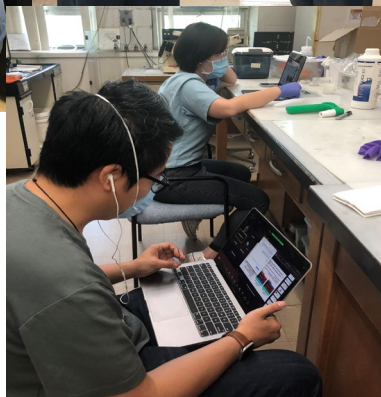


And many, many more!





Working
together &
with those
on line





Total Fun





Summer Scholar Schedule of Weekly Activities

Each day starts with a mandatory group meeting at 10 AM!


Daily Schedule: Week of 6/28

Monday – 6/28	Tuesday – 6/29	Wednesday – 6/30	Thursday – 7/1	Friday – 7/2																																																																
<p>10:00-10:15: Professor, Frank H. Wu, President of Queens College – Welcome to Garcia</p> <p>10:15-11:00: Introduction to the Garcia Program: Dr. Ann-Marie Scheidt, Director of Economic Development, Garcia Staff and Students</p> <p>11:00-12:00 Feini (Sylvia) Qu, VMD, PhD, (and her high school students), Washington State Regenerative Medicine</p> <p>12:00-1:00: Lunch break</p> <p>1:00-2:00: Dalia Leibowitz, R&D Engineer, Metronic, + interns: GYN surgical group</p> <p>2:00-3:00: Prof. Pawel Polak, Applied Math and Statistics, Stony Brook</p> <p>3:00-4:00: Sunny Tang (LIJ) "Rise of the Machines: Technology and Artificial Intelligence in psychiatry"</p>	<p>10:00-10:30: NetID & Technical Issues – Jessica Hofflich</p> <p>10:30-12:00: Biological Hazards; Bloodborne Pathogens; Managing Biological Waste; Working in a BSL-2 Enclosure – Chris Kuhlow</p> <p>12:00 – 12:30: Lunch</p> <p>12:30-1:00: Bernard Essuman: Simulation of Fibrinogen</p> <p>1:00 – 2:00: Philip Ball: Reporting Science</p> <p>2:00 – 3:00: Peng Zhang: Modeling the Coronavirus and Other Biological Systems</p> <p>3:00 – 4:00: Dmitris Assanis: The Science of Combustion</p>	<p>10:00 – 10:15: Mr. Steve Vacarelli, Morin Foundation Trust</p> <p>10:15 – 12:00: Drs. Ying Liu & Sandhiya Muralidharan, EH&S: Hazardous Chemical Disposal and Handling</p> <p>12:00 – 12:30: Lunch</p> <p>12:30 – 1:30: Dr. Gurtej Singh, Department of Plastic Surgery: Autologous Bioengineering</p> <p>1:30 – 2:30: Dr. Chang-Yong Nam, Brookhaven National Laboratory: Center for Functional Materials</p> <p>2:30 – 3:15: Eric Petersen: Biomedical Imaging</p> <p>3:15 – 4:00: Mrs. Rebecca Isseroff, Lawrence High School – Good Lab Notebooks, MRS, & Graphene</p>	<p>10:00 – 10:15: Organizational Meeting</p> <p>10:15 – 10:30: Dr. Ying Liu, EH&S – Hazardous Waste Handling Quiz (Kahoot)</p> <p>10:30 – 11:30: Yuet (Claire) Tran – Stony Brook University Library Resources</p> <p>11:30 – 12:30: Professor Marcia Simon, SBU School of Dental Medicine</p> <p>12:30 – 1:00: Lunch</p> <p>1:00 – 2:00: Professor Jonathan Sokolov, Department of Materials Science & Chemical Engineering</p> <p>2:00 – 3:00: Professor Eyal Zussman</p> <p>3:00 – 4:00: Professor Brooke Ellison</p>	<p>10:00 – 10:30: Jacob Meyers, Working in Garcia 2020</p> <p>10:30 – 11:15: Professor Dilip Gersappe, Department of Materials Science and Chemical Engineering</p> <p>11:15 – 12:00: Professor Steven Walker</p> <p>12:00 – 12:30: Lunch</p> <p>12:30 – 4:00: Facilities Tour</p> <table><tr><th>Time</th><th>Facility</th><th>Presenter</th><th>Room</th></tr><tr><td>12:30</td><td>3D Printer/ Fiber Extrusion</td><td>Yu-Chung</td><td>211</td></tr><tr><td>12:40</td><td>AFM</td><td>Haijiao</td><td>211</td></tr><tr><td>12:50</td><td>Fuel Cell/ Raman</td><td>Aniket</td><td>211</td></tr><tr><td>13:00</td><td>Zeta/UV-Vis/UV-Ozone</td><td>Fan</td><td>211</td></tr><tr><td>13:10</td><td>Cell Lab</td><td>Kuan-Che</td><td>H253</td></tr><tr><td>13:20</td><td>Rheometer</td><td>Robert</td><td>H251</td></tr><tr><td>13:30</td><td>DSC</td><td>Robert</td><td>H251</td></tr><tr><td>13:40</td><td>LB</td><td>Haoyan</td><td>H251</td></tr><tr><td>13:50</td><td>EVOS</td><td>Shi Fu</td><td>H249</td></tr><tr><td>14:00</td><td>Bioprinting</td><td>Olias</td><td>H249</td></tr><tr><td>14:10</td><td>FTIR/XPS/XRF</td><td>Mike</td><td>309</td></tr><tr><td>14:20</td><td>Contact angle</td><td>Kao</td><td>205</td></tr><tr><td>14:30</td><td>Instron/molding</td><td>Yiwei</td><td>205</td></tr><tr><td>14:40</td><td>Chemical Hood/Waste/313</td><td>Yifan</td><td>313</td></tr><tr><td>14:50</td><td>BNL/PVD</td><td>Yuchen</td><td>remote</td></tr></table>	Time	Facility	Presenter	Room	12:30	3D Printer/ Fiber Extrusion	Yu-Chung	211	12:40	AFM	Haijiao	211	12:50	Fuel Cell/ Raman	Aniket	211	13:00	Zeta/UV-Vis/UV-Ozone	Fan	211	13:10	Cell Lab	Kuan-Che	H253	13:20	Rheometer	Robert	H251	13:30	DSC	Robert	H251	13:40	LB	Haoyan	H251	13:50	EVOS	Shi Fu	H249	14:00	Bioprinting	Olias	H249	14:10	FTIR/XPS/XRF	Mike	309	14:20	Contact angle	Kao	205	14:30	Instron/molding	Yiwei	205	14:40	Chemical Hood/Waste/313	Yifan	313	14:50	BNL/PVD	Yuchen	remote
Time	Facility	Presenter	Room																																																																	
12:30	3D Printer/ Fiber Extrusion	Yu-Chung	211																																																																	
12:40	AFM	Haijiao	211																																																																	
12:50	Fuel Cell/ Raman	Aniket	211																																																																	
13:00	Zeta/UV-Vis/UV-Ozone	Fan	211																																																																	
13:10	Cell Lab	Kuan-Che	H253																																																																	
13:20	Rheometer	Robert	H251																																																																	
13:30	DSC	Robert	H251																																																																	
13:40	LB	Haoyan	H251																																																																	
13:50	EVOS	Shi Fu	H249																																																																	
14:00	Bioprinting	Olias	H249																																																																	
14:10	FTIR/XPS/XRF	Mike	309																																																																	
14:20	Contact angle	Kao	205																																																																	
14:30	Instron/molding	Yiwei	205																																																																	
14:40	Chemical Hood/Waste/313	Yifan	313																																																																	
14:50	BNL/PVD	Yuchen	remote																																																																	

Summer Scholar Schedule of Weekly Activities

Each day starts with a mandatory group meeting at 10 AM!

Daily Schedule: Week of 7/5

Monday – 7/5	Tuesday – 7/6	Wednesday – 7/7	Thursday – 7/8	Friday – 7/9
 <p>Happy Fourth of July! (Observed)</p>	<p>10:00-10:15: Organizational Meeting</p> <p>10:15-11:00: Dr. Hani Gnyem, Hebrew University</p> <p>11:00 – 11:45: Dr. Steven Larson, US Army Corps of Engineers</p> <p>11:45 – 12:30: Professor Steven Schwarz, Queens College – Spin Casting Fundamentals</p> <p>12:30 – 1:00: Lunch</p> <p>1:30 – 4:00: Journal Club Presentations</p>	<p>10:00 – 10:30: Profs. Allan Kucine, Ann Nasti, & Ife Onyenekwu, School of Dental Medicine Programs</p> <p>10:30 – 11:00: Safety/Facilities Quizzes</p> <p>11:00 – 11:30: Introduction to Spin Casting Experiment</p> <p>12:30 – 12:30: Dr. Chandramouli, Development of Liquid Embolic Agent Projects</p> <p>12:30 – 4:00: Polystyrene Recycling Spin Casting Experiment (multiple stations)</p>	<p>10:00 – 4:00: Polystyrene Recycling Spin Casting Experiment (continued) – Data Collection and Analysis</p>	<p>10:00 – 10:30: Statistical Analysis of Experimental Data</p> <p>10:30 – 11:30: Professor Nilanjan Chakraborty (Robotic Arm Project)</p> <p>11:30 – 12:30: Zhi Li & Wenzhe Cui (Eye Gaze)</p> <p>12:30 – 1:00: Wilson Lee, Estée Lauder</p> <p>1:00 – 1:30: Lunch</p> <p>1:30 – 2:30: Professor Marcia Simon, Dental Pulp Stem Cells</p> <p>2:30 – 3:30: Professor Jonathan Sokolov, Surface DNA Projects</p> <p>3:30 – 4:00: Polystyrene Recycling Spin Casting Experiment Wrap-Up</p>



Summer Scholar Schedule of Weekly Activities

Each day starts with a mandatory group meeting at 10 AM!

Daily Schedule: Week of 7/12


Monday – 7/12	Tuesday – 7/13	Wednesday – 7/14	Thursday – 7/15	Friday – 7/16
<p>10:00-10:30: Dr. Jack Fuhrer, Programs at Stony Brook University, Renaissance School of Medicine</p> <p>10:30-11:00: Professor Gary Halada, Department of Materials Science and Chemical Engineering</p> <p>11:00-12:00: Spin Casting Presentations Groups 1-5</p> <p>12:00-1:00: Lunch break</p> <p>1:15-3:00: Professor Jon Sokolov – DNA Projects</p> <p>3:00 – 4:00: Priyanka Sharma, Nanocellulose</p>	<p>10:00-10:45: Spincasting Presentations Groups 6-8 + Discussion</p> <p>10:45 – 11:15: Gurtej Singh & Shi Fu – Autologous Constructs</p> <p>11:45-12:15: Kuan-Che & Haijiao – Plaque Assays and Neurogenesis</p> <p>12:15-12:45: Lunch</p> <p>12:45-1:15: Fan Yang – DISC & Dental Pulp Stem Cells</p> <p>1:15-1:45: Yu-Chung Lin - X-ray scattering and FDM printing</p> <p>1:45-2:15: Robert Wong – Hydrogels</p> <p>2:15-2:45: Yiwei Fang – Nanocomposites</p> <p>3:30-4:00: Kao Li – P12 and Covid thrombogenesis</p>	<p>10:00 – 10:15: Organizational Meeting</p> <p>10:15 – 12:00: Dr. Ying Liu, EH&S: Correctly writing an SOP</p> <p>10:45 – 11:15: Projects with Dr. Pawel Polak: Facial Recognition</p> <p>11:15 – 11:45: Aniket & Haoyan – Hydrogen & Anionic Fuel Cells</p> <p>12:15 – 12:30: Gersappe Group – Theory and Modeling</p> <p>12:30 – 1:00: Lunch</p> <p>1:00 – 2:00: Dr. Sergei Levchik: Flame Retardant Materials</p> <p>2:00 – 2:30: Dr. Peng Zhang, Dr. Yuefan Deng – Computational Modeling</p>	<p>10:00 – 11:00: Announcement of project topics</p> <p>11:00 – 12:30: Project discussions in breakout rooms</p> <p>12:30 – 1:00: Lunch</p> <p>1:00 – 4:00: Writing SOPs in respective topic breakout rooms</p>	<p>10:00 – 11:00: Todd Dickson – Career Center</p> <p>11:00 – 11:30: Dr. Nadine Pernodet – Estée Lauder Skin Research</p> <p>11:30 – 11:45: Short Research Updates:</p> <p>Tony Deluxe – 15-Year-Old Bacteria</p> <p>Jessica Guo – Ethical Engineering</p> <p>11:45 – 2:00: Work!</p>



Summer Scholar Schedule of Weekly Activities

Each day starts with a mandatory group meeting at 10 AM!

Daily Schedule: Week of 7/19

Monday – 7/19	Tuesday – 7/20	Wednesday – 7/21	Thursday – 7/22	Friday – 7/23
<p>10:00 – 10:15: Organizational Meeting</p> <p>10:15 – 11:00: Dr. Richard Clark, MD – Departments of Dermatology and Biomedical Engineering</p> <p>11:00 – 4:00: Work! (According to your group's schedule)</p>	<p>10:00 – 10:10: Organizational Meeting</p> <p>10:10 – 11:00: Aaron Slutsky – Biopolymers</p> <p>11:00 – 11:30: Dr. David Sprouster – Micro- CT Analysis</p> <p>11:30 – 4:00: Work! (According to your group's schedule)</p>	<p>10:00 – 10:10: Organizational Meeting</p> <p>10:10 – 11:00: Professor Chulsung Bae</p> <p>11:00 – 11:30: Dr. David Sprouster – X-ray Materials Analysis: Porosity</p> <p>11:30 – 4:00: Work! (According to your group's schedule)</p>	<p>10:00 – 10:10: Organizational Meeting</p> <p>10:10 – 11:00: Professor Gordon Taylor</p> <p>11:00 – 11:50: Fred Weibke – TA Instruments – Tutorial for using the TRIOS rheometer software</p> <p>12:00 – 4:00: Work! (According to your group's schedule)</p>	<p>10:00 – 10:10: Organizational Meeting</p> <p>10:10 – 11:00: Short Research Updates: Dr. Cuiffo's Cellulose Fiber Group</p> <p>Shi Fu and Dr. Singh's Angiogenesis Group</p> <p>Bernard Essuman's Modeling and Simulation Group</p> <p>11:00 – 2:00: Work! (According to your group's schedule)</p> <p>12:00 – 2:00: Annual Garcia Barbecue! (In-Person)</p> 



Summer Scholar Schedule of Weekly Activities

Each day starts with a mandatory group meeting at 10 AM!


Daily Schedule: Week of 7/26

Monday – 7/26	Tuesday – 7/27	Wednesday – 7/28	Thursday – 7/29	Friday – 7/30
<p>10:00 – 10:10: Organizational Meeting</p> <p>10:15 – 11:00: Dr. Tai-De Li – Advanced Science Research Center</p> <p>11:00 – 4:00: Work! (According to your group's schedule)</p> <p>12:00 – 12:30: TTK Group Meeting with Dr. Brooke Ellison and Greg Blanchard</p>	<p>10:00 – 10:05: Organizational Meeting</p> <p>10:05 – 11:00: Donna Tuminello – Defining and Protecting Intellectual Property</p> <p>11:00 – 11:30: Professor Chang -Yong Nam – Electron Microscopy</p> <p>12:00 – 12:50: Professor Ralph Colby</p> <p>12:50 – 4:00: Work! (According to your group's schedule)</p>	<p>10:00 – 10:10: Organizational Meeting</p> <p>10:10 – 11:00: Professor Rina Tannenbaum, Department of Materials Science and Chemical Engineering</p> <p>11:00 – 4:00: Work! (According to your group's schedule)</p>	<p>10:00 – 10:15: Organizational Meeting</p> <p>10:15 – 10:45: Dr. Michelle Hutchings, Vagelos Integrated Program in Energy Research, University of Pennsylvania</p> <p>10:45 – 11:15: Professor Marcia Simon – Explaining RT-PCR</p> <p>11:15 – 4:00: Work! (According to your group's schedule)</p>	<p>10:00 – 10:15: Group Video Presentations 1-3</p> <p>10:15 – 10:30: Short Research Update: Kao Li's P12 and Thrombogenesis Group</p> <p>10:30 – 10:45: Group Video Presentations 4-6</p> <p>10:45 – 2:00: Work! (According to your group's schedule)</p>

Summer Scholar Schedule of Weekly Activities

Each day starts with a mandatory group meeting at 10 AM!

Daily Schedule: Week of 8/2


Monday – 8/2	Tuesday – 8/3	Wednesday – 8/4	Thursday – 8/5	Friday – 8/6
<p>10:00 – 10:30: Hybrid Group Picture (Engineering Lobby)</p> <p>10:30 – 11:30: Professor Carlos Simmerling – Modeling and Simulation</p> <p>11:30 – 11:40: Group Video Presentations 7, 8, & 10</p> <p>11:40 – 4:00: Work! (According to your group's schedule)</p> <p>6:00 – 8:00PM Sunset Dinner and Fishing Excursion! (Osprey – Port Jefferson)</p> 	<p>10:00 – 10:05: Organizational Meeting</p> <p>10:05 – 10:20: Interim Dean Jon Longtin, College of Engineering and Applied Sciences</p> <p>10:20 – 11:20: Dr. Stoyan Bliznakov</p> <p>11:20 – 4:00: Work! (According to your group's schedule)</p>	<p>10:00 – 10:30: Marla Boots – Submitting to the Materials Research Society (MRS) Meeting</p> <p>10:30 – 11:00: Short Research Updates: Dr. Polak's DISC Group Dr. Chakraborty's Robotic Arm Group Claire Yang – Laser Teaching Center</p> <p>11:00 – 4:00: Work! (According to your group's schedule)</p>	<p>10:00 – 10:20: Timothy Hart – Engineer at Beyond Meat & Garcia Alumnus</p> <p>10:20 – 10:30: Short Research Update: Professor Gersappe's Theory & Modeling Group</p> <p>10:30 – 10:45: Composing an Abstract & Preparing for the Garcia Symposium</p> <p>10:45 – 4:00: Work! (According to your group's schedule)</p>	<p>10:00 – 10:15: Organizational Meeting</p> <p>10:15 – 11:00: Short Research Updates: Yiwei's Flame Retardant Nanocomposites Group Yu-Chung's Printable Polymer Blends Group Aniket and Haoyan's Fuel Cell Groups</p> <p>11:00 – 2:00: Work! (According to your group's schedule)</p>



Summer Scholar Schedule of Weekly Activities

Each day starts with a mandatory group meeting at 10 AM!

Daily Schedule: Week of 8/9

Monday – 8/9	Tuesday – 8/10	Wednesday – 8/11	Thursday – 8/12	Friday – 8/13
<p>10:00 – 10:15: Selection of 2021 Logo</p> <p>10:15 – 11:00: Short Research Updates: Won-Il's Biosensor Group Yuchen and Yifan's Perovskite Group</p> <p>11:00 – 4:00: Work! (According to your group's schedule)</p> <p>Abstracts due at 11:59PM!</p>	<p>10:00 – 10:05: Organizational Meeting</p> <p>10:05 – 10:20: Revised Video Presentation Screenings</p> <p>10:20 – 11:00: Short Research Updates: Peng Zhang's Computational Modeling Groups Kuan-Che's Plaque Assay Group Haijiao's Neurogenic Differentiation Group</p> <p>11:00 – 4:00: Work! (According to your group's schedule)</p>	<p>10:00 – 10:10: Organizational Meeting</p> <p>10:30 – 11:00: Short Research Updates: Shi Fu's Dental Pulp Stem Cell Group Robert's Liquid Embolic Agent Group Tony Deluxe – Ancient Bacteria</p> <p>11:00 – 4:00: Work! (According to your group's schedule)</p> <p>Symposium Presentations due at 11:59PM!</p>	<p>10:00 – 10:20: Organizational Meeting</p> <p>10:20 – 10:30: Short Research Updates: Dr. Brooke Ellison's Ethical Engineering Projects Fan's RDP Group & Bioreactor Group</p> <p>10:30 – 4:00: Work! (According to your group's schedule)</p>	<p>9:15 – 11:30:</p>  <p>Garcia 2021 Virtual Research Symposium!</p>



Please join us
for the **Summer 2021**
Research Symposium
& Musical Arrangement
(Vivaldi Spring Movement)
on
Friday August 13
from
9:15 - 11:30 AM EST
Via Zoom

<https://bit.ly/garciasymposium21>

Questions/zoom problems— email garciareserach@stonybrook.edu
Sponsored by **the Louis Morin Charitable Trust**

The Garcia Research Scholar Program



Explanation of Logo Design: "While Garcia 2021 may be different than what we desired, it is no doubt that the program was nothing but successful. By thinking out of the box and integrating both digital and in-person components, Garcia 2021 will always be one of the most memorable experiences of our lives. From computer simulations to laboratory experiments and everything in between, we were able to explore a variety of fields in materials sciences. Thank you to Garcia, which gifted us with irreplaceable knowledge, experiences, and opportunities."

Leann Tai '21

9:15AM	Welcome Mr. Steve Vacarelli, Brown Bros Harriman and the Morin Charitable Trust
9:19AM	Musical Arrangement: "Vivaldi's Spring Movement" Prof. John Luckner Jerome and the Garcia 2021 Orchestra Arrangement: Jamie Jerome
9:24-9:25AM	Opening Remarks Dr. Brooke Ellison, Center for Medical Humanities, Compassionate Care, and Bioethics
9:25-9:29AM	Symposium X: Ethical Engineering Chair: Jessica Guo, Ward Melville High School, East Setauket, NY
1 min	Ethical Analysis of the 2019-21 Locust Epidemic Anirudh Bharadwaj , Lynbrook High School, San Jose, CA Justin Shnyder , Staten Island Technical High School, Staten Island, NY Jansen Wong , Great Neck South High School, Great Neck, NY Alan Zhu , Livingston High School, Livingston, NJ
1 min	Infodemic: Misinformation in the Age of COVID-19 Steven Luo , Evergreen Valley High School, San Jose, CA Jessica Guo , Ward Melville High School, East Setauket, NY Sneha Sunder , Fairfield Warde High School, Fairfield, CT Jacob Zerykier , Rambam Mesivta-Maimonides High School, Lawrence, NY Junzhi Xie , Richard Montgomery High School, Rockville, MD Matt Lim , Plainview-Old Bethpage JFK High School, Plainview, NY
1 min	Self-Driving Cars: A Moral Dilemma Andrew Ahn , Fayetteville-Manlius High School, Manlius, NY Eric Guan , North Carolina School of Science and Mathematics, Durham, NC Joshua Kaplan , The Frisch School, Paramus, NJ Lauren Yu , Brea Olinda High School, Brea, CA

9:30-9:39AM	Session I: The Influence of Nanoparticles on Human Cells: Chairs: Diya Rai-Gersappe, Vassar University Bharvi Chavre, Princeton University
6 min	The Impact of TiO ₂ on the Network Mechanics of HUVEC The Effect of Titanium Dioxide on Cell Survival , Proliferation and Bacterial Infection Impact of SynOss on the Doubling Time of Dental Pulp Stem Cells Sabreen Alam , Portola High School, Irvine, CA Prabuddha Ghosh Dastidar , North Carolina School of Science and Mathematics, Durham, NC Mira Rosovsky , SAR High School, Riverdale, NY Elizabeth Wang , BASIS Chandler, Chandler, AZ Daniel Xie , Panther Creek High School, Cary, NC
2 min	The Influence of TiO ₂ and ZnO Nanoparticles on the Bacterial Infection of HeLa Cells Joanna Li , Townsend Harris High School, Flushing, NY William Strutton , Hastings High School, Hastings on Hudson, NY Emily Zhou , The Harker School, San Jose, CA
9:40-9:45AM 1 min	Session II: Differentiation of Dental Pulp Stem Cells Chair: Ayman Lone, University of Chicago
2 min	The Effect of Hypochlorous on the Migration and Differentiation of Dental Pulp Stem Cells Sabreen Alam , Portola High School, Irvine, CA Prabuddha Ghosh Dastidar , North Carolina School of Science and Mathematics, Durham, NC Mira Rosovsky , SAR High School, Riverdale, NY Elizabeth Wang , BASIS Chandler, Chandler, AZ Daniel Xie , Panther Creek High School, Cary, NC

2 min	<p>The Effect of Surface Chemistry on Dental Pulp Stem Cells in Neurogenic Differentiation</p> <p>Leigh Baratta, Smithtown High School East, Smithtown, NY Nikhil Mehta, Smithtown High School East, Smithtown, NY Claire Richter, South Side High School, Rockville Centre, NY Layla Shaffer, The Lawrenceville School, Lawrenceville, NJ Andrew Yuen, Jericho High School, Jericho, NY</p>
9:46-9:54AM 2 min	<p>Session III: Machine Learning and Artificial Intelligence</p> <p>Co-Chairs: Rena Max, Midreshet Lindenbaum Hugh Rosshirt, University of Notre Dame</p>
2 min	<p>Deepfake Video Detection Using Biologically Inspired Geometric Deep Learning</p> <p>Yash Agarwal, Dougherty Valley High School, San Ramon, CA Eric Guan, North Carolina School of Science and Mathematics, Durham, NC Krish Jain, Redmond High School, Redmond, WA Steven Luo, Evergreen Valley High School, San Jose, CA Aayush Sheth, Tesla STEM High School, Redmond, WA Jansen Wong, Great Neck South High School, Great Neck, NY Eric Zhu, Princeton High School, Princeton, NJ</p>
2 min	<p>Creating an Interface for the Operation of a Robotic Arm</p> <p>Matthew Garcia, Plainedge High School, North Massapequa, NY Dyllan Hofflich, Pelham Memorial High School, Pelham, NY David Tarrab, Ramaz Upper School, New York, NY Audrey Wong, Beckman High School, Irvine, CA Lauren Yu, Brea Olinda High School, Brea, CA</p>
2 min	<p>Implementation of TTK for Control of Multiple Devices</p> <p>Ezra Reiss, Hebrew Academy of Nassau County, Uniondale, NY Ethan Pereira, West Windsor-Plainsboro High School North, Plainsboro Township, NJ Adin Moskowitz, Hebrew Academy of Nassau County, Uniondale, NY</p>

9:55-10:06AM 1 min	Session IV: Thrombosis and Viral Infection Chair: Katie Rosshirt, University of Notre Dame
4 min	Investigating How COVID-19 Induces Microthrombosis on Endothelial Cells The Effectiveness of P12: A Potential Anti-Thrombogenic Drug for COVID-19 Nicole Gabriel , South Side High School, Rockville Centre, NY Aarushi Mehrotra , Lynbrook High School, Lynbrook, NY Jia Lu (Angela) Sun , Lord Byng Secondary, Vancouver, Canada Sneha Sunder , Fairfield Warde High School, Fairfield, CT Serena Yang , Dougherty Valley High School, San Ramon, CA
2 min	Investigating the Atomistic Mechanism of Fibrinogen Inhibition by P12 Sophia Cai , Barrington High School, Barrington, IL LeAnn Tai , Arnold O. Beckman High School, Irvine, CA
2 min	Science At-Home Experiment Video 1
10:08-10:21AM 1 min	Session V: Modeling and Experiment of SARS-CoV-2 Spike Proteins Under Different Conditions Chair: Bernard Essuman, Stony Brook University
2 min	Influence Of Temperature, And Salt Concentration On Molecular Structure Of SARS-Cov-2 Spike Protein Using Potentiometric Sensor Emily Vaysman , Hebrew Academy of the Five Towns and Rockaway, Lawrence, NY Katherine Morse , Hebrew Academy of the Five Towns and Rockaway, Lawrence, NY Chloe Lim , Portola High School, Irvine, CA
2 min	Evaluating the Effectiveness of AI-Guided Coarse-Grained Modeling for More Efficient Molecular Dynamics Simulations Raaghav Malik , Columbus Academy, Gahanna, OH

2 min	Protein-Ligand Binding Affinity Prediction by Multi-Representation based Neural Network Emirhan Kurtuluş , Cağaloğlu Anatolian High School, Istanbul, Turkey
2 min	Fogging H1N1 Virus to Quantify the Survival Rate on Various Surfaces Francis White , Houston Christian High School, TX Timothy Reinholdt , South Side High School, Rockville Centre, NY Qianhui Hong , Shenzhen Foreign Languages School, Shenzhen, China
2 min	Interactions of Polylactic Acid with the SARS-CoV-2 Spike Glycoprotein Under Varying Temperatures Erika Flickinger , Saint Teresa High School, Decatur, IL Rebecca Hurwitz , Maine East High School, Park Ridge, IL Lydia Wang , Great Neck South High School, Great Neck, NY
10:21-10:29 2 min	Session VI: Nanocomposites Co-Chairs: Anna Cho, Stony Brook University Vikash Persaud, Stony Brook University
2 min	Creating Easily Processable, 3D-printable, and Biodegradable Flame Retardant Polymers Joshua Kaplan , The Frisch School, Paramus, NJ Katerina Popova , Hackley School, Tarrytown, NY Ethan Zuo , Saratoga High School, Saratoga, CA Abhishek Vangipuram , Novi High School, Novi, MI Miffy Liu , Shenzhen Middle School, Shenzhen, China
2 min	Optimizing the PP/PS Blends for Conductive Polymer 3D Printing Forest Ho-Chen , George School, Newtown, PA Shuhe Liu , The Experimental High School Attached to Beijing Normal University, Beijing, China Emma Savov , Mainland Regional High School, Linwood, NJ
2 min	Implications of modifying the rheology of <i>Rhizobium tropici</i> EPS Grace Wang , Lexington High School, Lexington, MA Emily Xiao , Alexander Mackenzie High School, Richmond Hill, ON, Canada

10:30-10:41 2 min	Session VII: Nanocomposite Modeling & Simulation Chairs: Olias Christie, Stony Brook University Varun Nimmagadda, University of Michigan-Ann Arbor
2 min	Designing Copolymers for Reducing Interfacial Tension in Polymer Blends using Coarse-Grained Molecular Dynamics Albert Tam , Lynbrook High School, San Jose, CA Nathra Ramrajvel , Thomas Jefferson High School for Science and Technology, Alexandria, VA
2 min	Simulating the Transport of Ions in Solid Electrolytes Using the Lattice-Boltzmann Method Jack Kugler , Phillips Exeter Academy, Exeter, NH Aishik Dhor , Munster High School, Munster, IN Satvik Lolla , Poolesville High School, Poolesville, MD
2 min	Investigating the effect of interface morphologies on dendrite formation in lithium-metal batteries via the Lattice-Boltzmann Method Neha Basu , BASIS Scottsdale, Scottsdale, AZ Anirudh Bharadwaj , Lynbrook High School, San Jose, CA
2 min	Using Coarse-Grained Molecular Dynamics to Model Rheological Properties of Hydrogels with Rigid and Bonded Clay Fillers Varun Nimmagadda , University of Michigan, Ann Arbor, MI
2 min	Science At-Home Experiment Video 2
10:41-10:50 1 min	Session VIII: Microorganisms and Materials Chair: Antony Deluxe, NYU, College of Arts and Science
2 min	Analysis of microorganisms associated with failed in endodontic treatment in fifteen-year-old samples of root canals Antony Deluxe , New York University, College of Arts and Science, New York, NY

4 min	<p>Deweaving Cotton Cloth using Non-Toxic and Environmentally-Friendly Methods</p> <p>Functionalizing Fibers from Cotton Cloth Unweaved using Sodium Nitrate and Citric Acid Solutions</p> <p>Ayush Agrawal, Canyon Crest Academy, San Diego, CA Tianyu Dong, Northview High School, Johns Creek, GA Amanda Xu, The Madeira School, McLean, VA Ivan Yuan, Shanghai High School International Division, Shanghai, China Jacob Zerykier, Rambam Mesivta-Maimonides High School, Lawrence, NY Elizabeth Zhang, Phillips Academy Andover, Andover, MA Guanchen Zhu, The Experimental High School Attached to Beijing Normal University, Beijing, China</p>
2 min	Science At-Home Experiment Video 3
10:51-11:02 2 min	<p>Session IX: Embolic Agents, DNA, & Backscattering</p> <p>Co-Chairs: Anthony Del Valle, Stony Brook University Megha Gopal, Stony Brook University</p>
2 min	<p>Application of Tn5 Transposase to Surface-immobilized DNA Combed on Grated Polydimethylsiloxane Film</p> <p>Robin Xiong, Ward Melville High School, East Setauket, NY Hannah Saks, Walt Whitman High School, Huntington, NY Junzhi Xie, Richard Montgomery High School, Rockville, MD Leon Zhou, Shenzhen Middle School, Luohu District, Shenzhen, Guangdong Province, China</p>
2 min	<p>Observation of Coherent Backscattering for Detection of Physical State Changes</p> <p>Claire Yang, Ward Melville High School, East Setauket, NY</p>

2 min	<p>Optimizing Brain Aneurysm Treatment with a Reverse Thermo-Responsive Liquid Embolic Agent</p> <p>Ifeoluwatobi Alao, High Technology High School, Lincroft, NJ Jessica Guo, Ward Melville High School, East Setauket, NY Matt Lim, Plainview-Old Bethpage JFK High School, Plainview, NY Chiara Mosca, East Islip High School, Islip Terrace, NY Hannah Tao, Academy for Information Technology, Scotch Plains, NJ Maya Vendhan, Colorado Academy, Denver, CO Harriet Zu, High School Affiliated to Renmin University of China, Beijing Aryan Roy, Cherry Creek High School, Denver, CO</p>
2 min	Science At-Home Experiment Video 4
11:03-11:17 2 min	<p>Session X: Sustainable Energy</p> <p>Chair: John Calderon, Stony Brook University</p>
6 min	<p>Use of Partially Reduced Graphene Oxide to Increase Power Efficiency in AEM Fuel Cells</p> <p>The Enhancement of AEMFCs using Bimetallic Ag₃Ni and AgNi₃ Nanoparticles</p> <p>Optimization of Membrane Electrode Assembly Using Silver Nanoparticles in Anion Exchange Membrane Fuel Cells</p> <p>Andrew Ahn, Fayetteville-Manlius High School, Manlius, NY Abhinav Madabhushi, Chirec International School, Hyderabad, Telangana, India Eyal Noy, Rochelle Zell Jewish High School, Deerfield, IL Audrey Zhan, Westminster School, London, UK Alex Zhang, Newton North High School, Newton, MA Alan Zhu, Livingston High School, Livingston, NJ</p>
2 min	<p>Polymeric Hole Transport Layer in Perovskite Solar Cells</p> <p>Miller Liao, Shenzhen Middle School, Shenzhen, China Grace Kyoko Wong, St Paul's Girls' School, London, UK</p>

2 min	Methylammonium Chloride Assisted Growth of High Quality FAPbI ₃ Shiqi Cheng , Illinois Mathematics and Science Academy, Aurora, IL Adin Moskowitz , Hebrew Academy of Nassau County, Uniondale, NY Justin Shnayder , Staten Island Technical High School, Staten Island, NY
2 min	Science At-Home Experiment Video 5
1 min	Adjourn

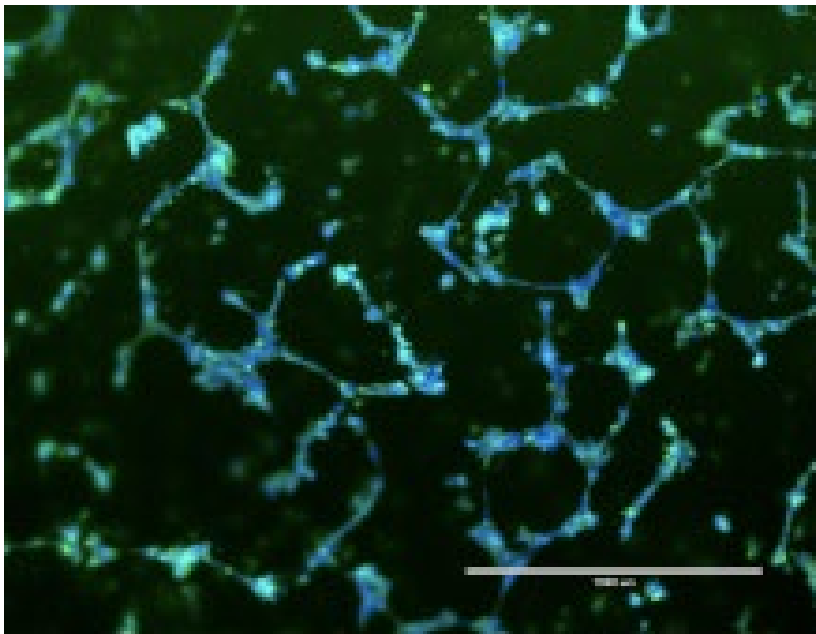
Garcia 2021 Logo designed by LeAnn Tai

*We gratefully acknowledge support from the
Louis Morin Charitable Trust*

SESSION I:

The Influence of Nanoparticles on Human Cells

Mentors: Shi Fu and Dr. Fan Yang



The Impact of TiO₂ on the Network Mechanics of HUVEC

Sabreen Alam¹, Prabuddha Ghosh Dastidar², Shi Fu³, Mira Rosovsky⁴, Elizabeth Wang⁵, Daniel Xie⁶

¹Portola High School, Irvine, CA 92618, ²North Carolina School of Science and Mathematics, Durham, NC, 27705,

³Stony Brook University, Stony Brook, NY 11794, ⁴SAR High School, Riverdale, NY 10471, ⁵BASIS Chandler, Chandler, AZ 85249, ⁶Panther Creek High School, Cary, NC 27519

Titanium dioxide is commonly used in consumer applications such as cosmetics, electronics, and sunscreen [1]. Titanium dioxide nanoparticles are known to pose as health hazards to humans and cause impairments to nervous and reproductive systems [2]. Previous studies have determined that in combination with UV light, titanium dioxide has the capability of killing bacteria and microorganisms [3]. Given that endothelial cells aid in angiogenesis which provides nutrients and oxygen to newly formed tissue, evaluating the effect of titanium dioxide on endothelial cells could help to realize the impact on the healing factor in humans. Due to the prevalence of TiO₂ in consumer products, it is crucial to determine its effect on network formation between cells. TiO₂ nanoparticles may cause tangling of actin fibers, making it difficult for them to stretch out and create tubes. In this study, we aim to investigate the effect of different kinds of titanium dioxide concentrations on HUVEC angiogenesis. To test the effect of TiO₂ on cellular network formation and cell migration of HUVEC cells, HUVEC cells were treated with rutile TiO₂ and lecithin-coated rutile for 16 hours. A control was also incubated for 16 hours. After the cells were stained as seen in Figure 1 before being imaged by the EVOS microscope. Cellular networks of the HUVEC cells after treatment were analyzed using ImageJ. Timelapses spanning 16 hours were taken of the cell networks and each treatment group, along with the controls, were inputted into ImageJ for network quantification at the 8 hour, 12 hour, and 16 hour mark. This network growth model is important because it provides insight into whether HUVEC cells can be utilized for angiogenesis, and if they can, what treatment results are optimal for angiogenesis.

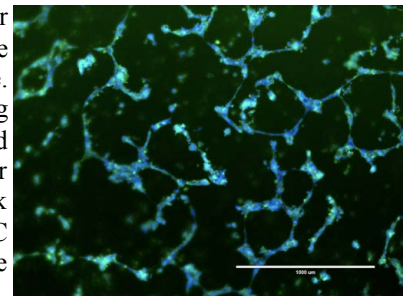


Figure 1. Stained network image of rutile treatment

The results from the network quantification indicate that rutile had significantly more network formation than the lecithin-coated rutile and control at all hours analyzed as seen in Figure 2. Next was the lecithin-coated rutile with control having the least amount of networks. This data suggests that TiO₂ may be a pro-angiogenic factor as treating the cells with rutile and lecithin-coated rutile, both containing TiO₂ nanoparticles, resulted in more network formation than the control group. Future tests will run the experiment again to make sure that TiO₂ is a pro-angiogenic factor, and cell migration data will be collected as well. The cell migration data will help to figure out how the HUVEC cells move during the entire 16 hours in which they were incubated.

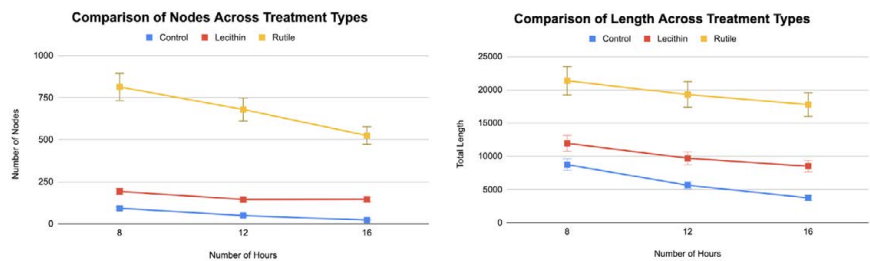


Figure 2. Comparison of the networks' nodes and lengths for different TiO₂ treatments

[1] Park, HG., Yeo, MK. Comparison of gene expression changes induced by exposure to Ag, Cu-TiO₂, and TiO₂ nanoparticles in zebrafish embryos. *Mol. Cell. Toxicol.* 9, 129–139 (2013).

<https://doi-org.proxy.library.stonybrook.edu/10.1007/s13273-013-0017-0>

[2] Yi Wu, Limei Chen, Feiran Chen, Hua Zou, Zhenyu Wang. A key moment for TiO₂: Prenatal exposure to TiO₂ nanoparticles may inhibit the development of offspring. *Ecotoxicology and Environmental Safety*. Volume 202, 2020, <https://doi.org/10.1016/j.ecoenv.2020.110911>.

[3] Tsuang, Y.-H., Sun, J.-S., Huang, Y.-C., Lu, C.-H., Chang, W.H.-S. and Wang, C.-C. (2008), Studies of Photokilling of Bacteria Using Titanium Dioxide Nanoparticles. *Artificial Organs*, 32: 167-174.

<https://doi-org.proxy.library.stonybrook.edu/10.1111/j.1525-1594.2007.00530.x>

The Effect of Titanium Dioxide on Cell Survival and Proliferation and Bacterial Infection

Sabreen Alam¹, Prabuddha Ghosh Dastidar², Shi Fu³, Mira Rosovsky⁴, Elizabeth Wang⁵, Daniel Xie⁶

¹Portola High School, Irvine, CA 92618, ²North Carolina School of Science and Mathematics, Durham, NC, 27705,

³Stony Brook University, Stony Brook, NY 11794, ⁴SAR High School, Riverdale, NY 10471, ⁵BASIS Chandler, Chandler, AZ 85249, ⁶Panther Creek High School, Cary, NC 27519

Titanium dioxide is commonly used in consumer applications such as cosmetics, electronics, and sunscreen [1]. Titanium dioxide nanoparticles are known to pose as health hazards to humans and cause impairments to nervous and reproductive systems [2]. Previous studies have determined that in combination with UV light, titanium dioxide has the capability of killing bacteria and microorganisms [3]. Given that endothelial cells aid in angiogenesis which provides nutrients and oxygen to newly formed tissue, evaluating the effect of titanium dioxide on endothelial cells could help to realize the impact on the healing factor in humans. In this study, we aimed to investigate the effect of varying concentrations of titanium dioxide on the proliferation of HUVEC cells. Cells in 24-well plates were treated with either Rutile or Lecithin-coated Rutile, and a control group with no treatment was used for comparison. The cells were treated with 4 different concentrations - 0.05 mg/ml, 0.1 mg/ml, 0.2 mg/ml, and 0.4 mg/ml. Afterwards, the cells were left in the incubator at a temperature of 37 degrees Celsius with 5% CO₂ and 80% humidity. To test TiO₂'s antibacterial properties, HUVEC cells were exposed to rutile TiO₂ and lecithin-coated rutile and left to sit for one day. They were then infected with *S. aureus* bacteria in order to determine TiO₂'s effect on the infection. After 24 hours, images of each of the cell

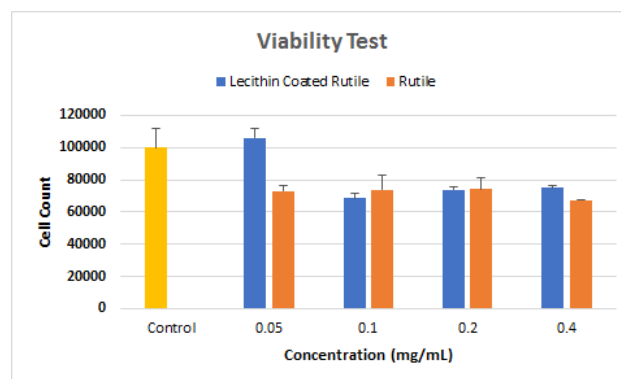
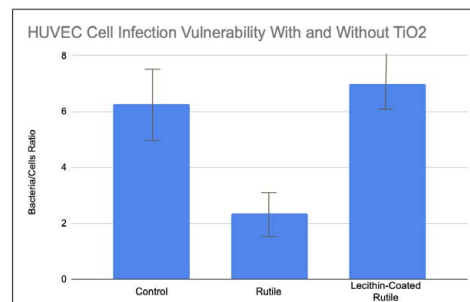


Figure 1. Cell counts for samples treated with Rutile and Lecithin.

plates were taken using an EVOS cell imaging system for both the viability and bacteria test. The cell count was then extracted from the images using ImageJ to find the impact of the TiO₂ treatment on the cells for the viability test. The cell counts were used to test the viability of using titanium dioxide to help with cell proliferation. Through the test (Figure 1), a decrease in the cell count can be seen as the concentration increases for both treatments. This demonstrates that titanium dioxide nanoparticles inhibit the growth and proliferation of the HUVEC cells. The alive and dead cells and bacteria for the bacteria infection test were also counted by hand using ImageJ for each of the 9 different wells. The total bacteria was then divided by the total cells for each of the wells and the 9 bacteria per cell numbers were averaged. In Figure 2, the bacteria per cell for the control is greater than that of the Rutile test which shows that TiO₂ may have antibacterial properties.



	Control	Rutile	Lecithin-Coated Rutile
Bacteria/Cells Ratio	6.27	2.36	6.99

Future tests will look at the impact of titanium dioxide nanoparticles

Figure 2. *S. Aureus* per cell for the different treatments of TiO₂

on the doubling time of HUVEC cells to gain further insight on the impact that TiO₂ has on cell survival and proliferation.

[1] Park, HG., Yeo, MK. Comparison of gene expression changes induced by exposure to Ag, Cu-TiO₂, and TiO₂ nanoparticles in zebrafish embryos. *Mol. Cell. Toxicol.* 9, 129–139 (2013).

<https://doi-org.proxy.library.stonybrook.edu/10.1007/s13273-013-0017-0>

[2]Yi Wu, Limei Chen, Feiran Chen, Hua Zou, Zhenyu Wang. A key moment for TiO₂: Prenatal exposure to TiO₂ nanoparticles may inhibit the development of offspring. *Ecotoxicology and Environmental Safety*. Volume 202, 2020,

<https://doi.org/10.1016/j.ecoenv.2020.110911>.

[3]Tsuang, Y.-H., Sun, J.-S., Huang, Y.-C., Lu, C.-H., Chang, W.H.-S. and Wang, C.-C. (2008), Studies of Photokilling of Bacteria Using Titanium Dioxide Nanoparticles. *Artificial Organs*, 32: 167-174.

<https://doi-org.proxy.library.stonybrook.edu/10.1111/j.1525-1594.2007.00530.x>

Impact of SynOss on the Doubling Time of Dental Pulp Stem Cells

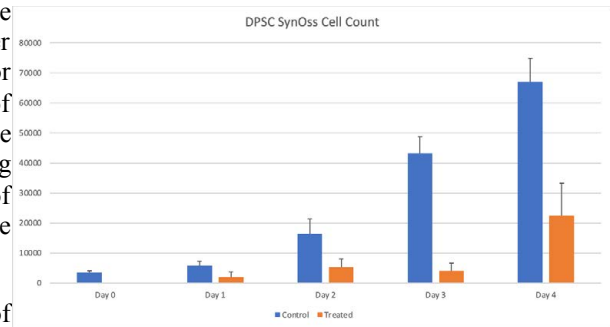
Sabreen Alam¹, Prabuddha Ghosh Dastidar², Shi Fu³, Mira Rosovsky⁴, Elizabeth Wang⁵, Daniel Xie⁶

¹Portola High School, Irvine, CA 92618, ²North Carolina School of Science and Mathematics, Durham, NC, 27705, ³Stony Brook University, Stony Brook, NY 11794, ⁴SAR High School, Riverdale, NY 10471, ⁵BASIS Chandler, Chandler, AZ 85249, ⁶Panther Creek High School, Cary, NC 27519

SynOss Synthetic Mineral is a bioclinical material that contains collagen; it has previously been shown to be associated with the use of regeneration of cell tissue in teeth and bones. [1] Previous studies have determined that a more predictable tissue regeneration was found in the majority of samples using SynOss and blood as a scaffold. [2] This demonstrates that SynOss has properties that aid in the growth and regeneration of tissue. Analyzing the impact of SynOss on the proliferation of dental pulp stem cells helps to bring insight into the clinical applications of SynOss such as the recovery of dental pulp after dental surgery. In this study, we aimed to investigate the effect of a concentration of SynOss on the doubling time of dental pulp stem cells. 27 wells of dental pulp stem cells were obtained and 15 of the cell wells were split into 3 wells for each day between day 0 to day 4 for the control.

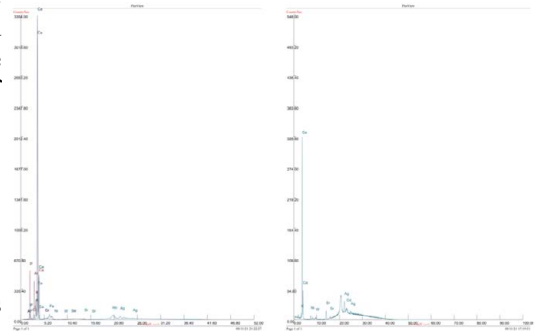
However, for the cell wells treated with SynOss, 12 wells were split into 3 wells for each day starting from day 1 to day 4. After the cells were plated into the cell wells with growth media and/or treatment, the cells were left in the incubator at a temperature of 37 degrees Celsius with 5% CO₂ and 80% humidity. After, the cells were stained and then imaged using the EVOS cell imaging machine to obtain the cell counts to analyze the impact of SynOss on the doubling time of the stem cells. The cells were counted using ImageJ and the cell count for each of the

Figure 1. Cell counts for dental pulp stem cells during each day 3 wells for each day were averaged. In Figure 1, the number of



cells in each control well was drastically greater than those in the treated wells. This leads to the belief that the SynOss material is inhibiting the growth and proliferation of the cells. SynOss was then measured using the XRF machine to find the elemental composition of it to help with finding the issue in the SynOss. Two different modes were used to test the composition of SynOss. TestAll Geo and General Metals. These modes helped to find the ppm of calcium and phosphate in the material. The spectra (Figure 2.) from the TestAll Geo and general metal modes shows that there is a large quantity of calcium and phosphate which provides a ratio of 2.5 +/- 0.011, similar to that of bones which has a ratio of 2.2.

Figure 2. XRF Spectra for SynOss using TestAllGeo and General Metals mode



This would help with the mineralization since it has a similar ratio and therefore would provide similar properties to bones. However, traces of cadmium and tungsten were also found in the material which may help to prove why the SynOss did not aid in the cell proliferation. Cadmium and tungsten have properties that are carcinogenic which proves to be detrimental to the survival of the cells [3]. Therefore, it supports the findings in Figure 1. which depicts the SynOss as having much lower cell counts than the control. Future works will have an acellular test: no cells are incubated; only adding cell media for several days to check mineralization situation, perform alive stain for checking the doubling time once more and also perform a 28 day RTPCR and check cell morphology after 28 days of differentiation.

[1] Ali Nosrat, Alireza Kolahdouzan, Amir Hossein Khatibi, Prashant Verma, Davoud Jamshidi, Alan J. Nevins, Mahmoud Torabinejad. Clinical, Radiographic, and Histologic Outcome of Regenerative Endodontic Treatment in Human Teeth Using a Novel Collagen-hydroxyapatite Scaffold. *Journal of Endodontics*, Volume 45, Issue 2, 2019, Pages 136-143, <https://doi.org/10.1016/j.joen.2018.10.012>.

[2] Arin Alexander, Mahmoud Torabinejad, Seyed Aliakbar Vahdati, Ali Nosrat, Prashant Verma, Anupama Grandhi, Shahrokh Shabahang. Regenerative Endodontic Treatment in Immature Non Infected Ferret Teeth Using Blood Clot or SynOss Putty as Scaffolds, *Journal of Endodontics*, Volume 46, Issue 2, 2020, Pages 209-215, <https://doi.org/10.1016/j.joen.2019.10.029>.

[3] Freda Laulicht, Jason Brocato, Laura Cartularo, Joshua Vaughan, Feng Wu, Thomas Kluz, Hong Sun, Betul Akgol Oksuz, Steven Shen, Massimiliano Peana, Serenella Medici, Maria Antonietta Zoroddu, Max Costa, Tungsten-induced carcinogenesis in human bronchial epithelial cells, *Toxicology and Applied Pharmacology*, Volume 288, Issue 1, 2015, Pages 33-39, <https://doi.org/10.1016/j.taap.2015.07.003>.

The Influence of TiO₂ and ZnO Nanoparticles on Bacterial Infection of HeLa Cells

Joanna Li¹, William Strutton², Emily Zhou³, Fan Yang⁴

¹Townsend Harris High School, Flushing, NY 11367; ²Hastings High School, Hastings on Hudson, NY 10706; ³The Harker School, San Jose, CA 95129; ⁴Department of Materials Science and Chemical Engineering, Stony Brook University, Stony Brook, NY 11794

Due to the widespread use of Titanium dioxide (TiO₂) and Zinc oxide (ZnO) nanoparticles (NPs) in products such as sunscreen, cosmetics, and food additives, an improved understanding of their possible negative effects on cells may help to better ensure consumer safety and public health [1, 2]. Previous research showed that TiO₂ NPs in the rutile and anatase forms may impair cell function and defense against bacterial infection in HeLa cells and human dermal fibroblasts [3]. ZnO NPs have also been shown to exhibit cytotoxicity to cancer cells; a recent study found that, when compared to controls, HeLa cells with added ZnO NPs had significantly lowered cell viability [4].

This study aimed to measure the doubling time of HeLa cells exposed to TiO₂ NPs, ZnO NPs, and lecithin-coated TiO₂ (L-TiO₂) NPs to further the understanding of the effects of different NPs on HeLa cell proliferation. HeLa cells were infected with *Staphylococcus aureus* bacteria at a multiplicity of infection (MOI) of 1000. The cells in each well were counted at both 24 hours and 96 hours after their initial exposure to the NPs to calculate the average doubling time for each condition.

To this end, 6-well plates were used to culture 3-well groups of HeLa cells to which 3 types of NPs were added: TiO₂, lecithin-coated TiO₂ (L-TiO₂), and ZnO NPs. Each type of NP was added at a concentration of 0.1 mg/L, which was determined in an earlier study to be the concentration at which TiO₂ NPs negatively affected cells without killing them [5]. One group serving as the control received no NPs. The cells were plated after reaching 80% confluency, and TiO₂ and L-TiO₂ NPs mixed in cell culture media were added to the wells. Cells were plated and cultured with ZnO NPs later in the study, as there was an initial lack of access to ZnO NPs. The cultured cells were counted at 24 hours and 96 hours after exposure to NPs using a hemocytometer, and the average doubling time of HeLa cells growing under each condition was calculated. There was no significant difference between the average doubling time of the control group and those of the TiO₂ group or L-TiO₂ groups.

The cells were stained with Alexa Fluor 488 Phalloidin and the *S. aureus* bacteria were stained with a live dead stain to count the total number of cells and infected cells and the number of live and dead bacteria, respectively. An EVOS cell imaging system (fluorescence microscopy) was used to produce images for cell and bacteria counting (Figure 1).

For the ZnO sample, bacteria cell counts and doubling time remain to be obtained. Once all data is present, further analyses will be needed to determine its possible significance. Future studies may include other NPs, or additional experiments on the nanotoxicity of ZnO if it is found to significantly affect the proliferation of HeLa cells or their resistance to *S. aureus* infection.

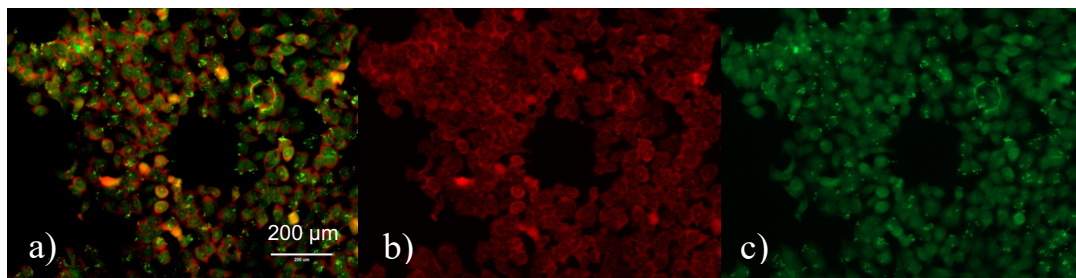


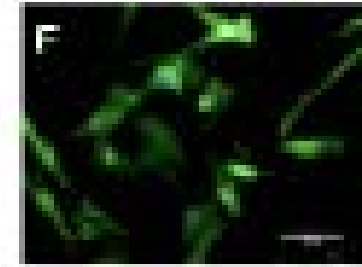
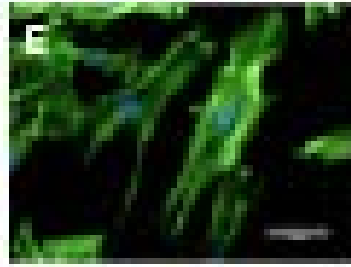
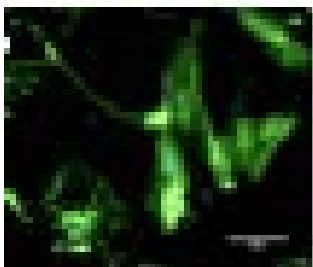
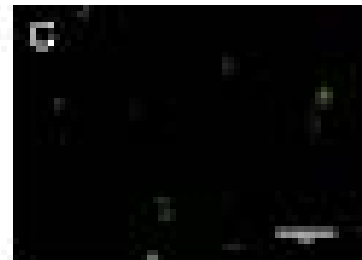
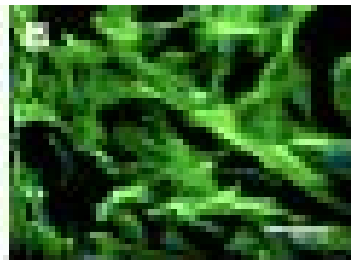
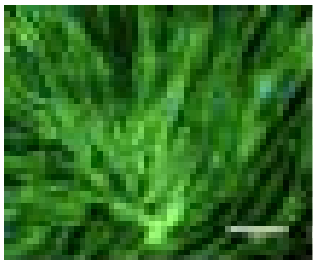
Fig. 1. a) EVOS images showing *S. aureus* and HeLa cells with both red and green channels. b) The red channel shows cells and dead bacteria (indicated by fluorescent red points). c) The green channel shows cells and live bacteria (indicated by fluorescent green points).

- [1] Xu, Yan, et al. "Exposure to TiO₂ Nanoparticles Increases Staphylococcus Aureus Infection of HeLa Cells." *Journal of Nanobiotechnology*, vol. 14, no. 1, 22 Apr. 2016, <https://doi.org/10.1186/s12951-016-0184-y>.
- [2] Vallabani, N. V Srikanth, et al. "ZnO Nanoparticles-associated Mitochondrial Stress-induced Apoptosis and G2/M Arrest HaCaT Cells: A Mechanistic Approach." *Mutagenesis*, vol. 34, no. 3, May 2019, pp. 265-77, <https://doi.org/10.1093/mutage/gez017>.
- [3] Pan, Zhi, et al. "Adverse Effects of Titanium Dioxide Nanoparticles on Human Dermal Fibroblasts and How to Protect Cells." *Small*, vol. 5, no. 4, 20 Feb. 2009, pp. 511-20, <https://doi.org/10.1002/sml.200800798>.
- [4] Yang, Yanjie, et al. "ZnO Quantum Dots Induced Oxidative Stress and Apoptosis in HeLa and HEK-293T Cell Lines." *Frontiers in Pharmacology*, vol. 11, 27 Feb. 2020, <https://doi.org/10.3389/fphar.2020.00131>.
- [5] ---. "Exposure to TiO₂ Nanoparticles Increases Staphylococcus Aureus Infection of HeLa Cells." *Journal of Nanobiotechnology*, vol. 14, no. 1, 22 Apr. 2016, <https://doi.org/10.1186/s12951-016-0184-y>.

SESSION II:

Differentiation of Dental Pulp Stem Cells

Mentors: Shi Fu and Haijiao Liu



The Effect of Hypochlorous Acid on the Migration and Differentiation of Dental Pulp Stem Cells

Sabreen Alam¹, Prabuddha Ghosh Dastidar², Shi Fu³, Mira Rosovsky⁴, Elizabeth Wang⁵, Daniel Xie⁶
¹Portola High School, Irvine, CA 92618, ²North Carolina School of Science and Mathematics, Durham, NC, 27705,
³Stony Brook University, Stony Brook, NY 11794, ⁴SAR High School, Riverdale, NY 10471, ⁵BASIS Chandler,
Chandler, AZ 85249, ⁶Panther Creek High School, Cary, NC 27519

Hypochlorous acid (HOCl) is a weak acid that acts as the primary active component of disinfectant solutions. It is known to effectively eliminate bacteria and biofilms while minimizing adverse impacts on surrounding tissue and without leaving harmful residues [1]. Due to its nontoxic and non-corrosive nature, hypochlorous acid has a wide range of clinical applications, from wound healing to eye care. Previous studies have also confirmed the efficacy of hypochlorous acid as a root canal irrigation solution [2]. Irrigation is a critical step in dissolving organic matter and effectively eradicating harmful microbes during root canal treatments [3]. Prior to irrigation, scaffolds consisting of dental pulp stem cells and growth factors are implanted into root canals to promote regeneration of a dentine-pulp complex [4].

The objective of this study is to investigate the effect of hypochlorous acid on dental pulp stem cells. Analyzing the cytotoxicity of hypochlorous acid contributes important information on the safety and effectiveness of using this compound in root canal irrigation. In addition, examining the migration and differentiation of dental pulp stem cells in response to hypochlorous acid can provide insight into whether the solution will stimulate mineralization if leakage occurs on live cells around the root.

A solution consisting of 30% hypochlorous acid mixed with Alpha Minimum Essential Medium (MEM) was added into 6-well tissue culture plastic (TCP) plates containing dental pulp stem cells for 5 minutes in an incubator, and washed with phosphate-buffered saline (PBS) twice. On Day 0, media containing multiple compounds to trigger the dental pulp stem cells to differentiate was added (RT-PCR calculations shown in Figure 1). On Day 14, a solution was added to induce cell lysis, after which centrifugation was used to produce an RNA mixture. This was stored at 80 degrees Celsius for later analysis of the RNA profile. The cells were harvested and analyzed for abnormalities in growth and genetic expression on Day 28.

ImageJ was used to calculate the number of cells and cell migration across different time intervals. Future directions would include additional trials of the different concentrations of hypochlorous acid on dental pulp stem cells, observing the effects of hypochlorous acid on scaffolds with dental pulp stem cells and relevant growth factors, and analyzing the long-term effects of hypochlorous acid compared to alternative root canal irrigation solutions on differentiation and dentine-pulp complex regeneration.

Top count	Bottom Count	Single Square Average	cell count		Neutralize d Trypsin	total cell	Cell suspension	Medium Needed
#	#	#	#	cell/ml	ml	cell	cell/ml	ml
265	288	69.125	69.125	1.00E+04	10	6.91E+06	2.00E+05	34.56

Figure 1. RT-PCR calculations for dental pulp stem cells growth/differentiation media

[1] Chen, C. J., Chen, C. C., & Ding, S. J. (2016). Effectiveness of Hypochlorous Acid to Reduce the Biofilms on Titanium Alloy Surfaces in Vitro. *International journal of molecular sciences*, 17(7), 1161.

<https://doi.org/10.3390/ijms17071161>

[2] Hsieh, S. C., Teng, N. C., Chu, C. C., Chu, Y. T., Chen, C. H., Chang, L. Y., ... & Yang, J. C. (2020). The antibacterial efficacy and in vivo toxicity of sodium hypochlorite and electrolyzed oxidizing (EO) water-based endodontic irrigating solutions. *Materials*, 13(2), 260.

[3] Haapasalo, M., Shen, Y., Wang, Z., & Gao, Y. (2014). Irrigation in endodontics. *British dental journal*, 216(6), 299–303. <https://doi.org/10.1038/sj.bdj.2014.204>

[4] Bakhtiar, H., Mazidi S, A., Mohammadi Asl, S., Ellini, M. R., Moshiri, A., Nekoofar, M. H., & Dummer, P. (2018). The role of stem cell therapy in regeneration of dentine-pulp complex: a systematic review. *Progress in biomaterials*, 7(4), 249–268. <https://doi.org/10.1007/s40204-018-0100-7>

The Effect of Surface Chemistry on Dental Pulp Stem Cells in Neurogenic Differentiation

Leigh Baratta¹, Nikhil Mehta¹, Claire Richter², Layla Shaffer³, Andrew Yuen⁴, Katie Rosshirt⁵, Kuan-che Feng⁶, Haijiao Liu⁶, Marcia Simon⁷, Miriam Rafailovich⁶

¹Smithtown High School East, NY, 11780; ²South Side High School, NY, 11570; ³The Lawrenceville School, NJ, 08648; ⁴Jericho High School, NY; ⁵University of Notre Dame, IN, 46556; ⁶Department of Materials Science and Chemical Engineering, Stony Brook University, NY, 11794; ⁷Department of Oral Biology and Pathology, School of Dental Medicine, Stony Brook University, NY, 11794

Neurodegenerative diseases represent a major incapacitating health problem of the foreseeable future. If the nervous system sustains injuries or damage, the neurons are unable to efficiently regenerate or repair in response¹. To combat such damage to the nervous system, Dental Pulp Stem Cells (DPSCs), pluripotent stem cells that can effectively differentiate into neurons, are vital in neuroregenerative medicine due to their accessibility at the human third molars and neurogenic abilities². Neurogenic differentiation can be promoted with the use of polymers to regulate the substrate mechanisms. The purpose of this study is to investigate various substrate materials for their efficiency in neurogenic differentiation of DPSC. Poly (4-vinyl pyridine) (P4VP) is a glassy surface polymer with uniform surface properties and a structure comparable to polystyrene³. Polyvinylidene Fluoride (PVDF) has a high tensile strength and abrasion resistance with ferroelectric properties⁴. RDP/Clay with PLA is a biodegradable and non-toxic phosphorus blend⁵. Polybutadiene (PB) is a biocompatible and synthetic polymer that produces uniform films³. The addition of TiO₂ to Polybutadiene (PB) adds a UV filtering through its light scattering properties and high refractive index⁶. To create thin films, solutions of 3% PVDF with Dimethylformamide (DMF), 20 mg/ml

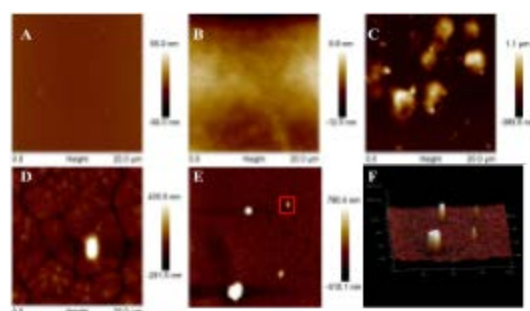


Figure 1. AFM surface morphology images A) P4VP, B) PB, C) PVDF, D) RDP/Clay with PLA 20 µm, E) RDP/Clay with PLA 80 µm, F) 3D image of RDP/Clay with PLA 80 µm

Polybutadiene with toluene, 7 mg/ml Poly(4-vinylpyridine) P4VP with DMF, and 30 mg/ml RDP/clay with PLA and Chloroform were spun cast unto cleaved silicon wafers. The wafers were spun cast at 2500 rpm at 1000 rpm/s for 30s, 3000 rpm at 1500 rpm/s for 45s, 2500 rpm at 1000 rpm/s for 30s, and 4000 rpm at 3000 rpm/s for 30s for the PB, P4VP, RDP/Clay, and PVDF solutions respectively. The surface morphology of the various thin films were then analyzed with Atomic Force Microscopy (AFM) imaging and Nanoscope Analysis software. The AFM images, as shown in **Figure 1**, present the various film topographies. The cells were then cultured with growth media for 3 days, then replaced with neurobasal media and changed twice a week. The neurobasal A media was composed of 100 µg/mL penicillin, 1X B27 supplement, 100 µg/mL streptomycin, 20 ng/mL epidermal growth factor (EGF) and 40 ng/mL fibroblast growth factor (FGF). The EVOS scans a sample to present the cell morphology of day 0 and day 7, as shown in **Figures 2** and **3**, and will be performed again on day 28. In order to collect the images, the cells were stained with DAPI and Alexa Fluor 488. On day 0, day 14, day 21, and day 28, Real-Time Polymerase Chain Reaction (RT-PCR) will be performed on the DPSCs to investigate the degree of neuronal differentiation on the genetic level. The RNA will be isolated using QIAzol lysis reagent and the RT-PCR will be conducted to quantify the expression of the neuromarkers Nestin(early), β-Tubulin-III (intermediate), and NEFM (mature).

Polybutadiene with toluene, 7 mg/ml Poly(4-vinylpyridine) P4VP with DMF, and 30 mg/ml RDP/clay with PLA and Chloroform were spun cast unto cleaved silicon wafers. The wafers were spun cast at 2500 rpm at 1000 rpm/s for 30s, 3000 rpm at 1500 rpm/s for 45s, 2500 rpm at 1000 rpm/s for 30s, and 4000 rpm at 3000 rpm/s for 30s for the PB, P4VP, RDP/Clay, and PVDF solutions respectively. The surface morphology of the various thin films were then analyzed with Atomic Force Microscopy (AFM) imaging and Nanoscope Analysis software. The AFM images, as shown in **Figure 1**, present the various film topographies. The cells were then cultured with growth media for 3

days, then replaced with

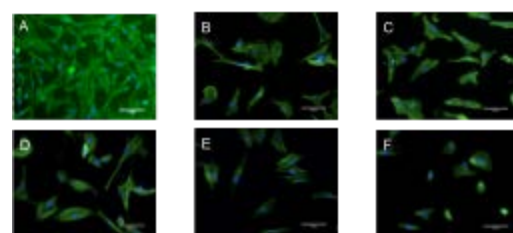


Figure 2. EVOS Day 0 20x Imaging: A) TCP, B) P4VP, C) PVDF, D) RDP, E) PB, F) PB/TiO2

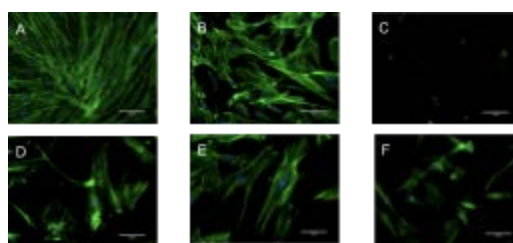


Figure 3. EVOS Day 7 20x Imaging: A) TCP, B) P4VP, C) PVDF, D) RDP, E) PB, F) PB/TiO2

¹Przedborski, S., Vila, M., & Jackson-Lewis, V. (2003). Neurodegeneration: The Journal of clinical investigation, 111(1), 3-10. <https://doi.org/10.1172/JCI17522>

²Aljamie, M., Alessa, L., Noah, R., & Elyased, L. (2016). Dental pulp stem cells, a new era in Regenerative medicine: A literature review. Open Journal of Stomatology, 06(06), 155-163. <https://doi.org/10.4236/ojst.2016.66020>

³Jurukovski, Vladimir & Rafailovich, Miriam & Simon, Marcia & Bherwani, A. & Chan, Chung-Chueng. (2014). Citation: Entangled Polymer Surface Confinement, an Alternative Method to Control Stem Cell Differentiation in the Absence of Chemical Mediators. Annals of Materials Science & Engineering. Advances in Materials Science and Engineering. 1. 3-2014.

⁴Park, Youn & Sung, Jinwoo & Jo, Pil & Park, Cheolmin & Kim, Kap Jin & Cho, Beong. (2008). Spin cast ferroelectric beta poly(vinylidene fluoride) thin films via rapid thermal annealing. Applied Physics Letters. 92. 012921-012921. 10.1063/1.2830701.

⁵Singha, S., & Hedenqvist, M. S. (2020). A Review on Barrier Properties of Poly(Lactic Acid)/Clay Nanocomposites. Polymers, 12(5), 1095. <https://doi.org/10.3390/polym12051095>

⁶Skocaj, M., Filipic, M., Petkovic, J., & Novak, S. (2011). Titanium dioxide in our everyday life; is it safe?. Radiology and oncology, 45(4), 227-247. <https://doi.org/10.2478/v10019-011-0037-0>

SESSION III:

Machine Learning and Artificial Intelligence

Mentors: Nilesh Chaturvedi, Shubham Agrawal, Dasharadhan Mahalingam, and Dr. Fan Yang

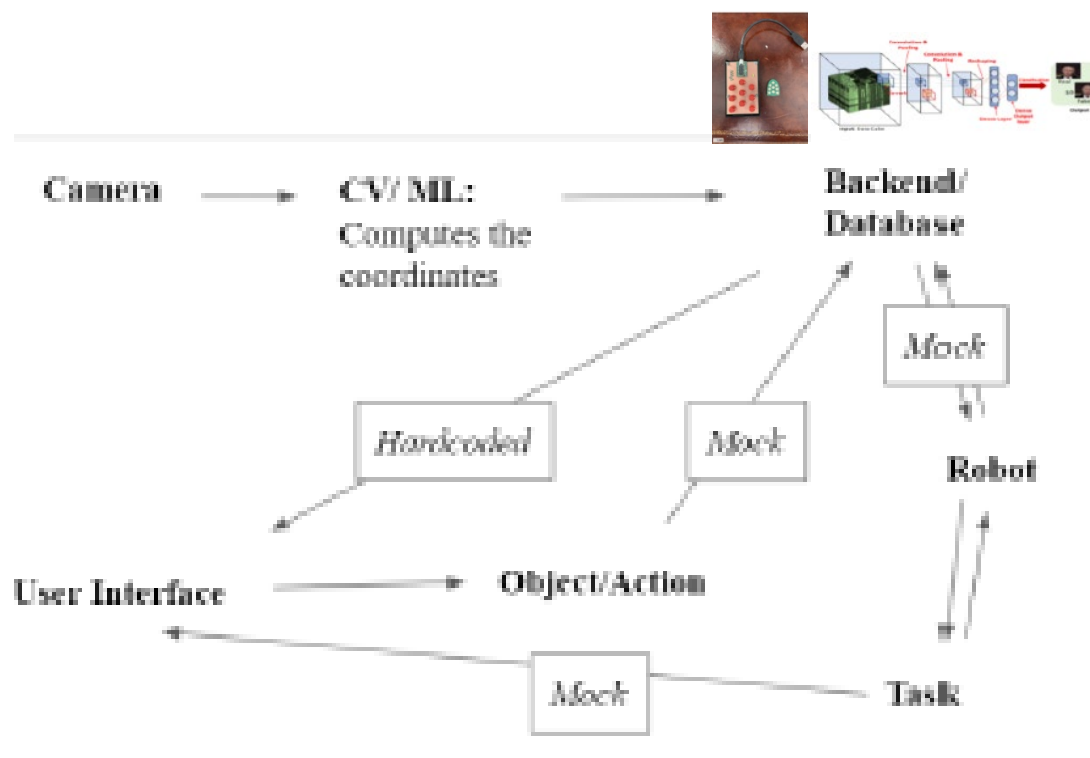


Fig 2. Flowchart of robot-human interface pipelines.

Deepfake Video Detection Using Biologically Inspired Geometric Deep Learning

Yash Agarwal¹, Eric Guan², Krish Jain³, Steven Luo⁴, Aayush Sheth⁵, Jansen Wong⁶, Eric Zhu⁷, Rena Max⁸, Nilesh Chaturvedi⁹, Fan Yang¹⁰, Miriam Rafailovich¹⁰, Pawel Polak⁹

¹Dougherty Valley High School, San Ramon, CA 94582; ²North Carolina School of Science and Mathematics, Durham, NC 27705; ³Redmond High School, Redmond, WA 98052; ⁴Evergreen Valley High School, San Jose, CA 95148; ⁵Tesla STEM High School, Redmond, WA 98053;

⁶Great Neck South High School, Great Neck, NY 11020; ⁷Princeton High School, Princeton, New Jersey, 08540; ⁸Department of Computer Science, University of Maryland, College Park, MD 20742; ⁹Department of Applied Mathematics and Statistics, Stony Brook University, Stony Brook, NY 11794; ¹⁰Department of Materials Science and Chemical Engineering, Stony Brook University, Stony Brook, NY 11790

Deepfakes are a form of synthetic media in which a person's appearance is altered to look like another's. As the technology used to generate deepfakes improves and becomes more accessible, they can more easily be used for anonymizing journalistic sources and everyday artistic expression, but the potential to spread misinformation and discredit others also increases. Since deepfakes are able to deceive the human senses by creating hyper-realistic manipulations¹, the ability to identify them is critical in preserving the integrity of digital media, and computers are uniquely able to do so.

In order to determine if a video was a deepfake, we first divided the video into individual frames. Then, to correspond to the parts of a human face in each frame, we used a 3D manifold of 468 landmarks created by the open-source MediaPipe library from Google². This was used to measure the movements of human face muscles for facial construction during the training of the biologically inspired geometric deep neural network. A sphere was created around every landmark to record uniformly spaced points. These landmarks were then input into an optical method that employs tracking and image recognition techniques for accurate measurement of deformation (displacement and strain) from digital images. We estimated the Jacobian matrix of the transformation of the FaceMesh from one frame to the next and used the Jacobian determinant to properly scale each sphere's radius between frames. Due to the local topology induced by the FaceMesh points, the produced features are robust against translation and rotation of the face in the frame (Figure 1).

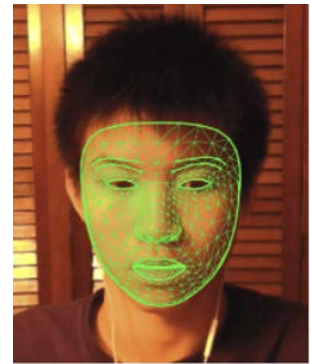


Figure 1: A facemesh is applied

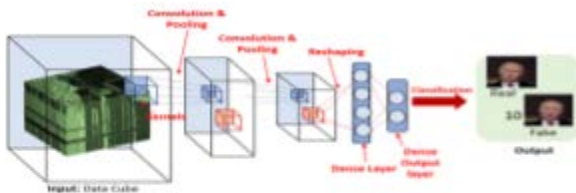


Figure 2: Outline of 3D CNN used to identify deepfakes

The frames that went through the optical method which records displacement of muscle movements were used as features in a 3D Convolutional Neural Network (CNN) to classify fake and real videos (Figure 2). The proposed model will be trained on state of the art, publicly available sets of manipulated and real videos, including FaceForensics³, FaceForensics++⁴, and Deep Fakes Dataset¹, with more than 500 gigabytes of data available.

We constructed a website for users to upload their own videos and to detect whether they are deepfakes or not. The frontend was written in React JS while the backend was written in Python using Flask using Nginx as the front-facing server and Gunicorn to server the Flask app, both of which are currently hosted on Stony Brook University servers. Ultimately, the trained model will be used as a predictor in the publicly available website on a university server which will allow users to analyze their own videos and label them as fake or real.

¹Ciftci, Umur Aybars, Ilke Demir, and Lijun Yin. "Fakecatcher: Detection of Synthetic Portrait Videos using Biological Signals." *IEEE Transactions on Pattern Analysis and Machine Intelligence* (2020).

²Kartynnik, Yury, et al. "Real-Time Facial Surface Geometry from Monocular Video on Mobile GPUs." *arXiv preprint arXiv:1907.06724* (2019).

³Rössler, Andreas, et al. "FaceForensics: A Large-Scale Video Dataset for Forgery Detection in Human Faces." *arXiv preprint arXiv:1803.09179* (2018).

⁴Rössler, Andreas, et al. "FaceForensics++: Learning to Detect Manipulated Facial Images." *Proceedings of the IEEE/CVF International Conference on Computer Vision* (2019).

Creating an Interface for the Operation of a Robotic Arm

Matthew Garcia¹, Dyllan Hofflich², David Tarrab³, Audrey Wong⁴, Lauren Yu⁵, Shubham Agrawal⁶,
Dasharadhan Mahalingam⁶, Nilanjan Chakraborty⁶

¹ Plainedge High School, North Massapequa NY; ² Pelham Memorial High School, Pelham NY 10803; ³ Ramaz Upper School, New York NY; ⁴ Beckman High School, Irvine CA 92602; ⁵ Brea Olinda High School, Brea CA 92823; ⁶ Stony Brook University, Stony Brook, NY 11790

Ailments like Parkinson's disease, carpal tunnel syndrome, arthritis, and cerebral palsy can leave individuals severely limited in mobility and unable to perform essential tasks. The diseases and impairments listed above all damage functionality in the upper arms. The use of a robotic arm to perform activities of daily living (ADL's) may be able to address these limitations.

Previous studies have sought to confront similar issues. A study by Maheu et al. found that the use of a JACO robotic arm has the potential to reduce caregiving time by 41%¹.

The goal of this study is to control a robotic arm with eye-gaze technology or a Tongue Touch Keypad (TTK) through the shared context of a web interface (Fig 1). Created with HTML, CSS, and JavaScript, the interface was designed to facilitate clear communication between the user and robot arm. To allow the robotic arm to complete a task with missing information, the interface included a query-based system that would allow the user to supply additional information to aid the robot in performing a task. Important design decisions included the size and placement of buttons as well as the display of information on the interface to address the heightened error that follows eye-tracking².

This web interface will ultimately be built into the robot arm system to allow for its full testing and use by individuals. Two different pipelines will be present, the first using a wheelchair-mounted camera to acquire the coordinates of objects (Fig 2). The second will act upon the user's interactions with the interface as an object with a corresponding movement is selected; this information is then sent to the robot arm for the requested action to be executed. This backend development will be completed using ROS (Robot Operating System) and further project development will include optimizing communication between nodes, which include the web interface, camera, and various modalities of user interaction.

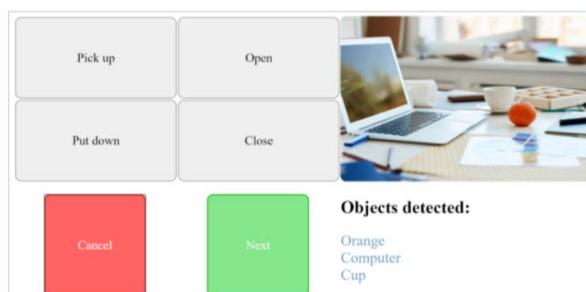


Fig 1. Web interface.

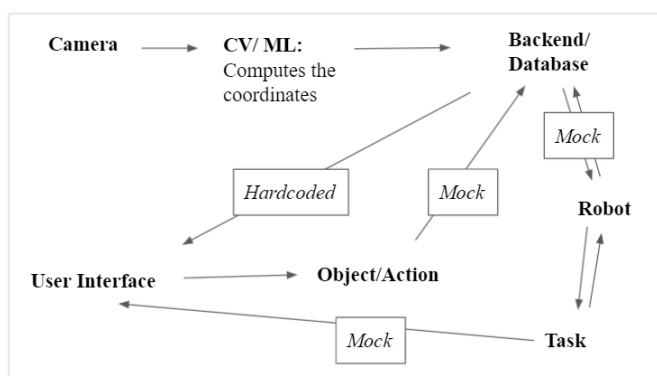


Fig 2. Flowchart of robot-human interface pipelines.

¹ Maheu, Veronique et al. "Evaluation of the JACO robotic arm: clinico-economic study for powered wheelchair users with upper-extremity disabilities." IEEE ... International Conference on Rehabilitation Robotics : [proceedings] vol. 2011 (2011): 5975397. doi:10.1109/ICORR.2011.5975397

² Feit, Anna Maria, et al. "Toward Everyday Gaze Input." Proceedings of the 2017 CHI Conference on Human Factors in Computing Systems, 2 May 2017, doi:10.1145/3025453.3025599.

Implementation of TTK for Control of Multiple Devices

Ezra Reiss¹, Hugh Rosshirt², Ethan Pereira³, Adin Moskowitz⁴ and Michael Gouzman⁵

Hebrew Academy Of Nassau County,¹ University of Notre Dame², West Windsor-Plainsboro High School North³, Hebrew Academy of Nassau County⁴, Department of Electrical and Computer Engineering, Stony Brook University⁵

For many within the disabled community, accomplishing even the simplest tasks can seem impossible. With the help of robotics, an interdisciplinary science that incorporates engineering, biology, and physics, we can aid those with disabilities in day-to-day tasks. For example, many quadriplegia control their wheelchairs via a Sip and Puff system where they suck and blow through a tube. The wheelchair then moves based on the intensity and direction of the airflow through the tube. This solution allows quadriplegia to control their wheelchair when otherwise impossible.

This method of control can often be inconvenient and physically taxing. Therefore, our objective is to improve the effectiveness of an electric wheelchair system tailored for a quadriplegia. Our focus is to effectively replace the old wheelchair control method (Sip and Puff) with a Tongue Touch Keyboard (TTK) [1]. As such, we plan to set up the TTK as a “computer mouse” capable of accessing and controlling a central computer within the wheelchair. The goal of this project is to create a system through which the wireless capabilities of the TTK can be processed to direct signals for control of multiple external devices. The capability of the TTK aimed to harness in this project is to be able to both effectively control multiple systems as well as setup a capability to switch active control between multiple devices. To display a proof of concept and test for this system, we focused on a specific issue of spatial observation for the quadriplegic patient. As a result of no neck movement, patients are unable to both look at and detect objects in their vicinity, and hence we implemented a camera on a 360 degree swivel to simulate neck movement for all around observation of objects. In the future we also aim to incorporate this controlling modality for control of the patient’s wheelchair [2].

Due to many of us being online for the majority of the time we decided to use TeamViewer as our primary way to code into both the Arduino and Raspberry Pi. However, in-person visits were still required in order to fix device wiring. The Raspberry Pi allows us to detect mouse inputs which are sent to the Arduino via the serial port. The Arduino then communicates with a servo, instructing it which direction to rotate. For example, left mouse movement results in a counter clockwise servo movement, and right mouse movement causes the servo to rotate clockwise. We plan on further developing this project by adding a second servo motor which would allow the camera three dimensions of motion (up, down, left, and right). The ultimate goal is to apply this design to the TTK in order to control the entire wheelchair more conveniently.



Figure 1: Tongue Touch Keypad (TTK) for communicating with internal computer and servo motors

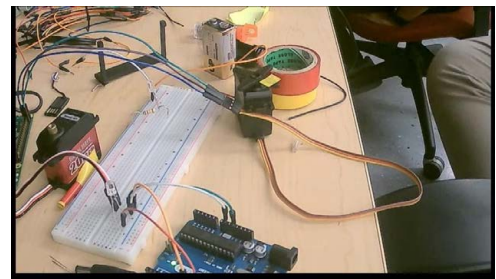


Figure 2: image of physical setup used to interpret the commands of the TTK and convey them to the motor.

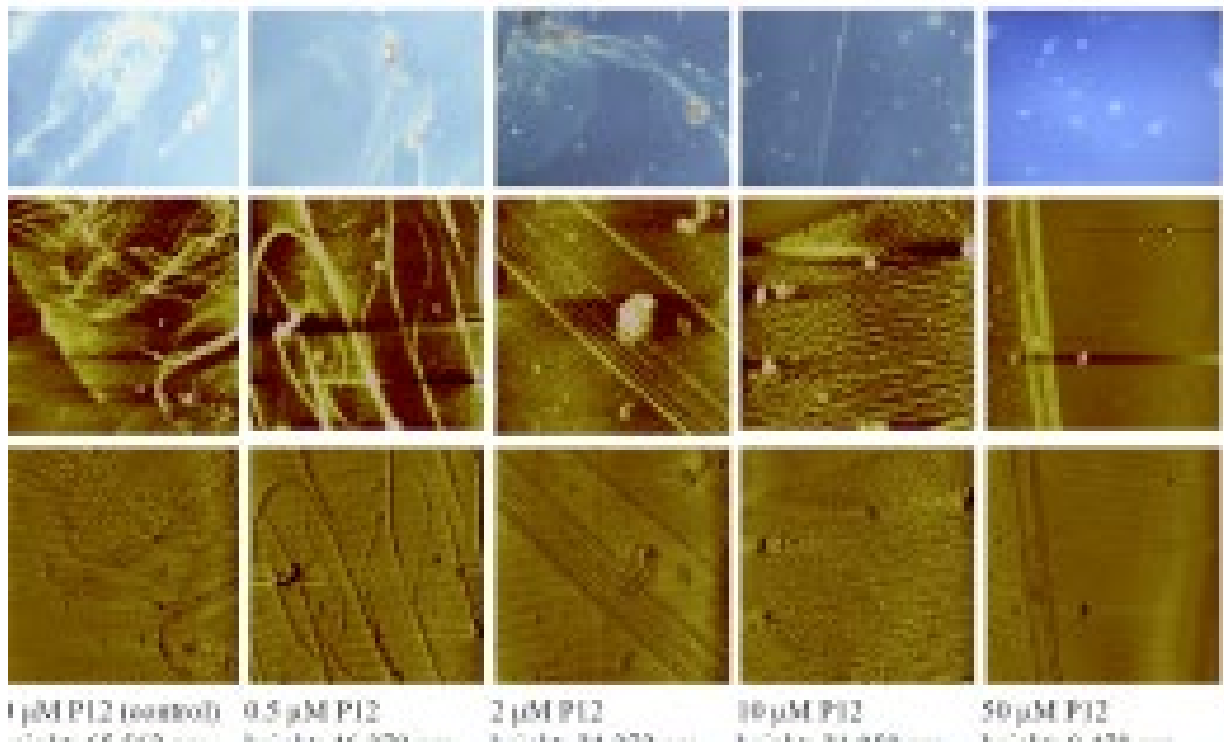
[1] Georgia Tech. (2013, December 3). Tongue-drive wheelchair works better than sip-and-puff system. *ScienceDaily*. Retrieved August 10, 2021 from www.sciencedaily.com/releases/2013/12/131203141834.htm

[2] Kim, J., Park, H., Bruce, J., Sutton, E., Rowles, D., Pucci, D., Holbrook, J., Minocha, J., Nardone, B., West, D., Laumann, A., Roth, E., Jones, M., Veledar, E., & Ghovanloo, M. (2013, November 27). *The Tongue Enables computer and Wheelchair control for people with spinal cord injury*. Science Translational Medicine. <https://stm.sciencemag.org/content/5/213/213ra166>.

SESSION IV:

Thrombosis and Viral Infection

Mentors: Kao Li and Bernard Essuman



Investigating How COVID-19 Induces Microthrombosis on Endothelial Cells

Nicole Gabriel¹, Aarushi Mehrotra², Jia Lu (Angela) Sun³, Sneha Sunder⁴, Serena Yang⁵, Anthony Deluxe⁶, & Kao Li⁷

¹South Side High School, Rockville Centre, NY 11570; ²Lynbrook High School, San Jose, CA 95129; ³Lord Byng Secondary, Vancouver, BC V6R 2C9, Canada; ⁴Fairfield Warde High School, Fairfield, CT 06825; ⁵Dougherty Valley High, San Ramon, CA 94582; ⁶New York University, New York, NY 10003; ⁷Stony Brook University, Stony Brook, NY 11794

SARS-CoV-2 infects lung epithelial cells through the interaction between its spike (S) proteins and the human angiotensin-converting enzyme 2 (ACE2) receptor [1]. It remains unknown how viral infection dysregulates vascular functions on endothelium tissue that cannot be directly infected due to a lack of ACE2 receptors [2]. Therefore, in this project, we aim to understand how thrombosis is induced on endothelial cells. Due to safety precautions, the H1N1 (PR8) strain was used instead of SARS-CoV-2, but even though the receptors for infection are different [1], both have similar epithelium-endothelium pathology [1,3].

To test the time dependency of the virus, cultures of human gingival epithelial cells, the host cells, and human umbilical vein endothelial (HUVEC) cells, the target cells, were established. Four samples of host epithelial cells were infected by placing them in viral media for 0.5, 1, 1.5, and 24 hours. Infected epithelial cell media was collected and incubated with the four respective samples of target HUVEC cells for 6 hours. The media was replaced with a fibrinogen solution and the samples were incubated for 6 more hours. The samples were then washed and stained with fluorescent antibody

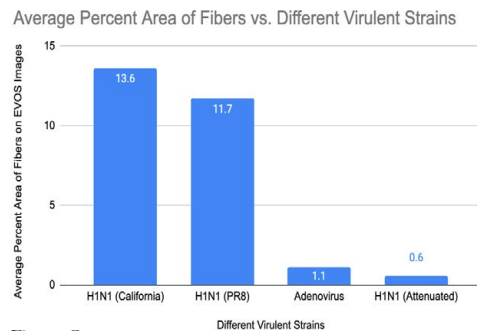
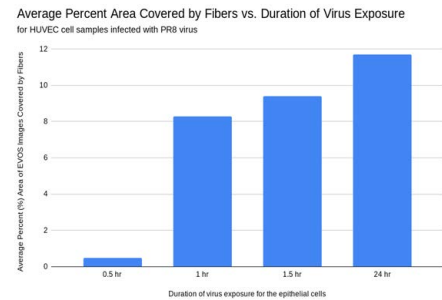


Figure 2

same process as described above was followed to induce thrombosis onto HUVEC cells with viral epithelial medium incubated for 24 hours, enough for one cycle of H1N1 replication. The findings are shown in Figures 2 and 3. It's important to note that although the adenovirus and attenuated H1N1 didn't have enough fiber formation to be considered virulent, these viruses are still capable of thrombosis and may pose a threat to certain vulnerable populations.

We then hypothesized that the presence of fibers on the hydrophilic endothelial cells was caused by cytokines which resulted in the hydrophobic cell surface, since fibrinogen self-assembles into fibers on hydrophobic surfaces but needs thrombin to do so on hydrophilic surfaces. To test this, hydrophilic surfaces were created by spin-casting a solution of poly(4-vinyl pyridine) (P4VP), a hydrophilic polymer, onto silicon wafers. The aforementioned 1.5 hours and 24 hours conditioned viral epithelial media was placed on the hydrophilic samples, followed by fibrinogen after 6 hours. Fibers were observed only in the samples that were exposed to viral medium from 24 hours infected cells. Additionally, the contact angles were measured on samples before fibrinogen was added, giving a value of 59.91 ± 1.49 for the pure P4VP control, 72.89 ± 1.54 for samples with a 1.5 hours infected medium, and 81.15 ± 0.91 for samples with 24 hours infected medium. The increase in contact angles supports the hypothesis that some factor in the medium is causing the surfaces to become increasingly hydrophobic, and from the fiber formation data, we can conclude that this factor is a cytokine released from infected epithelial cells.

Figure 1



tagging for imaging. The fibers were quantified using EVOS and ImageJ. The results show that just one hour was sufficient for substantial fiber formation (Figure 1).

Next, we compared different virulent strains and tested whether viruses deemed noninfectious would still induce thrombosis. The two highly infectious H1N1 strains tested were California and PR8. The two noninfectious viruses were attenuated H1N1 and adenovirus, both of which are currently being engineered as vaccine carriers. The

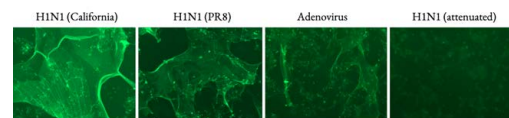


Figure 3. Images taken on EVOS FL Auto

- [1]. Flerlage, T., Boyd, D. F., Meliopoulos, V., Thomas, P. G., & Schultz-Cherry, S. (2021). Influenza virus and SARS-CoV-2: pathogenesis and host responses in the respiratory tract. *Nature Reviews Microbiology*, 1-17.
- [2]. McCracken, I. R., Saginc, G., He, L., Huseynov, A., Daniels, A., Fletcher, S., ... & Randi, A. M. (2021). Lack of evidence of angiotensin-converting enzyme 2 expression and replicative infection by SARS-CoV-2 in human endothelial cells. *Circulation*, 143(8), 865-868.
- [3]. Friedman, H. M., Macarak, E. J., MacGregor, R. R., Wolfe, J., & Kefalides, N. A. (1981). Virus infection of endothelial cells. *Journal of Infectious Diseases*, 143(2), 266-273.

The Effectiveness of P12: A Potential Anti-Thrombogenic Drug for COVID-19

Nicole Gabriel¹, Aarushi Mehrotra², Jia Lu (Angela) Sun³, Sneha Sunder⁴, Serena Yang⁵, Anthony Deluxe⁶, & Kao Li⁷

¹South Side High School, Rockville Centre, NY 11570; ²Lynbrook High School, San Jose, CA 95129; ³Lord Byng Secondary, Vancouver, BC V6R 2C9, Canada; ⁴Fairfield Warde High School, Fairfield, CT 06824; ⁵Dougherty Valley High, San Ramon, CA 94582; ⁶New York University, New York, NY 10003; ⁷Stony Brook University, Stony Brook, NY 11794

The phenomenon of vascular occlusion has been commonly found in cases of COVID-19 infection. Vascular occlusion damages the endothelium of blood vessels, leading to blockage related to fibrinogen aggregation and microthrombi formation [1], causing many of the symptoms associated with COVID-19. To form an occlusion, the enzyme thrombin needs to cleave fibrinopeptide A and fibrinopeptide B from fibrinogen's α and β chains [2]. The fibrinogen, now in its active state fibrin, can polymerize by binding to each other's alpha C domain. However, the fibrinogen molecule has a binding site for fibronectin on the alpha C domain at Aa 221-391 [3], and previous research has shown that IgG alpha C binding prevents fiber development [1]. Using this information, we propose that fibronectin-derived oligopeptides such as P12 could prevent fibrin polymerization, and we aim to find the minimum concentration of P12 for such a task.

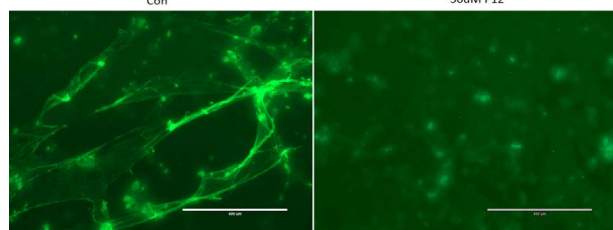


Figure 1. EVOS FL Imaging of Fiber on Control vs. 50 μ M P12 samples

The first step for testing the effectiveness of P12 was to infect human umbilical vein endothelial (HUVEC) cells. The H1N1 (PR8) strain was used, but because endothelial cells don't contain the receptor that allows direct infection, gingival epithelial cells were infected for 24 hours first, and their infected medium was incubated with HUVEC cells for 6 hours. The viral medium was replaced with a 4 mg/mL fibrinogen and 50 μ M P12 solution and incubated for 6 additional hours. The control samples without any P12 had fibers covering almost 80% of the surface while 50 μ M of P12 dropped the fiber area coverage to less than 10% (Figure 1 and Diagram 1), giving evidence supporting further studies of P12 for use clinically.

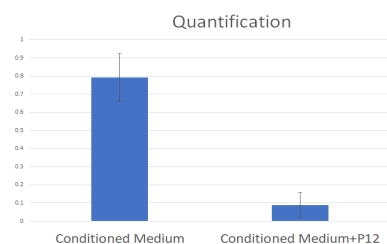


Diagram 1. Proportion of Fiber on Images

To test the minimum P12 concentration needed for these results, four different P12 concentrations were created by diluting the stock 5 mM P12 solution in phosphate-buffered saline (PBS) with 4mg/ml fibrinogen to create 50 μ M, 10 μ M, 2 μ M, and 0.5 μ M solutions. These solutions were mixed using a vortex and after sitting for 10 minutes, 1 mL of the appropriate concentration solution was added onto spun-cast polystyrene on 1 cm x 1 cm silicon wafers. After fibrinogen adsorption overnight, the samples were dried and viewed with an optical microscope and fiber formation was analyzed with the help of AFM imaging. The control sample with no P12, the 0.5 μ M, and 2 μ M all displayed a degree of fiber formation, the 10 μ M had fewer and thinner fibers, and there were hardly any fibers on the 50 μ M sample. Thus, it can be concluded that for in vitro testing, ~10 μ M P12 concentration solution is the threshold for fiber formation, as shown in Figure 2. Figure 2 also shows the height of the tallest fiber and width of the widest fiber produced across all samples of every concentration.

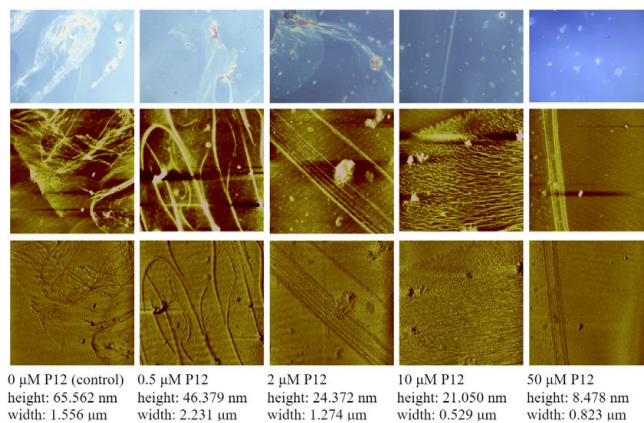


Figure 2. 0 μ M, 0.5 μ M, 2 μ M, 10 μ M, 50 μ M AFM and Optical Microscope Images

- [1]. Clark, Richard AF, et al. *Experimental dermatology* 27.6 (2018): 625-629.
- [2]. Weisel, J. W., & Litvinov, R. I. (2013). Mechanisms of fibrin polymerization and clinical implications. *Blood*, 121(10), 1712–1719. <https://doi.org/10.1182/blood-2012-09-306639>
- [3]. Makogonenko, Evgeny, et al. *Biochemistry* 41.25 (2002): 7907-7913.

Investigating the Atomistic Mechanism of Fibrinogen Inhibition by P12

Sophia Cai¹, LeAnn Tai², Bernard Essuman³, Peng Zhang^{3,5}, Miriam Rafailovich⁴, Yuefan Deng³,
¹Barrington High School, Barrington, IL, 60010, ²Arnold O. Beckman High School, Irvine, CA, 92602, ³Department of Applied Mathematics and Statistics, Stony Brook University, Stony Brook, NY 11794, ⁴Department of Materials Science and Chemical Engineering, Stony Brook University, Stony Brook, NY 11794, ⁵Department of Biomedical Engineering, Stony Brook University, Stony Brook, NY 11794

Fibrinogen is a plasma-soluble glycoprotein responsible for blood clot formation. After an injury to the blood vessels, fibrinogen molecules are polymerized into fibrin through binding and interactions at their α C domains, forming a fibrin mesh that completes a blood clot. Previous studies indicate that excessive coagulation can lead to harmful diseases and health conditions like strokes and pulmonary embolism [1]. P12, a peptide derived from fibronectin, can mitigate fibrinogen formation and reduce thrombogenesis [2]. In this study, we investigated the properties of the interaction between P12 and the α C domain of fibrinogen.

We hypothesized that when interacting, P12 distorts the α C domain so that the α C domains of different fibrinogen molecules are unable to bind with each other, preventing the formation of a fiber network. To test this, an *in silico* model of the α C domain was first created using the molecular dynamics package GROMACS. Potential models of the P12- α C interaction were collected from multiple docking servers, including ClusPro, FRODOCK, and HDOCK. The top models from each server were determined using UCSF Chimera visualization, then further evaluated using the KDeep protein-ligand affinity prediction software. The top scores were all located within residues 518 to 584, which we hypothesized to be the binding site of P12 in the α C domain.

Changes to the α C domain structure were visualized by superimposing its structure with P12 on the domain without P12 (**Figure 1**). To understand the binding interactions between P12 and the α C domain, hydrogen bonding sites were mapped through Cytoscape detection. Six residues displayed hydrogen bonding with the P12 ligand. Furthermore, RMSF calculations were performed by Gromacs to analyze the stability of the P12- α C domain complex. The introduction of P12 increased the overall flexibility of the α C domain complex, as indicated by the higher RMSF values (**Figure 2**).

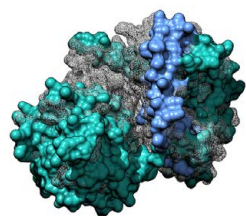


Figure 1. The extent of which the structure of the α C domain was altered is depicted by the mesh structure (produced from UCSF Chimera).

To verify these salt bridges, we will conduct a distance map calculation by creating an index of the applicable residues and mapping out the calculated distances between those residues. The hydrophobicity of the α C domain and P12 complex was mapped using UCSF Chimera to observe the forces that keep the complex intact and determine the degree of hydrophobicity at the P12 binding sites on the α C domain. On both the P12 molecule and the α C domain, the specific sites of interaction were shown to be very hydrophobic.

Although the specific residues in which disulfide bonds are present have been located throughout the fibrinogen molecule in previous studies, it is less specified for the α C domain itself. We intend to analyze the presence of disulfide bonds within the α C domain prior to and after introducing a P12 molecule.

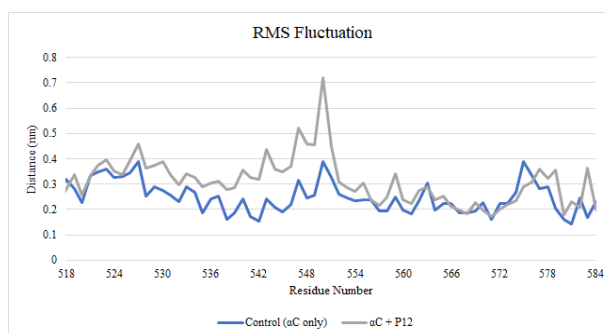
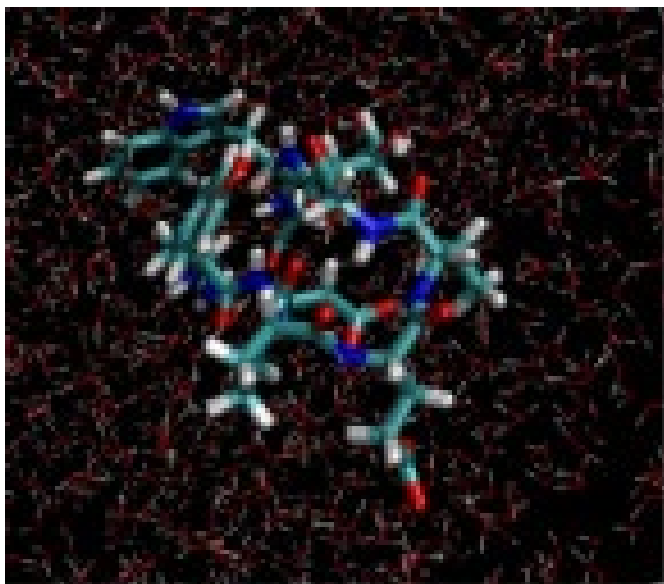


Figure 2. RMSF graph illustrating the changes in flexibility, and therefore stability, of the α C domain with and without P12 binding.

- [1] Jin, Ng Zhang, and Subash C. B. Gopinath. "Potential Blood Clotting Factors and Anticoagulants." *Biomedicine & Pharmacotherapy*, vol. 84, 2016, pp. 356–65. *Crossref*, doi:10.1016/j.biopha.2016.09.057.
- [2] Doilidov, Andrei, et al. "The Effect of P12 Peptide on Fibrinogen Fiber Formation and Endothelial Cell Attachment on Polystyrene." *Journal of Undergraduate Chemical Engineering Research*, 2019, pp. 19–23, cpb-us-e1.wpmucdn.com/you.stonybrook.edu/dist/f/2071/files/2019/05/The_Effect_of_P12_Peptide_on_Fibrinogen_Fiber_Formation_and_Endothelial_Cell_Attachment_on_Polystyrene-3.pdf.

SESSION V:

Modeling and Experiment of SARS- CoV-2 Spike Proteins Under Different Conditions:



Mentors: Ziji
(Jason) Zhang,
Bernard Essuman,
and Won-Il Li

Influence of Temperature and Salt Concentration on Molecular Structure of SARS-CoV-2 Spike Protein Detected Using Potentiometric Sensor

Emily Vaysman¹, Katherine Morse¹, Chloe Lim², Won-Il Lee³, Miriam Rafailovich³

¹Hebrew Academy of the Five Towns and Rockaway, NY 11516, ²Portola High School, CA 92618, ³Department of Materials Science and Chemical Engineering, Stony Brook University, NY 11794

Ever since SARS-CoV-2 was detected in Wuhan China in early December 2019, the world has been experiencing a public health emergency. As the virus spreads worldwide, many SARS-CoV-2 variants have emerged, a common feature of these variants being mutations in the SARS-CoV-2 spike protein, a target for most COVID-19 vaccines. The spike protein is the outermost structural protein of the SARS-CoV-2 virus, which mediates to host cellular receptors human angiotensin-converting enzyme 2 (ACE2) and resulting in viral entry into the host. To precisely understand the spread mechanism of SARS-CoV-2 and develop a spike protein-based therapeutic agent to suppress it, research on the molecular structure of the spike protein according to the external environment is crucial and has not yet been clearly elucidated.

In this study, molecular structural deformations were confirmed by comparing the detection sensitivity according to changes in temperature and salt concentration using a potentiometric sensor that can detect SARS-CoV-2 spike protein in real-time using a three-dimensional surface molecular imprinting technique. The 3D surface molecular imprinting technique imprints hydroxyl-terminated alkanethiol chains and template analytes on the gold surface to form a self-assembled monolayer around the analytes and crystallize into the specific molecular structure of the target molecule. After that, when the template is removed, template-shaped cavities are formed, and when an analyte is injected, the target molecule is re-adsorbed based on its specific structure and conformation. The analyte can be detected by measuring the potential difference generated by re-adsorption using Open Circuit Potential (OCP) measurements. Previous works have shown that the technique could detect Zika virus and accurately discriminate against DENV¹. Furthermore, this technique could selectively detect the spike protein of SARS-CoV-2 and MERS in phosphate-buffered saline and human saliva without any sample manipulation. Due to the specificity of the shape and structure of the imprinted cavities, if there were to ever be a change in the environment that changes the shape of the target biomolecule, a molecular imprinted biosensor would no longer be able to detect it. Therefore, we compared the detection sensitivity according to temperature (20, 37, 56, 60, 70 °C) and salt concentration (0, 0.15, 1.5, 5 M) after manufacturing the MI sensor using pristine SARS-CoV-2 spike protein. In the case of the heat-treated sample, it was confirmed that the detection sensitivity was not affected at less than 40 °C, but it decreased drastically from 56 °C. That is, it can be confirmed that the molecular structure of the spike protein changes from 50 °C, which is consistent with the TEM results (figure 1). In addition, in the case of 70 °C, it was not even detected at all, and it can be inferred that the molecular structure was completely transformed. On the other hand, although the detection sensitivity according to the salt concentration was compared, there was almost no difference. Therefore, it is judged that the salt concentration has little effect on the structural change.

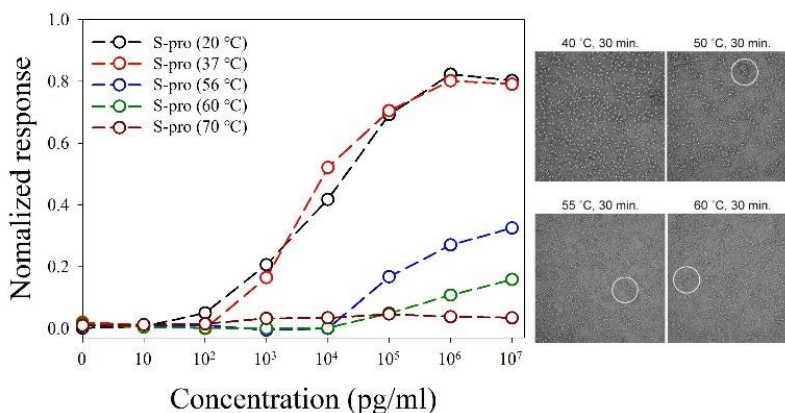


Figure 1. (Left) OCP responses of re-adsorption of heat-treated SARS-CoV-2 spike protein (20, 37, 56, 60, 70 °C) on pristine SARS-CoV-2 spike protein imprinted sensor. (Right) TEM images of heat-treated SARS-CoV-2 spike protein².

¹ Vincent Ricotta et al., A chip-based potentiometric sensor for a Zika virus diagnostic using 3D surface molecular imprinting, *Analyst*, 2019, 144, 4266–4280

² Ching-Lin Hsieh et al., Structure-based design of prefusion-stabilized SARS-CoV-2 spikes, *Science*, 369, 1501–1505 (2020)

Evaluating the Effectiveness of AI-Guided Coarse-Grained Modeling for More Efficient Molecular Dynamics Simulations

Raaghav Malik¹, Ziji (Jason) Zhang², Peng Zhang²

¹Columbus Academy, Gahanna, OH 43021

²Department of Applied Mathematics and Statistics, Stony Brook University, Stony Brook, NY 11794

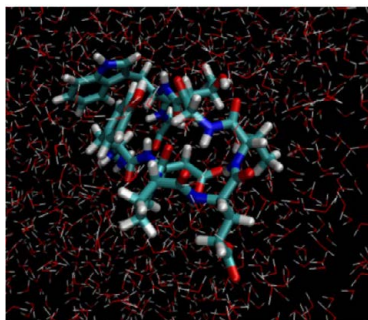


Figure 1: Equilibrated All-Atom Chignolin Model Solvated in Water

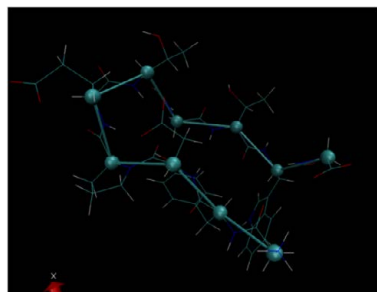


Figure 2: Coarse-Grained Model Overlaid on All-Atom Model

Biological systems are fascinating due to their complex dynamics, and if these dynamics are fully understood, it would pave the way for advancements in targeted drug discovery, tissue engineering, and more natural prosthetics. In fact, the physics behind the atomistic interactions that drive such biological systems are well-studied; Newton's equations of motion lead to fairly accurate molecular dynamic simulations describing the physical movements of atoms and molecules.¹ However, such simulations are far too computationally inefficient for large-scale systems, and quickly become inadequate at the scale of biological cells. In the last decade, a rise in coarse-grained modeling allows for the scaling down in resolution of such systems for more efficient modeling. Coarse-grained modeling simplifies the atomic structure by having multiple closely interacting atoms be represented by a single particle. Such modeling techniques hold promise, yet the most crucial part in retaining accuracy compared to all-atom models is how the parameters for the potential energy function between coarse-grained particles are defined.²

The goal of this project is to investigate a particular usage of machine learning in molecular dynamics: learning the parameters for the potential energy function in coarse-grained molecules, known as force field parameters, for more accurate coarse-graining. Two main techniques in particular were studied: the Iterative Boltzmann Inversion (IBI), serving as a baseline for comparison, and the CGnet framework developed by Wang et al.³ Both methods use information from the all-atom simulation to define the force field parameters. The Iterative Boltzmann Inversion is a popular currently-used technique based on iteratively adjusting the force field parameters based on the ground-truth from the all-atom simulation.⁴ CGnet is an artificial neural network (ANN) model with the inputs as Cartesian coordinates of coarse-grained particles and the output as the potential energy function which is

differentiated to calculate the force on each particle. The parameters of this potential energy function are represented as the weights of the network, and the model is trained to minimize error from the all-atom model using supervised learning.

The molecule that was modeled in this study was the peptide chignolin, due to its relatively small size making the all-atom model as a basis for ground truth easier to compute. The peptide was computationally solvated in a water box, then simulated until it equilibrated, using NAMD⁵ to run the simulation and VMD⁶ to visualize it (Fig. 1). RMSD values were computed for the all-atom model as a reference before doing the coarse-grained analysis. The molecule was then coarse-grained by extracting the alpha carbon atoms, as these are the primary atoms defining the shape and dynamics of chignolin, and a custom topology file was created defining the bonds and angles of the coarse-grained molecule (Fig. 2). Finally, an IBI analysis using RMSD values was performed to compute the coarse-grained force field, and the RMSD was compared to the all-atom case.

Next steps include performing a similar analysis with CGnet and comparing the results. Additionally, a couple major issues were found: the IBI does not account for dihedral angles, leading to drawbacks in accuracy, and it cannot be performed directly on a solvated protein model as the solvent is usually not coarse-grained. Future work will also be done on investigating combining aspects of the IBI with the CGnet framework for improved accuracy.

¹Rahman, A. (1964). Correlations in the Motion of Atoms in Liquid Argon [Abstract]. *American Physical Society*, 136 (2A). <https://doi.org/10.1103/PhysRev.136.A405>.

²*Chem. Rev.* 2016, 116, 14, 7898–7936. Publication Date: June 22, 2016. <https://doi.org/10.1021/acs.chemrev.6b00163>.

³*ACS Cent. Sci.* 2019, 5, 5, 755–767, Publication Date: April 15, 2019, <https://doi.org/10.1021/acscentsci.8b00913>

⁴Moore et al. Derivation of coarse-grained potentials via multistate iterative Boltzmann inversion. *BioChemical Physics* 8 (6), 06B606_1 (2014).

⁵Phillips et al. Scalable molecular dynamics on CPU and GPU architectures with NAMD *Journal of Chemical Physics*, 153:044130, 2020. doi:10.1063/5.0014475.

⁶Humphrey, W., Dalke, A. and Schulten, K., "VMD - Visual Molecular Dynamics", *J. Molec. Graphics*, 1996, vol. 14, pp. 33-38.

Protein-Ligand Binding Affinity Prediction by Multi-Representation based Neural Network

Emirhan Kurtuluş¹, Bernard Essuman², Miriam Rafailovich², Peng Zhang², Yuefan Deng²

¹Cağaloğlu Anatolian High School, Turkey, 34160, ²Stony Brook University

Binding affinity prediction is a key component in many biomolecular applications ranging from drug discovery [1] to biomolecular simulations [2]. Pioneered by energy-calculations, the field is dominated by *in silico* methods due to advantages introduced thereby such as faster evaluation of the proposed model and cheaper experiments. Recently, machine learning applications and deep learning models [3] dominated the field, reducing the required computation time from days to minutes while improving the accuracy.

In this work, we present a state-of-the-art deep learning-based protein-ligand binding affinity prediction model. The proposed model uses three different representations of the given biomolecular system, namely 3D point-cloud, SMILES strings and sequence information. Transformers [4] modules are utilized for processing SMILES strings and sequence information, while for 3D point-cloud a new fully convolutional encoder is introduced. The outputs of these modules are concatenated and fed into a fully convolutional decoder. We find that using three different representations of the biomolecular system is highly superior to single representation networks and hypothesize multi-representation approach not only increases the generalization capabilities and robustness to outliers of the model but also is of high benefit for combating overfitting due to the small size of the annotated data available. Fig. 1 provides an overview of the proposed architecture. All training and evaluations are made on PDBbind v2019 [5] dataset where our model achieves state-of-the-art performance in root mean squared error and Pearson's Correlation Coefficient. Table 1 presents comparisons with the state-of-the-art models.

In spatial encoding, 4D tensor is constructed via extracting 3D coordinates of the atoms alongside a feature descriptor. 19 features are determined to represent an atom, 9 bits (one-hot or all null) encoding atom types: B, C, N, O, P, S, Se, halogen and metal, 1 integer (1, 2, or 3) with atom hybridization, 1 integer counting the numbers of bonds with other heavy atoms, 1 integer counting the numbers of bonds with other heteroatoms, 5 bits (1 if present) encoding properties defined with SMARTS patterns: hydrophobic, aromatic, acceptor, donor and ring, float with partial charge, 1 integer (1 for ligand, -1 for protein) to distinguish between the two molecules.

Our contributions to the literature are threefold: being the first study to utilize three different representations and use them both for regularization and generalization purposes, introducing transformers for the first time to the field, improving the state-of-the-art by a remarkable margin.

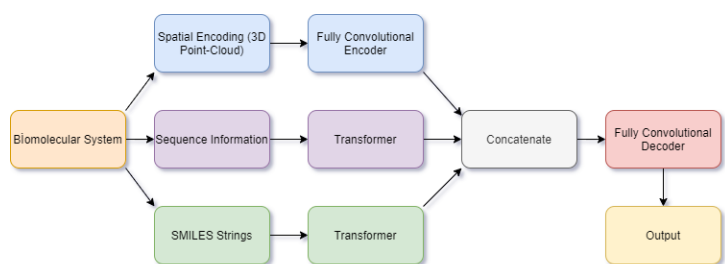


Fig.1 An overview of the proposed model

Model	PCC	RMSE
Ours	0.831	1.192
Kwon, et al., 2020	0.812	1.293
Liu, et al, 2021	0.79	1.44
Jones, et al.,2021	0.532	1.326
Zhu, et al., 2020	0.72	1.55
Bao, et al, 2020	0.74	1.627

Table 1. Comparisons with the SOTA models

[1] Ibrahim, Mahmoud AA, et al. "In silico drug discovery of major metabolites from spices as SARS-CoV-2 main protease inhibitors." *Computers in Biology and Medicine* 126 (2020): 104046.

[2] Batoulis, H., Schmidt, T., Weber, P. *et al.* Concentration Dependent Ion-Protein Interaction Patterns Underlying Protein Oligomerization Behaviours. *Sci Rep* 6, 24131 (2016). <https://doi.org/10.1038/srep24131>

[3] Jiménez, José, et al. "K deep: protein–ligand absolute binding affinity prediction via 3d-convolutional neural networks." *Journal of chemical information and modeling* 58.2 (2018): 287-296.

[4] Vaswani, Ashish, et al. "Attention is all you need." *Advances in neural information processing systems*. 2017.

[5] Su, Minyi, et al. "Comparative assessment of scoring functions: the CASF-2016 update." *Journal of chemical information and modeling* 59.2 (2018): 895-913.

Fogging H1N1 Virus to Quantify the Survival Rate on Various Surfaces

Francis White¹, Timothy Reinholdt², Qianhui Hong³, Kuan- Che Feng⁴, Miriam Rafailovich⁵

¹Houston Christian High School, TX, 77043; ²South Side High School, Rockville Centre, NY, 11570; ³Shenzhen Foreign Languages School, Shenzhen, China, 518000; ⁴Department of Materials Science and Chemical Engineering Stony Brook University, NY, 11794; ⁵Department of Materials Science and Chemical Engineering, Stony Brook University, NY, 11794

The COVID-19 pandemic has made the general public more understanding of threats viruses pose. With that threat comes the interest in how long pathogens are able to survive on surfaces, in the hopes that people are able to minimize potential exposures. Hypochlorous Acid, or HOCL is an endogenous substance found in mammals, and effective against a wide range of microorganisms¹. This research will determine the efficacy of Hypochlorous Acid for eliminating the H1N1 Virus, which is responsible for a highly contagious respiratory disease², and identify the survival rate on various surfaces.

To identify the reduction rate of H1N1, a plaque assay technique was utilized to calculate the PFU of H1N1 virus plated on PLA (Polylactic Acid), Polystyrene (280K), and Aluminum at different timeframes. The samples were allocated into vials with 0.2% BSA in MEM (minimum essential media) and vortexed to promote uniformity. Subsequently, the new virus solution underwent a ten-fold serial dilution to perform a plaque assay. After the MDCK-II cells were 90-95% confluent, the PBS solution was utilized to remove dead cells before adding 250 μ L of virus solution into the wells. The infected plates were placed in a rocking mechanism for 30 minutes, and in an incubator for one hour at 37°C. The virus was then replaced by the gum medium (0.2% BSA, 0.5% TrypLE Select, 1% PenStrep and 25% Tragacanth gum). Lastly, the plates were placed in the incubator for 3 days and later stained with 1% crystal violet, with 4% formaldehyde and 50% methanol dye. The PFU of each well was counted and documented.

In relation to time (in hours), drying in a room temperature environment was significantly more susceptible to viruses surviving than at 4°C, despite the variance in surfaces. For the 24 hour series, PLA—at room temperature—achieved the most resistance to the H1N1 virus with a 2-log reduction. Most notably, an Aluminum surface drying for 48 hours produced a 3-log reduction, which resulted in a 99.9% H1N1 elimination, not nearly effective enough to be considered antiviral (requires at least 4-log or 99.99%) (Figure 1). Therefore, the addition of Hypochlorous Acid, a common disinfectant, was deemed necessary to increase the log reduction of H1N1 on various surfaces.

To establish the disinfecting effect of Hypochlorous Acid, the chlorine concentration was tested at 350 and 510 ppm (low and high). Firstly, the H1N1 virus was deposited on two different surfaces: Polystyrene (280K) and Aluminum. The plated virus samples were then fogged with HOCL at 2.5 minutes, 5 minutes, and 7.5 minutes with a 5 minute interval of rest for the different concentrations. For H1N1 deposited on Aluminum, there was an increasing correlation between log reduction and time (in minutes) for both chlorine concentrations, denoting that longer fogging cycles eliminates more virus particles. Similarly, H1N1 plated on Polystyrene (280K) mimicked the same correlation for the lower chlorine concentration (Figure 2). These preliminary results provide promising evidence that makes hypochlorous acid fogging, a cheap and readily available substance, a potential method of disinfecting with high efficacy.

Figure 1: H1N1 surface interactions

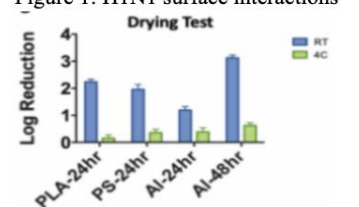
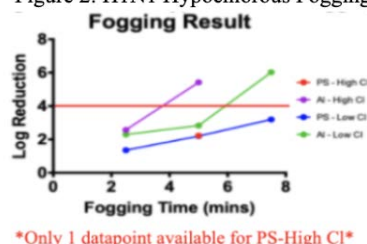


Figure 2: H1N1 Hypochlorous Fogging



¹Block, Michael S, and Brian G Rowan. "Hypochlorous Acid: A Review." Journal of oral and maxillofacial surgery : official journal of the American Association of Oral and Maxillofacial Surgeons vol. 78,9 (2020): 1461-1466. doi:10.1016/j.joms.2020.06.029

²Lee, Spike W., et al. "Risk Overgeneralization in Times of a Contagious Disease Threat." Frontiers in Psychology, vol. 11, 2020, doi:10.3389/fpsyg.2020.01392.

Interactions of Polylactic Acid with the SARS-CoV-2 Spike Glycoprotein Under Varying Temperatures

Erika Flickinger¹, Rebecca Hurwitz², Lydia Wang³, Karin Hasegawa⁴, Miriam Rafailovich⁵, Peng Zhang⁶, Yuefan Deng⁷
¹Saint Teresa High School, Decatur, IL 62526, ²Maine East High School, Park Ridge, IL 60068, ³Great Neck South High School, Great Neck, NY 11020, ⁴Stony Brook University, Stony Brook, NY 11794, ⁵Stony Brook University, Stony Brook, NY 11794, ⁶Stony Brook University, Stony Brook, NY 11794, ⁷Stony Brook University, Stony Brook, NY 11794

Host infection of SARS-CoV-2—the virus that causes Covid-19— occurs when S-protein located outside of the virus bind to host cell's ACE2 protein receptors¹. Scientists can study the S-protein's ability to survive on a common surface by analyzing the interaction between the S-protein and Polylactic Acid (PLA). PLA, a hydrophobic polymer, is commonly used in household items, commercial applications, medical devices, and personal protective equipment². Therefore, data extracted from the interaction between the S-protein and PLA can provide further information that may help develop treatment to protect against individuals' indirect SARS-CoV-2 infection.

The in silico study aimed to observe the binding dynamics and structural changes of the SARS-CoV-2 spike glycoprotein with PLA under 3 different conditions (3°C, 24°C, and 50°C) in a water environment. Principal Component Analysis (PCA) was used to identify the essential intrinsic motions of the S-protein and Root Mean Square Fluctuation (RMSF) was used to identify and investigate the deviations in residues of the S-protein.

RMSF analysis on the 24°C and 50°C showed fluctuations over 1 nm in residues 214, 215, 1146, and 1147 in Chain A, 1138-1147 in Chain B, and 1142-1147 in Chain C for both structures at 24 degrees and 50 degrees. PCA was conducted on the trajectory data from the 24°C and 50°C simulation. For the 24°C simulation, the first two principal components were sufficient in determining the movement of atoms over time, as they represented over 48% of the variance, while the 50°C simulation's first two principal components represented over 35% of the variance. The PCA on the 24°C data had distinct clusters, while the PCA on the 50°C data did not have distinct clusters, with the exception of the earliest frames that represented the starting structure (Fig. 1 & 2).

The PCA on the 24°C and the PCA on the 50°C data suggest that temperature can affect the interactions of PLA and the S-protein, which changes the intrinsic structure of the S-protein. Time Independent Component Analysis (tICA), measurements of phi and psi angles, measurements of the Radius of Gyration, and a creation of a visual comparison between the average and initial structures of the S-protein can be conducted on the data in the future. These analyses help scientists reveal the underlying structural changes in proteins, as the atoms interact with polymers at different temperatures.

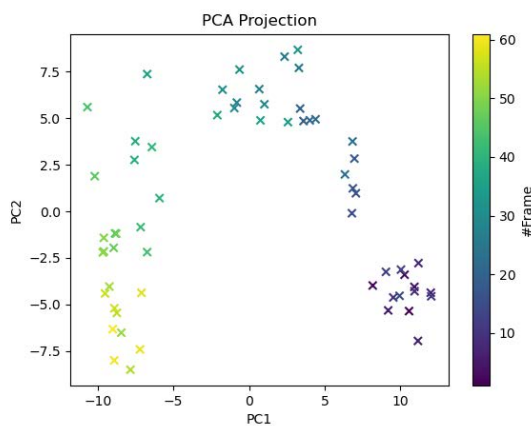


Fig. 1 PCA on the 24°C simulation data.

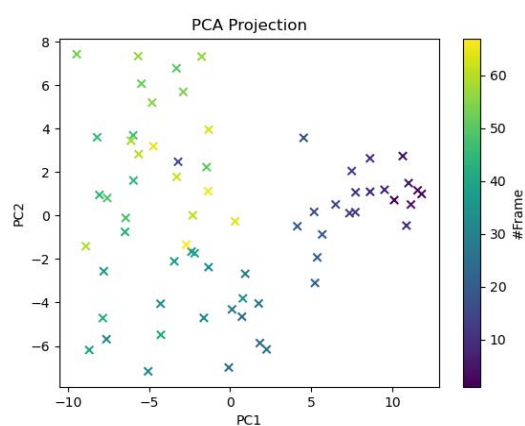


Fig. 2 PCA on the 50°C simulation data.

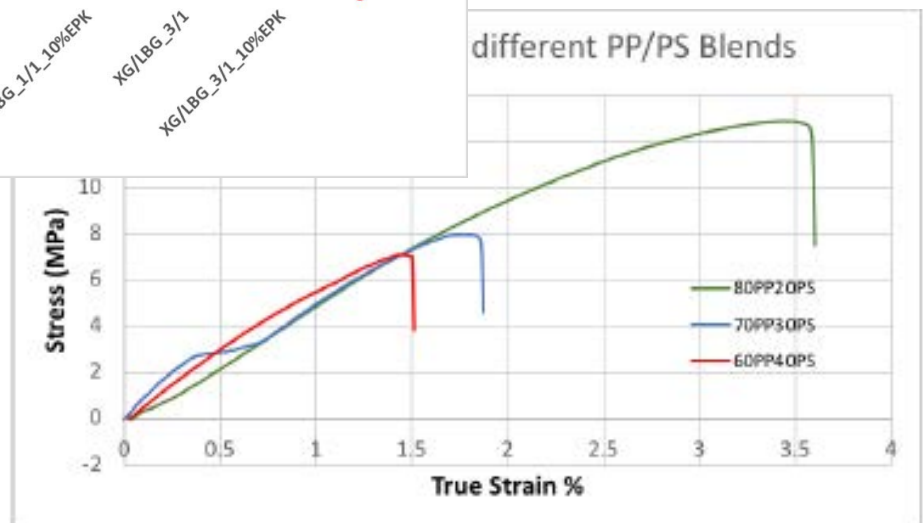
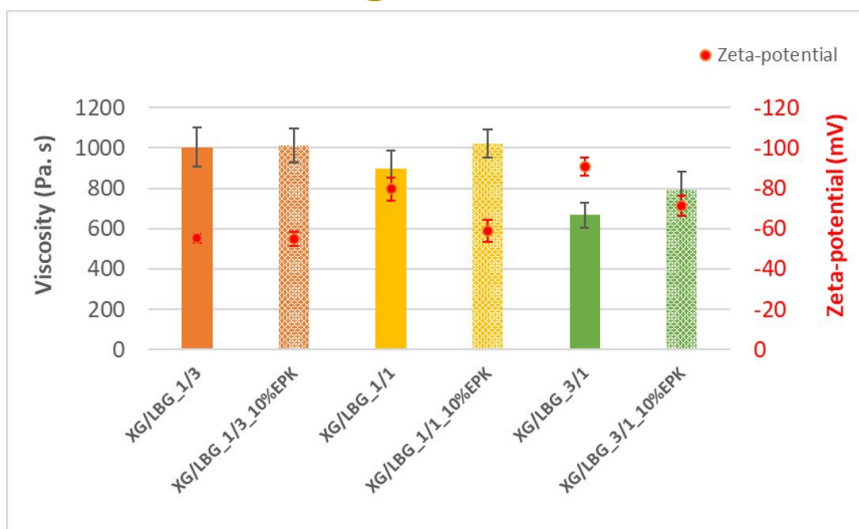
¹He, Yuxian et al. "Receptor-binding domain of SARS-CoV spike protein induces highly potent neutralizing antibodies: implication for developing subunit vaccine." *Biochemical and biophysical research communications* vol. 324,2 (2004): 773-81. doi:10.1016/j.bbrc.2004.09.106

²Farah, Shady, et al. "Physical and Mechanical Properties of PLA, and Their Functions in Widespread Applications — A Comprehensive Review." *Advanced Drug Delivery Reviews*, vol. 107, Dec. 2016, pp. 367–92.

SESSION VI:

Nanocomposites:

Mentors: Yiwei Fang , Yu-Chung Lin, and Dr. Fan Yang



Creating Easily Processable, 3D-printable, and Biodegradable Flame Retardant Polymers

Joshua Kaplan¹, Katerina Popova², Ethan Zuo³, Abhishek Vangipuram⁴, Miffy Liu⁵, Anna Cho⁶, Krish Patel⁷, Vikash Persaud⁷, Yiwei Fang⁷, and Miriam Rafailovich⁷

¹ The Frisch School, Paramus, NJ, 07652, USA, ² Hackley School, Tarrytown, NY, 10591, USA, ³ Saratoga High School, Saratoga, CA, 95070, USA, ⁴ Novi High School, Novi, MI, 48375, USA, ⁵ Shenzhen Middle School, Shenzhen, CN, ⁶ Biomedical Engineering Undergraduate Program, Stony Brook University, Stony Brook, NY, 11794, USA, ⁷ Department of Materials Science and Chemical Engineering, Stony Brook University, Stony Brook, NY, 11794, USA

Being naturally synthesized as an energy storage source by certain bacteria like *Cupriavidus necator*, polyhydroxyalkanoate (PHA) is one of the most biodegradable polymers¹. PHA is truly biodegradable as enzymes and microorganisms can degrade it, unlike other so-called “biodegradable” polymers, such as poly(lactic acid) (PLA), which requires water. Previous research has shown that ammonium polyphosphate (APP) combined with resorcinol bis(diphenyl phosphate) (RDP), which acts as a surfactant, provides optimal flame retardancy and mechanical properties². The main goal of this research study was to engineer a biodegradable, flame-retardant polymer while retaining its strength. A secondary goal was to make this material easily processable and 3D printable.

Several polymer blends were mixed at 180°C with a Brabender and molded with a Carver Hot Press into both rod (5” x ½”) and dog-bone shapes. The rod-molded samples were used for the UL94 20mm Vertical Flame Tests to determine the flame retardancy characteristics of our samples. The dog bone samples were tested in the Instron 5542 Tensile Tester to determine Young’s Modulus and tensile strength; the stress-strain curves produced for each sample were later analyzed. Additionally, the Tinius Olsen Model Impact 104 Plastic Pendulum Impact Tester was used to determine the material’s impact resistance.

Analytical techniques including Fourier Transform Infrared Spectroscopy (FTIR), Differential Scanning Calorimetry (DSC) and Thermogravimetric Analysis (TGA) were used. FTIR confirmed the composition of our blends. Heat effect and crystallization behavior was investigated by DSC, which also obtained the glass transitions of our materials in order to set temperatures for the polymer mixing. TGA determined the thermal stability of the polymers and the char content, a key component of intumescent flame retardants.

Adding APP drastically increases the flame-resistance properties of PHA, however it also reduces the strength of PHA due to its rigidity. As seen in Figure 1, the UL94 result was best for the 90% PHA/10% APP and 95% PHA/5% APP/0.15% RDP samples, earning the best flame retardancy grade V-0. Pure PHA failed the test by dripping, burning the cotton, and not self-extinguishing. The 95% PHA/5% APP with no RDP sample proved slightly flame retardant, more so than pure PHA, but less than the other blends, earning a V-2 grade.

Young’s modulus for pure PHA was higher than that of 90% PHA/10% APP, meaning it was more brittle. The tensile strength of pure PHA was significantly higher than that of 90% PHA/10% APP. We attempted to find a balance between the flame retardant benefits of more APP/RDP and the mechanical properties of having a higher content of PHA. As of writing, we are currently investigating PHB in addition to PHA, as our impact test in Figure 2 showed it had superior mechanical properties (6 times higher average impact resistance in J/m).

Material	T1 (s)	T2 (s)	Dripped?	Cotton burned?	Grade
Pure PHA	Just Burned		Yes	Yes	NG
90% PHA/10% APP	<1	<1	No	No	V-0
95% PHA/5% APP	11	30	Slightly	Yes	V-2
95% PHA 5%APP + 0.15% RDP	2	7	No	No	V-0

Figure 1: UL94 Results for Selected Polymer Blends

Material	Average Impact Strength (J/m)	Tensile Strength (MPa)	Young’s Modulus (MPa)
Pure PHA	20.83±2.32	11.11±1.41	588.91±60.36
90%PHA/10%APP	-	4.92±3.58	566.35±376.84
95%PHA/5%APP	9.90±1.45	-	-
95%PHA/5%APP/RDP	15.55±4.73	-	-
Pure PHB	116.10±7.62	-	-

Figure 2: Impact Test, Tensile Test, and Young’s Modulus Results for Selected Blends

¹ Kim, Y. B.; Lenz, R. W. (2001). "Polyesters from microorganisms". *Advances in Biochemical Engineering/Biotechnology*. 71: 51–79. doi:10.1007/3-540-40021-4_2

² Xue, Yuan, et al. “Enhanced Flame Retardancy of Poly(Lactic Acid) with Ultra-Low Loading of Ammonium Polyphosphate.” *Composites Part B: Engineering*, vol. 196, 2020, p. 108124., doi:10.1016/j.compositesb.2020.108124.

Optimizing the PP/PS Blends for Conductive Polymer 3D Printing

Forest Ho-Chen, George School, Newton, PA

Shuhe Liu, Experimental High School Beijing Normal University, Beijing, China

Emma Savov, Mainland Regional High School, Linwood, NJ

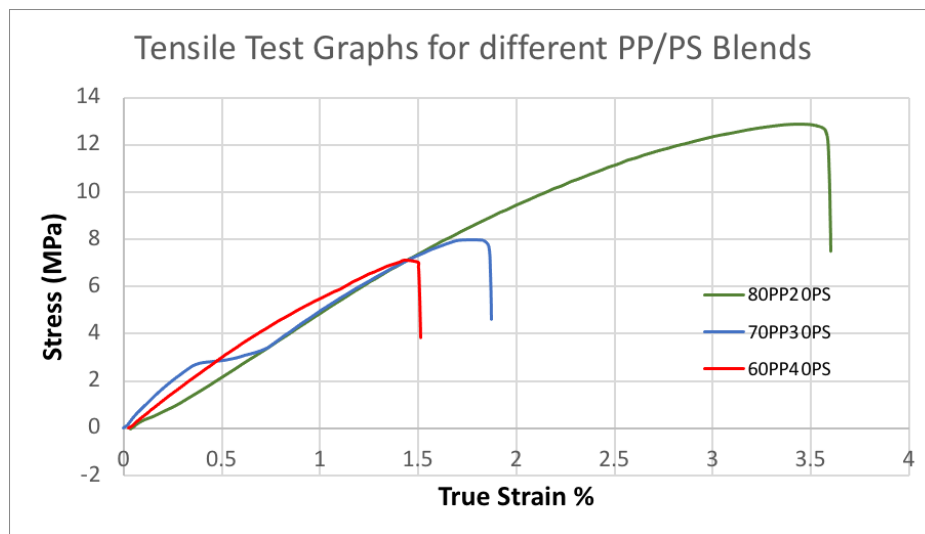
Yu-Chung Lin, Dept. of Materials Science and Chem Eng. Stony Brook, NY

Polypropylene (PP) is a widely used plastic, and because it is conformal to Graphene Nanoplatelets (GNPs), PP is a wonderful carrier of it for conductive components. However, PP doesn't readily adhere to most materials, which limits its usage in 3D printing [1].

We aim to blend PP/PS together to avoid the brittleness of PS and adhesion problems of PP due to the shrinkage by crystallization. Strong mechanical properties and electrical conductivity can be acquired from the blends to print circuits. Because GNPs will be incorporated into the blends for thermal and electrical conductivity, the ratio of PP is controlled to decrease the GNP loading.

We mixed three blends of PP and PS with 80/20, 70/30, and 60/40 ratios using the C.W. Brabender. These were put into a pelletizer and a Filabot Extruder to turn the blends into a filament for 3D printing. After this, we printed multiple samples using the Ultimaker 2 Extended 3D printer to test the printability of the samples and to perform the tensile tests on the samples.

The blends have similar torque and rheological properties. Additionally, the rheology of all three blends is very similar to the rheology of pure polypropylene. The data showed that the mechanical properties including the toughness and the ultimate tensile strength were significantly higher for the 80PP20PS blend in comparison to the 70PP30PS and 60PP40PS blends. However, the Young's Modulus was similar for all three blends. As shown in figure 1, the 80PP20PS blend could be stretched significantly more before breaking in comparison to the other blends.



For the future, we will incorporate GNPs into the blends to test the electrical and thermal conductivity to determine whether an electrical circuit can be 3D printed using polymers. We will also perform impact tests on the samples.

Figure 1: Stress vs Strain graphs from the tensile tests showing

that the 80PP20PS blend has stronger mechanical properties than the 70PP30PS and 60PP40PS blends.

[1] Bachhar, Nirmalya, et al. "3D Printing of Semicrystalline Polypropylene: Towards Eliminating Warpage of Printed Objects." *Bulletin of Materials Science*, vol. 43, no. 1, 2020, doi:10.1007/s12034-020-02097-4.

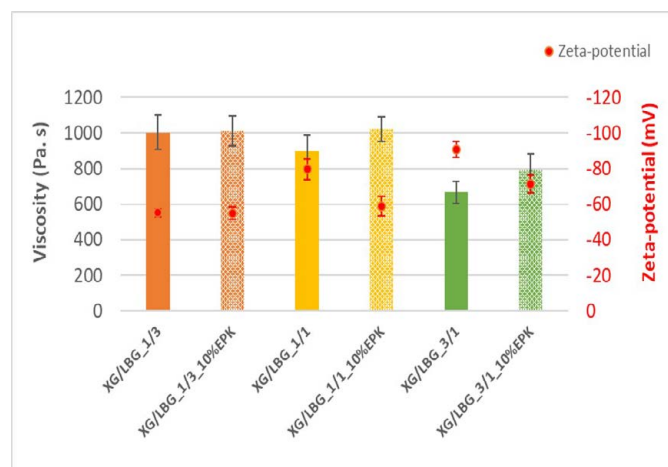
Implications of modifying the rheology of *Rhizobium tropici* EPS

Grace Wang¹, Emily Xiao², Olias Christie³, Vikash Persaud³, Fan Yang³

¹Lexington High School, Lexington, MA 02420, ²Alexander Mackenzie High School, ON L4S1S9, ³Department of Material Science and Chemical Engineering, Stony Brook University, Stony Brook, NY 11794

Rhizobium tropici (ATCC 49672) is a bacterium attached to the roots of leguminous plants and produces nodules that convert nitrogen in the atmosphere to ammonia. The *Rhizobium tropici* species are gram-negative, aerobic, rod-shaped bacterium that are 0.5 to 0.7 by 1.5 to 2 μm [3]. *Rhizobium tropici* uses plant sugars (carbohydrates) to produce an extracellular polymeric substance (EPS), a biopolymer, which can be implemented as an additive to increase the viscosity of substances, such as aqueous solutions [1]. It is of great interest to take advantage of these naturally developed biopolymers and use them beyond the simple symbiotic advantages between legumes and rhizobial microbes. There are many applications of biopolymers in the civil, agricultural, and military sectors. Our project aims to improve upon the physical properties of soil in order to create more sustainable training grounds, detect soil disturbances, and suppress dust formation for the military.

To effectively alter the physical properties of the *Rhizobium tropici* EPS and ultimately increase the substance's overall viscosity, we sought to modify the biopolymer's surface charge. We hypothesized that by adjusting the surface charge of a biopolymer (i.e. the zeta potential), it would alter the biopolymer's viscosity. More specifically, as the zeta potential of a biopolymer decreases, the viscosity of a biopolymer increases. We aimed to confirm this hypothesis first by measuring the viscosity of Xanthan Gum and Locust Bean Gum mixtures with Edgar Plastic Kaolin (EPK) clay and halloysite clay with varying characteristics. We then sought to correlate these measurements to the solutions' resulting zeta potentials. To test our hypothesis, six solutions were prepared. These solutions consisted of mixtures of xanthan gum and locust bean gum with the following specifications: XG/LBG 1:3, XG/LBG 1:3 with 10% EPK clay, XG/LBG 1:1, XG/LBG 1:1 with 10% EPK clay, XG/LBG 3:1, XG/LBG 3:1 with 10% EPK clay. Mixing biopolymers forms a supra-molecular structure which strengthens the biopolymer mesh network and increases viscosity [2]. The viscosity measurements of the six solutions were performed using a DHR-2 rheometer. Furthermore, a bioreactor was constructed to synthesize a stock of *Rhizobium tropici* EPS. We will continue to perform tests to characterize the *Rhizobium tropici* EPS via differential scanning calorimetry (DSC), Thermogravimetric analysis (TGA), scanning electron microscopy (SEM) and Raman spectroscopy.



Since clay is negatively charged, adding it into the relatively neutral 1:1 XG/LBG mixtures increases viscosity, as seen in Figure 1. Also, adding clay into the slightly positive 1:3 XG/LBG mixtures tends to increase the viscosity. In the slightly negative 3:1 XG/LBG mixtures, the clay tends to increase the viscosity as well. When clay neutralizes the excess positive charge of the biopolymer samples, it increases the content of neutral particles, leading to increased Van der Waals interactions. From these observations, it is apparent that altering the zeta potential of the *Rhizobium tropici* EPS can serve as a potential method for modifying the biopolymer's viscosity and enhance its application for the military and beyond.

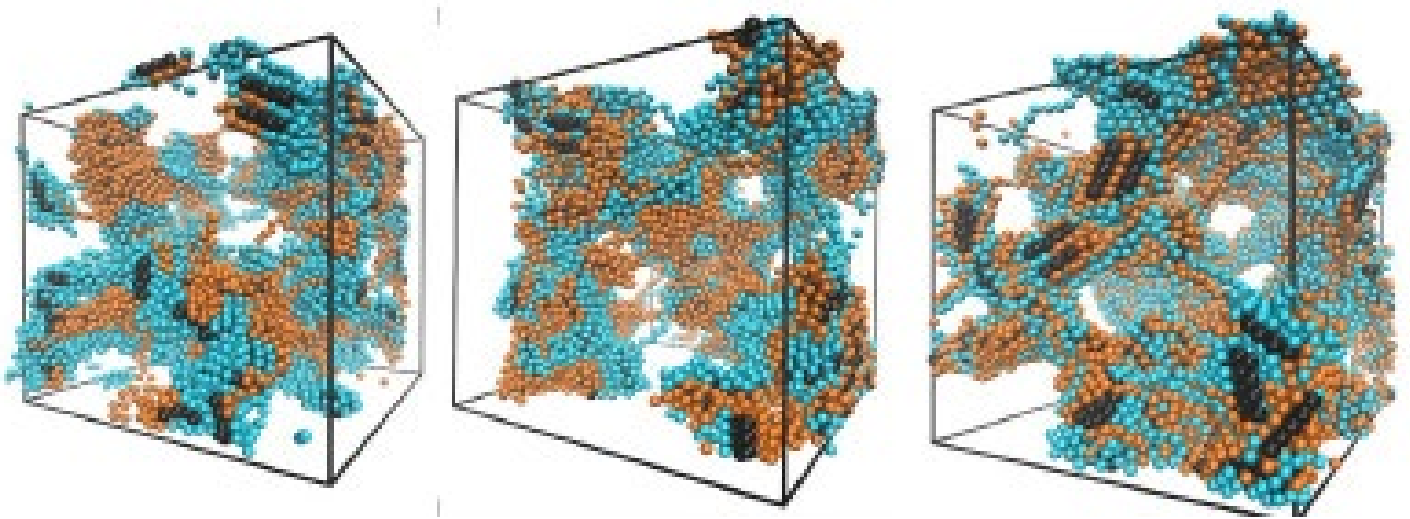
Figure 1. Correlation of zeta potential and viscosity measurements for mixtures of XG, LBG, and EPK clay.

1. Castellane, T. C., et al. "Evaluation of the Biotechnological Potential of *Rhizobium Tropici* Strains for Exopolysaccharide Production." *Carbohydrate Polymers*, vol. 111, 2014, pp. 191–197., doi:10.1016/j.carbpol.
2. Garcia-Ochoa F., Casas J.A. "Viscosity of locust bean (*Ceratonia siliqua*) gum solutions." *Wiley Online Journals*, vol. 59,1 (1992), pg 97-100. doi:10.1002/jsfa.2740590114
3. Martinez-Romero, E. et al. "*Rhizobium tropici*, a novel species nodulating *Phaseolus vulgaris* L. beans and *Leucaena* sp. trees." *International journal of systematic bacteriology* vol. 41,3 (1991): 417-26. doi:10.1099/00207713-41-3-417

SESSION VII:

Nanocomposite Modeling & Simulation:

Mentors: Shoumik Saha and Zhuolin Xia



Designing Copolymers for Reducing Interfacial Tension in Polymer Blends using Coarse-Grained Molecular Dynamics

Albert Tam¹, Nathra Ramrajvel², Shoumik Saha³, Dilip Gersappe³, Miriam Rafailovich³

¹Lynbrook High School, San Jose, CA 95129, ²Naperville Central High School, Naperville, IL 60540, ³Stony Brook University, NY 11794

Blends of different polymers can supply a number of distinct advantages over single polymers, such as enhanced cost effectiveness and the ability to tune critical characteristics such as rigidity and elasticity [1]. However, phase separation in polymer blends leads to the formation of unstable polymer-polymer interfaces, sources of tension that can compromise the stability of the blend.

Past work has focused on the use of diblock copolymers for use in polymer blends to alleviate interfacial tension. Here, we consider copolymers consisting of alternating monomers, and copolymers consisting of randomly arranged monomers. To simulate their effects on polymer blends, we used LAMMPS [2], a software package for

coarse-grained molecular dynamics simulations. For each type of copolymer, systems representing polymer blends were initialized at 1%, 2%, 3%, and 4.5% copolymer by volume. Pressure profiles by layer as well as velocity profiles under shearing were constructed for each system.

The pressure profiles (Fig. 1) of the alternating copolymers demonstrate that interfacial tension within the blend decreases with increasing concentration of copolymer by up to 30% between the 1.0% blend and 4.5% blend. Visualization also revealed that copolymers tended to clump toward the center of the blend and orient horizontally.

Similarly, the random copolymer system (Fig. 2) also showed an increase in interfacial tension correlated with a decrease in the volume percentage of the copolymer. The interfacial tension for the 1.0% blend is about 1.4x that of the 4.5% blend. The velocity profile under shearing indicated that the general trend is that higher concentrations have smaller velocities and are therefore slightly more resistant to shearing. The random copolymers, indicated by the blue and pink beads in Figure 2, tended to gravitate towards the center of the interface between the two polymers as well.

Although the alternating and random copolymer blends had similar pressure profiles, there were some small differences. For the same concentrations, the random copolymers had slightly higher interfacial tension values than the alternating copolymers for every z-coordinate. Alternating copolymers are shown to be more effective in reducing interfacial tension.

Overall, alternating and random copolymers appear to alleviate interfacial stress and have the potential to be viable options for improving the stability of polymer blends. Future work could include testing systems at more levels of phase separation, comparing simulated results to experimental outcomes, and exploring alternative

algorithms for designing copolymer compatibilizers that also take into account the composition of the polymers.

[1] Lyatskaya, Y., Gersappe, D., Gross, N. A., & Balazs, A. C. (1996). *Designing Compatibilizers To Reduce Interfacial Tension in Polymer Blends*. *The Journal of Physical Chemistry*, 100(5), 1449–1458.

[2] S. Plimpton, *Fast Parallel Algorithms for Short-Range Molecular Dynamics*, *J Comp Phys*, 117, 1-19 (1995).

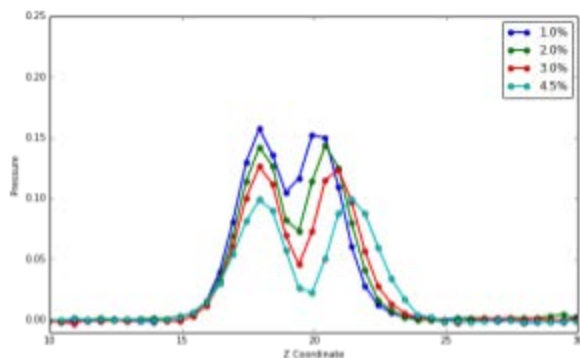


Figure 1. Layer pressure vs. z-coordinate in polymer blends with alternating copolymers. Percentages represent the % of copolymer by volume in each blend.

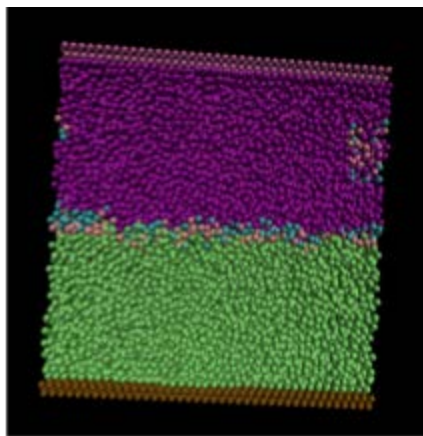


Figure 2. Visualization of the random copolymer system, consisting of two polymer layers interspersed with copolymers.

Simulating the Transport of Ions in Solid Electrolytes Using the Lattice-Boltzmann Method

Jack Kugler¹, Aishik Dhori², Satvik Lolla³, Zhuolin Xia⁴, Dilip Gersappe⁴

¹Phillips Exeter Academy, Exeter, NH 03833; ²Munster High School, Munster, IN 46321; ³Poolesville High School, Poolesville, MD 20837; ⁴Department of Materials Science and Chemical Engineering, Stony Brook University, Stony Brook, NY, 11794

The Lattice-Boltzmann method (LBM) is a powerful simulation technique that tracks the evolution of groups of particles in order to provide effective and computationally efficient fluid dynamics models. The Lattice-Boltzmann method was applied to simulate the flow of lithium cations through a solid electrolyte. All-Solid-State Batteries (ASSBs), which contain solid electrolytes, could have a greater energy density than traditional lithium-ion batteries with liquid electrolytes. Furthermore, solid electrolytes are considered safer than their liquid counterparts, which are flammable and volatile.¹ However, a major challenge facing solid electrolytes such as Lithium Phosphorus Sulfide (LPS) is that they have complicated porous geometries and multiple phases with different ion transport abilities.² Our research uses LBM to simulate the ion transport process through solid electrolytes in a constant electric field.

In our simulations, we modeled lithium-ion transport through solid electrolytes in environments with varying porosities and diffusivities. The system we used measures 0.1 mm in the x-direction, 0.032 mm in the y-direction, and 0.032 mm in the z-direction. Initially, there is an ion flux at the interface between the counter-electrode and electrolyte and no mobile ions elsewhere. In order to measure the transport of ions through the electrolyte, we maintain the constant flux at the inlet and calculate the flux of lithium ions at the interface between the working-electrode and electrolyte. The simulation calculated flux every millisecond for 10000 milliseconds.

The different porosity values tested were 0% porosity, 10% porosity, 20% porosity, and 30% porosity. Porosity is modeled so that ions are unable to travel through a certain percentage of the nodes. The varying diffusivity values tested were $3.13\text{E-}4\text{ cm}^2/\text{s}$, $3.13\text{E-}5\text{ cm}^2/\text{s}$, and $3.13\text{E-}6\text{ cm}^2/\text{s}$. The changing diffusivity values are representative of different solid phases. It was observed that the flux of the system equilibrates to higher values with higher porosities when diffusivity is lower, either $3.13\text{E-}6\text{ cm}^2/\text{s}$ or $3.13\text{E-}5\text{ cm}^2/\text{s}$. However, for the higher diffusivity value of $3.13\text{E-}4\text{ cm}^2/\text{s}$, the higher porosity values initially start out as having greater flux, but in the latter stages of the simulation, the flux of the lower porosity electrodes is actually greater (Fig. 1).

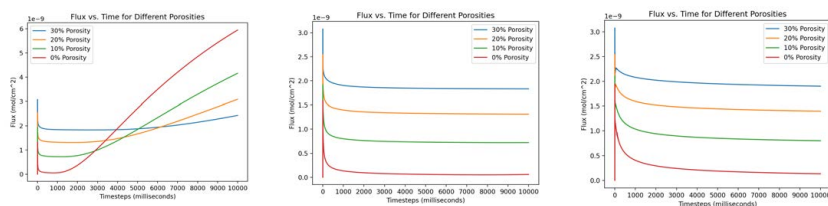


Fig. 1: (1a, left) Flux vs. Time graph for different porosities at a diffusivity of $3.13\text{E-}4\text{ cm}^2/\text{s}$ (1b, middle) Flux vs. Time graph for different porosities at a diffusivity of $3.13\text{E-}5\text{ cm}^2/\text{s}$ (1c, right) Flux vs. Time graph for different porosities at a diffusivity of $3.13\text{E-}6\text{ cm}^2/\text{s}$

It was observed that when the porosity is constant, the flux values for the diffusivity of $3.13\text{E-}6\text{ cm}^2/\text{s}$ are greater than $3.13\text{E-}5\text{ cm}^2/\text{s}$. However, the flux values for the diffusivity of $3.13\text{E-}4\text{ cm}^2/\text{s}$ initially start lower than the other diffusivity values before the flux increases to become greater in the later part of the simulation (Fig. 2). In all of the simulations, the initial increase in flux is caused by incoming ions being reflected by the working electrode. The initial decrease is caused by diffusion and adsorption at the interface. In the future, we plan to study the effects of electrostatic force, run the simulation over longer time intervals, and simulate multiple phases to better understand ion transport through solid electrolytes.

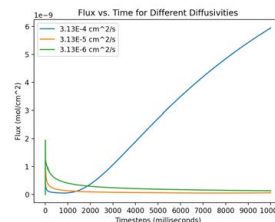


Fig. 2: Flux vs. Time graph for different diffusivities at porosity of 0%

¹ Lim, Hee-Dae, et al. "A Review of Challenges and Issues Concerning Interfaces for All-Solid-State Batteries." *Energy Storage Materials*, vol. 25, Mar. 2020, pp. 224–250. *ScienceDirect*, doi:10.1016/j.ensm.2019.10.011.

² Lau, Jonathan, et al. "Sulfide Solid Electrolytes for Lithium Battery Applications." *Advanced Energy Materials*, vol. 8, no. 27, 25 Sept. 2018, doi:https://doi-org.proxy.library.stonybrook.edu/10.1002/aenm.201800933.

Investigating the effect of interface morphologies on dendrite formation in lithium-metal batteries via the Lattice-Boltzmann Method

Neha Basu¹, Anirudh Bharadwaj², Zhuolin Xia³, Dilip Gersappe³, and Miriam Rafailovich³

¹BASIS Scottsdale, Scottsdale, AZ 85259, ²Lynbrook High School, San Jose, CA 95129, ³Department of Materials Science & Engineering, Stony Brook University, Stony Brook, NY 11794

Lithium has long been considered as a potential anode material in batteries, as it has numerous physical properties that make its use in batteries ideal, from a high specific capacity, to a negative redox potential [1]. Despite these advantages, it has never made the leap to commercial applications. The primary reason for its impracticality is the issue of dendrite growth on the lithium surface, which can lead to performance failures that destroy the battery [2]. Different surfaces can promote or suppress lithium dendrite deposition on the anode of Li metal secondary batteries. Our goal is to identify the surface that best suppresses such deposition.

In this study, we aimed to determine what solid electrode-electrolyte interface pattern would best mitigate dendrite growth in a half-cell with a Li working electrode, virtual Li counter electrode, and LPS solid electrolyte. We simulated this system through the Lattice Boltzmann Method (LBM). We modeled 2 systems – rough and micropatterned electrode/electrolyte interface, as shown in Fig. 1. For each system, we analyzed the fraction of Li at each node, potential of the half-cell, Li ion concentration distribution and density, and surface area of the working electrode. By viewing the Li fraction and reaction layer data, we verified the structure of our cell, including any patterns applied to the electrode-electrolyte interface. We ran our simulations with constant current charge, and consequently, the potential over time was the same for the rough and micropatterned systems. We compared dendrite growth between the 2 systems using the Li fraction, density, and surface area data. Visualizing the Li fraction and density files qualitatively showed us the growth of dendrites at the electrode-electrolyte interface. These results were confirmed quantitatively by the increasing surface area over time for a random lattice, indicating dendrite growth, and constant surface area over time for our micropatterned system.

Our results revealed that dendrite formation at the interface is quite apparent in the random lattice, confirming fears over dendrite growth in lithium-metal batteries. However, it also appears that dendrite growth is inhibited in the presence of a micropattern at the interface. This result represents a major advance in regard to lithium-metal batteries, as the suppression of dendrite formation, which we observed when the simulation was run with the micropattern, would result in lithium-metal batteries becoming a high performing and commercially viable option. Our next step is to simulate different micropatterned interfaces, that may vary in all three dimensions, and explore their resultant effect on dendrite formation, with an aim of ultimately finding the micropattern most efficient at inhibiting dendrite growth.

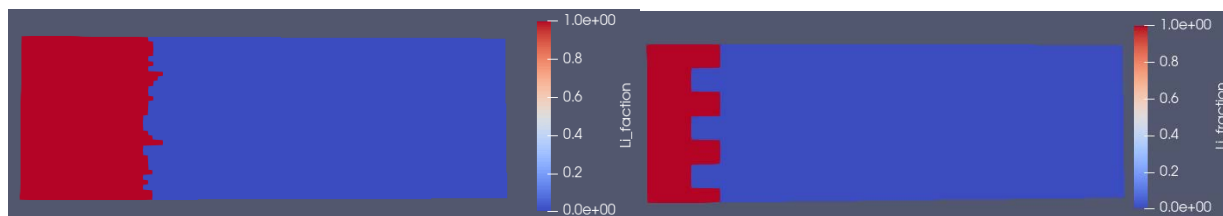


Fig. 1. (A) ParaView visualization of Li fraction output for random lattice; (B) ParaView visualization of Li fraction output for micropatterned lattice

[1] Zhang, Xinyue et al. "Dendrites in Lithium Metal Anodes: Suppression, Regulation, and Elimination." *Accounts of chemical research* vol. 52,11 (2019): 3223-3232. doi:10.1021/acs.accounts.9b00437

[2] Park, Joonam, et al. "Micro-Patterned Lithium Metal Anodes with Suppressed Dendrite Formation for Post Lithium-Ion Batteries." *Advanced Materials Interfaces*, vol 3, no. 11, doi:10.1002/admi.201600140.

Using Coarse-Grained Molecular Dynamics to Model Rheological Properties of Hydrogels with Rigid and Bonded Clay Fillers

Varun Nimmagadda¹, Shoumik Saha², Dilip Gersappe²

¹University of Michigan, Ann Arbor, MI 48109, ²Stony Brook University, Stony Brook, NY 11794

In recent years, much study has been put into the field of polymer blends, which are formed from the mixture of two or more different polymers. In comparison to homopolymers, these blends can provide improved and more desirable structural and rheological properties such as rigidity, elasticity, and viscosity[1]. However, polymer blends can often be difficult to produce due to phase separation, which causes instability and a non-homogenous blend. As a result, compatibilizers such as clay fillers are used to help synthesize polymer blends with the desired enhanced properties[2]. Among other applications, the use of clay fillers in polymer blends has shown potential to be a replacement for using cement as a soil additive to improve soil stability[3]. However, while experiments have successfully demonstrated the positive effect of hydrogels on soil strength, the effect of various types and amounts of clay fillers on the rheological properties of hydrogel blends is still not well understood.

The goal of this study is to assess the mechanical and structural properties of hydrogels consisting of two types of polymer chains (A and B) and clay nanoplatelets dispersed in an explicit water solvent. It was also to determine the difference in properties between bonded and rigid clay nanoplatelet fillers with different levels of filler percentage and attraction between A and B polymers. To simulate the formation and behavior of the polymer blends, the systems were studied using coarse-grained molecular dynamics in LAMMPS software. Simulations were run with 0.00%, 0.74%, 1.46%, 2.17%, and 2.88% bonded and rigid filler by volume in systems with A-B energy interaction parameters (E_{ab}) of 0.7, 1.0, and 1.5. Various means of analysis including modeling the Viscosity, Stress Autocorrelation (SAC), Means Squared Displacement (MSD), Non-Gaussian Parameter (NGP), and Radial Distribution Function (RDF) were then used to infer properties of the different systems.

Figure 1 shows the viscosity of the hydrogels at increasing levels of bonded clay fillers at different E_{ab} values. The graphs show a larger percentage of clay fillers by volume is positively correlated to higher levels of viscosity, and that stronger levels of polymer A – polymer B attraction also tends to increase viscosity. Figure 2 shows visualizations of the hydrogels at different E_{ab} values. In systems with E_{ab} values of 0.7 and 1.0, the two polymers tend not to mix and phase separate. However, with stronger attractive forces when E_{ab} equals 1.5, the system tends to form an interpenetrating network with stronger properties.

Overall, clay nanoplatelet fillers were shown to be successful in positively altering the properties of hydrogels, showing potential for this method being usable to create tailor made polymer blends in the future. However, further testing and analysis is needed to examine other properties such as behavior during different shear rates and to compare to experimental data.

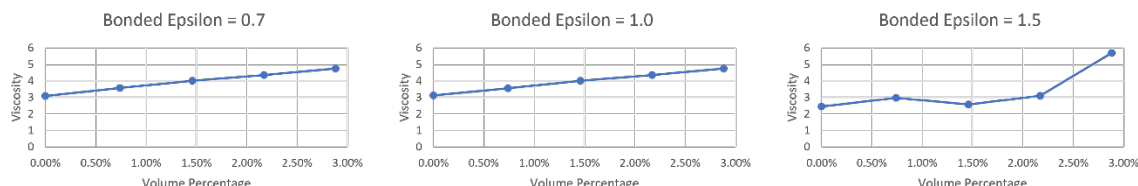


Figure 1: Viscosity values for varying levels of filler percentages in systems with E_{ab} of 0.7, 1.0, and 1.5 respectively.

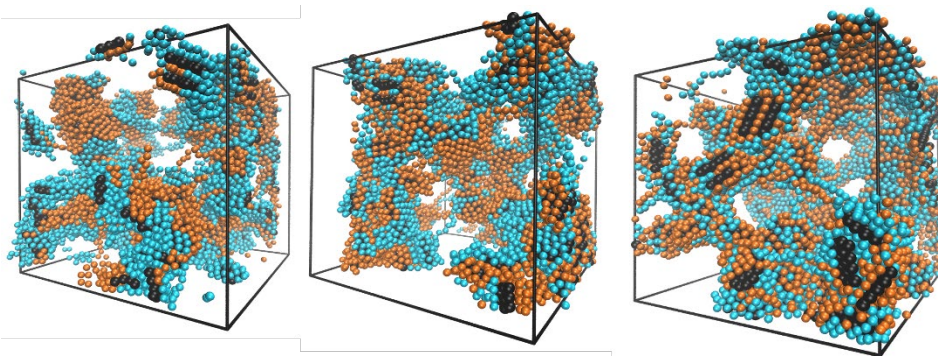


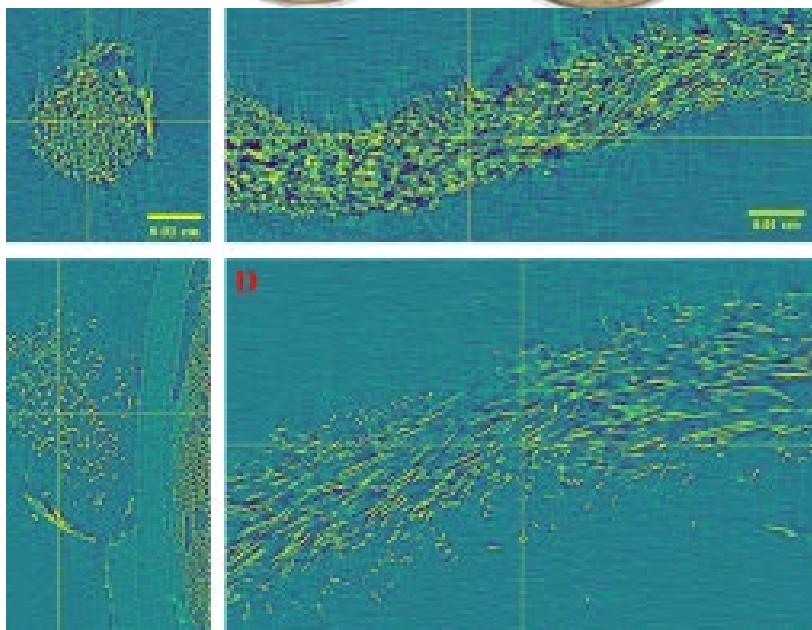
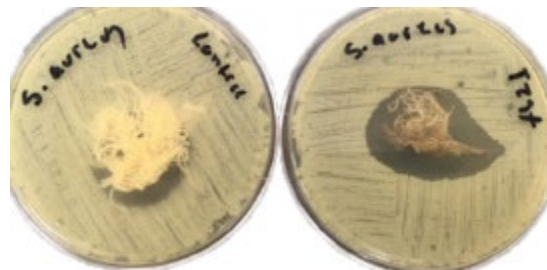
Figure 2: VMD visualizations for systems with E_{ab} of 0.7, 1.0, and 1.5 respectively.

1. Paul, D.R., *Polymer Blends*. Vol. Vol 1. 2012: Elsevier
2. Xu, D. et al. "Rheology of Poly(N-isopropylacrylamide)-Clay Nanocomposite Hydrogels." *Macromolecules* Sept. 12 2019
3. Zhao, Zhi, et al. "Biomimetic Hydrogel Composites for Soil Stabilization and Contaminant Mitigation." *Environmental Science & Technology*, vol. 50, no. 22, American Chemical Society, Nov. 2016, pp. 12401–10, doi:10.1021/acs.est.6b01285.

SESSION VIII:

Micro-Organisms and Materials:

Mentors: Dr. Michael Cuiffo and Antony
Deluxe



Analysis of microorganisms associated with failed endodontic treatment in fifteen-year-old samples of root canals

Stephen G. Walker, MSc, PhD¹, Antony Deluxe²

¹ Stony Brook University School of Medicine, Stony Brook, NY 11794; ² New York University, College of Arts and Science, New York, NY 10003

Enterococcus faecalis is a bacterium known for its resilience. It has been found to survive harsh conditions such as at 10°C or 45°C, acidic or basic conditions, in ethanol, in hydrogen peroxide, or under UV irradiation.¹ *E. faecalis* is particularly prevalent in infections of the root canal system and is known to survive after being desiccated for long periods.

The aim of this study was to determine if *Enterococcus faecalis* can survive after lying dormant in a desiccated state for 15 years. In a previous study, *E. faecalis* was identified in samples taken from root canals using polymerase chain reactions², and a similar method was used to identify bacteria in this study.

In 2006, teeth with root canals were prepared with samples of *E. faecalis* placed above the root canal to assess the sealing capabilities of the gutta percha. However, this study was canceled, leaving the samples of *E. faecalis* desiccated for 15 years. To recover them, these samples were filled with Brain Heart Infusion broth and incubated for two days at 37°C then plated on KF Streptococcus agar, which is selective for *E. faecalis*. After the agar plates were incubated at 37°C for two days, they were observed for growth. In plates that had growths, samples were taken and prepared for polymerase-chain reaction analysis.

After DNA was extracted, a PCR procedure was carried out in 0.75% agarose gel using 16S rDNA universal primers, which show the presence of any type of bacteria. All isolated samples contained bacteria per these results. Then, another PCR procedure was carried out in 1.5% agarose gel using a 16S rDNA primer specific for *E. faecalis*. This primer results in a band at about 310 base pairs. The results of this assay are shown in Figures 1 and 2; the position of 300 base pairs is marked by arrows in both figures. Figure 2 was edited for clarity. Lanes 7 through 15 contain the isolated samples. Lanes 2, 6, 17, and 18 contain the positive controls. Lanes 3 and 4 contain *S. aureus* and *E. faecium*, respectively, while lanes 5 and 16 contain no DNA.

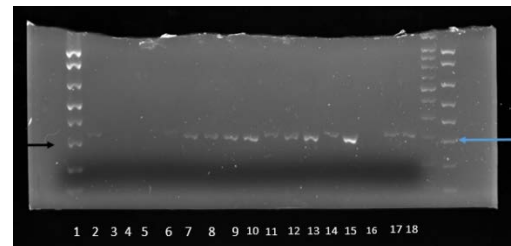


Figure SEQ Figure * ARABIC 1: PCR assay selective for *E. faecalis*

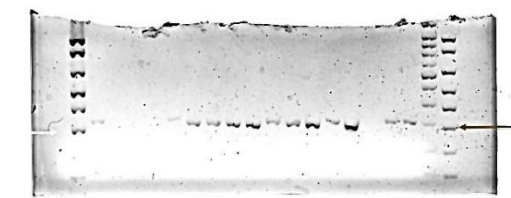


Figure SEQ Figure * ARABIC 2: PCR assay selective for *E. faecalis* (edited)

The strains recovered from the isolated samples are tentatively identified as *E. faecalis*. More testing, such as genome sequencing, is required to verify this claim.

1 Halkai, R., Hegde, M.N., Halkai, K. "Enterococcus faecalis can survive extreme challenges – overview." *Journal of Health and Allied Sciences NU*, Vol. 2, No. 3, doi: 10.1055/s-0040-1703595

2 Siqueira, J.F. and Rocas, I.N. "Polymerase chain reaction–based analysis of microorganisms associated with failed endodontic treatment." *Oral Surg Oral Med Oral Pathol Oral Radiol Endod* 2004; 97:85-94, doi: 10.1016/s1079-2104(03)00353-6

Deweaving Cotton Cloth using Non-Toxic and Environmentally-Friendly Methods

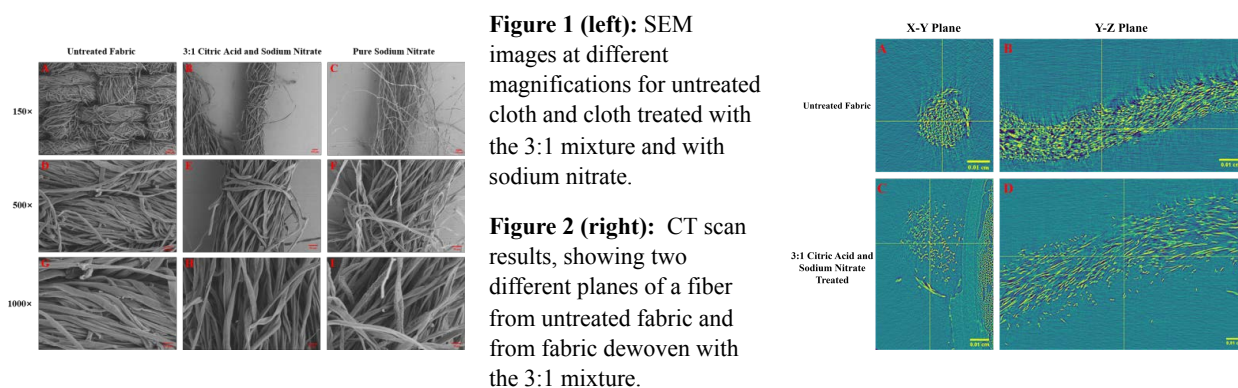
Ayush Agrawal¹, Tianyu Dong², Amanda Xu³, Ivan Yuan⁴, Jacob Zerykier⁵, Elizabeth Zhang⁶, Guanchen Zhu⁷, Michael Cuiffo⁸, David Sprouster⁸ and Miriam Rafailovich⁸

¹Canyon Crest Academy, San Diego, CA 92130; ²Northview High School, Johns Creek, GA 30097; ³The Madeira School, McLean, VA, 22102; ⁴Shanghai High School International Division, Shanghai, China, 200237; ⁵Rambam Mesivta-Maimonides High School, Lawrence, NY, 11559; ⁶Phillips Academy Andover, Andover, MA 01810; ⁷The Experimental High School Attached to Beijing Normal University, Beijing, China, 100032; ⁸Department of Materials Science and Chemical Engineering, Stony Brook University, Stony Brook, NY, 11794

The fashion industry as a whole has a large environmental impact^[1]. Part of this impact comes from the lengthy and complicated supply chain that takes materials such as cotton from plants to garments. This problem has only grown due to the rise of fast fashion. It has been estimated that over 10 million tons of waste cotton cloth are disposed of every year globally^[2]. Though procedures currently exist for cotton recycling, they involve harsh and/or toxic chemicals and often over-degrade cotton into glucose instead of maintaining the cellulose structure^[3]. The goal of this research is to find a more efficient and environmentally-friendly way of deweaving cotton, specifically muslin tailoring cloth, in order for it to be reused or repurposed, thus minimizing waste.

Fabric was first cut diagonally to maximize the number of fibers exposed. These diagonal pieces were then immersed in 40 mL solutions of deionized water, citric acid (0.5 M), sodium hydroxide (0.5 M), sodium nitrate (0.5 M), and urea (0.5 M) to determine the optimal reagent. After stirring the fabric and solution for 15 minutes at 600 rpm and 50 °C, the fabric pieces in citric acid and sodium nitrate had dewoven completely. Citric acid and sodium nitrate were then combined in solution at different ratios to determine the most effective combination. Fabric pieces were immersed in 40 mL solutions with volume ratios (citric acid [0.5 M] to sodium nitrate [0.5 M]) of 1:3, 1:1, 3:1, and 7:1 and stirred for 15 minutes at 600 rpm and 60 °C. The 3:1 combination was the only one in which the fabric was fully dewoven in all tested trials. To differentiate between the solutions that fully degraded fabric—citric acid, sodium nitrate, and the 3:1 by volume mixture—fabric pieces were heated and stirred in each solution for five minutes and then analyzed on petri dishes. The fabric immersed in the 3:1 mixture had the smallest remaining woven area, confirming it to be the most effective solution for deweaving. Afterward, the 3:1 treated fabric was analyzed in thermogravimetric analysis (TGA) to confirm that the treated sample's characteristics still matched those of cotton.

To understand the changes in fiber structures after deweaving, the untreated fabric and the dewoven fibers were analyzed and compared with scanning electron microscopy (SEM, Figure 1), X-ray computed tomography (CT, Figure 2), and X-ray photoelectron spectroscopy (XPS). Comparing Figures 1G and 1H, we may observe how untreated fibers are more tightly packed than dewoven fibers. This is confirmed in Figure 2 through CT analysis. Another observation from SEM is that the fibers dewoven with pure sodium nitrate contain large amounts of salt particles on the surface. In XPS analysis, a low binding energy peak appeared in untreated fabric analysis but not in any of the samples treated with degradation solution. The low binding energy could correspond to an sp^3 to sp^2 transition. This, along with the silicon peaks present, suggests that the fabric was likely coated with a thin layer of hydrophobic material that was easily penetrated by degradation solutions.



^[1] Cuiffo, M., Jung, H.J., Skocir, A. et al. "Thermochemical degradation of cotton fabric under mild conditions." *Fash Text* 8, 25 (2021). <https://doi.org/10.1186/s40691-021-00263-8>

^[2] Mohamed, S.H.; Hossain, M.S.; Mohamad Kassim, M.H.; Ahmad, M.I.; Omar, F.M.; Balakrishnan, V.; Zulkifli, M.; Yahaya, A.N.A. Recycling Waste Cotton Cloths for the Isolation of Cellulose Nanocrystals: A Sustainable Approach. *Polymers* 2021, 13, 626. <https://doi.org/10.3390/polym13040626>

^[3] Gao, Lixia. "NaOH/Urea Swelling Treatment and Hydrothermal Degradation of Waste Cotton Fiber." *Journal of Renewable Materials*, vol. 8, no. 6, 2020, pp. 703–13, doi:10.32604/jrm.2020.09055.

Functionalizing Fibers from Cotton Cloth Deweaved Using Sodium Nitrate and Citric Acid Solutions

Ayush Agrawal¹, Tianyu Dong², Amanda Xu³, Ivan Yuan⁴, Jacob Zerykier⁵, Elizabeth Zhang⁶, Guanchen Zhu⁷, Michael Cuiffo⁸, Stephen Walker⁹ and Miriam Rafailovich⁸

¹Canyon Crest Academy, San Diego, CA 92130; ²Northview High School, Johns Creek, GA 30097; ³The Madeira School, McLean, VA 22102; ⁴Shanghai High School International Division, Shanghai, China 200237; ⁵Rambam Mesivta-Maimonides High School, Lawrence, NY 11559; ⁶Phillips Academy Andover, Andover, MA 01810; ⁷The Experimental High School Attached to Beijing Normal University, Beijing, China 100032; ⁸Department of Materials Science and Chemical Engineering, Stony Brook University, Stony Brook, NY 11794, ⁹ Dept. of Oral Biology and Pathology, Stony Brook University, NY 11794

Using non-toxic and environmentally friendly techniques, cotton fabrics can be broken down into centimeter-scale fibers that can be repurposed^[1]. Here, we investigate repurposing unwoven fibers for the synthesis of silver nanoparticles and the preparation of a chitosan-based composite used for absorbing heavy metals.

Composites with Chitosan

A 1.5 g to 120 mL solution of chitosan was prepared at a pH of 5 (adjusted by HCl). Pieces of fabric were placed in 40 mL of 0.5 M citric acid and stirred at 800 rpm and 60 °C for 15 minutes. The fibers were then placed in a beaker, mixed with about 20 mL of chitosan solution, and cured with 3 different methods: ultraviolet irradiation for 10 minutes, air-drying, and a heat lamp. After UV curing, the composite exhibited gel-like properties. The air-dried sample, after drying overnight, was considerably stiffer than the originally degraded fibers. Similar effects were achieved by placing the sample under a heat lamp for one hour. The samples were then examined with scanning electron microscopy (SEM), demonstrating that cotton fiber and chitosan blended into a composite.

Cotton-chitosan composites are known to absorb metals^[2]. To test such properties, the heat lamp-dried composites were immersed in 15 mL of 0.01 M potassium dichromate solution for one hour. For comparison, untreated fabric and deweaved fibers (treated with 3:1 mixture of 0.5 M citric acid and 0.5 M sodium nitrate) were also immersed in potassium dichromate solution. Afterward, samples were retrieved from the solutions and dried overnight. X-Ray Fluorescence (XRF) on the three samples revealed that the chitosan composite absorbed three times more chromium than the control untreated fabric and treated deweaved fibers (Figure 1). In the future, samples will be examined using ultraviolet-visible spectroscopy (UV-Vis) and similar experiments will be conducted with lead nitrate.

Synthesizing Silver Nanoparticles

Samples of dried unwoven fibers (treated with 3:1 mixture of 0.5 M citric acid and 0.5 M sodium nitrate) were used for the synthesis of silver nanoparticles in two ways. Both samples were treated with a solution of 20 mL silver nitrate and 2-5 drops of sodium borohydride (until color change was detected). The first sample was placed for 20 minutes at room temperature, while the second sample was ultrasonicated for 20 minutes at 40 °C. Both samples were then air-dried. The silver nitrate solution was then analyzed using UV-Vis spectrometry, showing a peak at 325 nm, which is characteristic of silver nanoparticles^[3]. The samples were then observed with SEM to visualize the size and features of the nanoparticles (Figure 2). The fibers heated in the ultrasonicator showed far more and smaller nanoparticles than the non-heated samples. In addition, a test was run with staphylococcus aureus which showed that the particles are antibacterial (Figure 3).

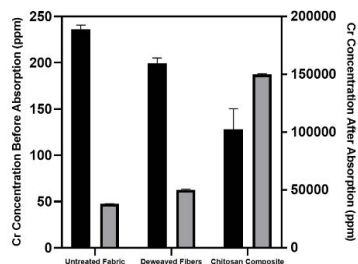


Figure 1. Chromium concentration before (Black) and after (Gray) Absorption in PPM.

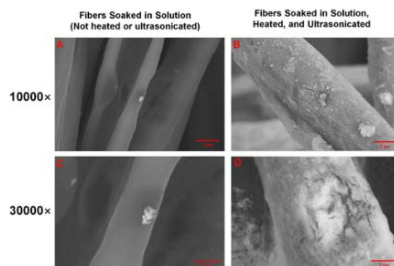


Figure 2. SEM of dewoven fibers and silver nanoparticles synthesized using two different methods.



Figure 3. Two petri dishes coated in *S. aureus* with dewoven fibers. The one on the left a control and the right containing nanoparticles.

^[1] Cuiffo, M., Jung, H.J., Skocir, A. et al. "Thermochemical degradation of cotton fabric under mild conditions." *Fash Text* 8, 25 (2021). <https://doi.org/10.1186/s40691-021-00263-8>

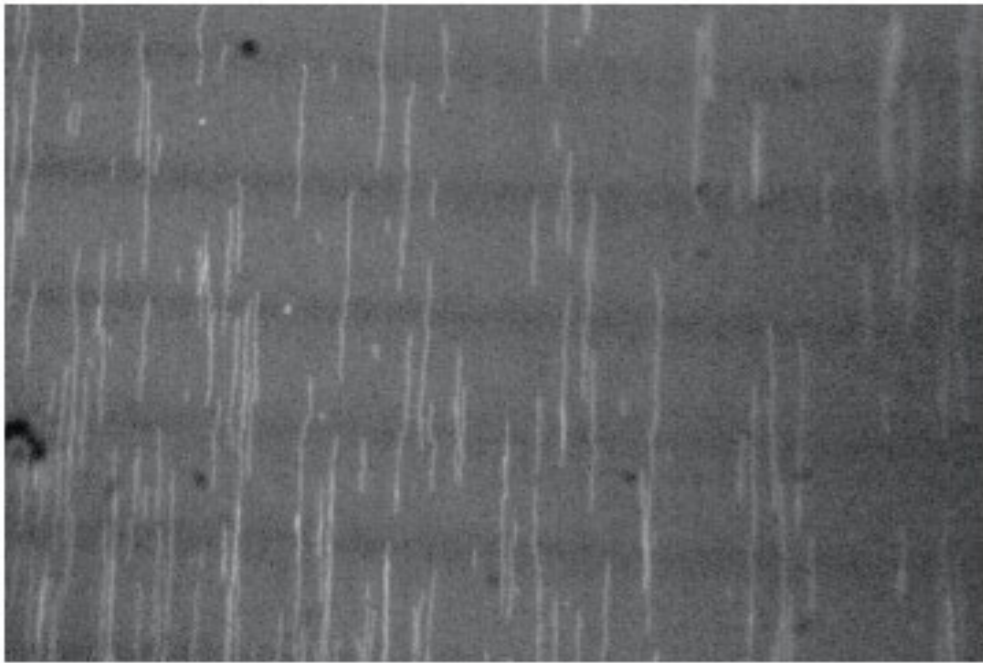
^[2] Alonso-Segura, Diana et al. "The Development and Characterization of a Cotton-Chitosan Composite for Lead Removal from Water." *Polymers* vol. 13,13 2066. 23 Jun. 2021, doi:10.3390/polym13132066

^[3] De Leersnyder, Ilse et al. "High Variability in Silver Particle Characteristics, Silver Concentrations, and Production Batches of Commercially Available Products Indicates the Need for a More Rigorous Approach." *Nanomaterials* (Basel, Switzerland) vol. 10,7 1394. 17 Jul. 2020, doi:10.3390/nano10071394

SESSION IX:

Embolic Agents, DNA, and Backscattering:

Mentors: Robert Wong and Anthony
DeValle



Application of Tn5 Transposase to Surface-immobilized DNA Combed on Grated Polydimethylsiloxane Film

Robin Xiong¹, Hannah Saks², Junzhi Xie³, Leon Zhou⁴, Anthony Del Valle⁵, Jonathan Sokolov⁵

¹Ward Melville High School, East Setauket, NY 11733, ²Walt Whitman High School, Huntington, NY 11743, ³Richard Montgomery High School, Rockville, MD 20852, ⁴Shenzhen Middle School, Luohu District, Shenzhen, Guangdong Province, China, ⁵Department of Materials Science & Chemical Engineering, Stony Brook University, Stony Brook, NY 11794

Since the human genome was first sequenced in 2003, next generation sequencing (NGS) methods have seen widespread use for high-throughput DNA sequencing [1]. Recent development of long-range sequencing (LRS) instruments, such as Pacific BioScience's RS, has enabled ID of contiguous DNA fragments tens of kilobase pairs in length [2]. However, existing LRS methods involve stochastic mixing of DNA in buffer solution, losing information about DNA fragment order and necessitating complex computational reassembly. An alternative method has previously been described to preserve spatial orientation and greatly simplify LRS, where DNA is combed on polymethacrylate (PMMA) thin film and stamped with endonuclease (DNase I) before recovery for sequencing [3].

This study improves on the group's previous work by applying "tagmentation" to surface-immobilized DNA fragments, a process utilizing Tn5 transposase to simultaneously cut and label DNA fragments. This study explores the application of tagmentation to linearly combed, surface immobilized DNAs on grated polydimethylsiloxane (PDMS) film, which may simplify the recovery of spatial information. Application of this method to NGS, such as application to the Illumina flow cell surface, may be a promising area of further study.

PDMS was prepared with 10-parts elastomer, 1-part curing agent. The mixture was poured onto silicon wafers of different gratings spanning approximately 2-8 μm in a petri dish. After curing overnight, the PDMS was peeled off, cut with a razor blade, and placed in a vacuum chamber. Samples were soaked in an ethanol bath overnight to remove unreacted PDMS polymers. To prepare the DNA solution, λ DNA (NEB) was first diluted in Tn5 transposase (TE) buffer to a concentration of 5-50 $\mu\text{m}/\mu\text{l}$. DNA was stained with SyBr Gold for easier visibility under a fluorescence microscope. DNA was deposited onto grating surfaces by dipping the sample in DNA solution and withdrawing at a rate of 2 mm/second using a computer-controlled linear stage. This facilitated DNA stretching by maintaining a constant rate of deposition.

The PDMS samples were then transferred to microscope slides and examined under a Leica microscope under 40x and 63x magnification. In theory, the microscope images would highlight large amounts of bridging across the troughs of the grating and between the channels, allowing the transposase to latch onto the DNA and cut it.

After obtaining a DNA sample with a significant bridging, a few drops (2 μl) of TE buffer were placed in an area with visible bridging under the microscope, trying to minimize evaporation. Testing indicated that a 28% m/v glycerol solution experienced the least evaporation.

DNA was successfully combed onto grated PDMS (Fig. 1), although samples were often inconsistent in linearity and direction. However, Tn5 transposase action was shown to be inconclusive after preliminary testing. Current experimentation suggests that further exploration may yield promising results.

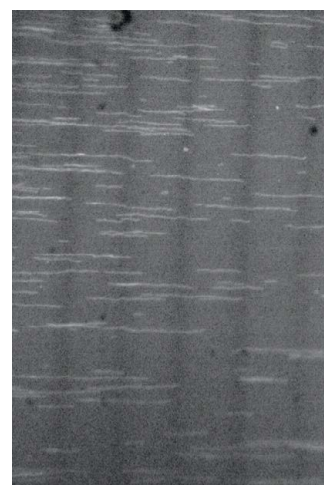


Figure 1: Leica microscope image of DNA with significant bridging

[1] Goodwin, S. et al. (2016). "Coming of age: ten years of next-generation sequencing technologies." *Nat Rev Genet* 17. DOI: <https://doi.org/10.1038/nrg.2016.49>

[2] Quail, M., et al. (2012) "A tale of three next generation sequencing platforms: comparison of Ion Torrent, Pacific Biosciences and Illumina MiSeq sequencers." *BMC Genomics* 13. DOI: 10.1186/1471-2164-13-341

[3] Cho, N., et al. (2017). "Fragmentation of Surface Adsorbed and Aligned DNA Molecules using Soft Lithography for Next-Generation Sequencing." *J Biosens Bioelectron* 8(3). DOI: 10.4172/2155-6210.1000247

Observation of Coherent Backscattering for Detection of Physical State Changes

Claire Yang¹, Dr. Eric Jones², Dr. Martin Cohen³, Professor Harold Metcalf⁴

¹ Ward Melville High School, East Setauket, NY 11733, ²Laser Teaching Center, Stony Brook University, Stony Brook, NY 11794 ^{3,4} Department of Physics and Astronomy, Stony Brook University, Stony Brook, NY 11794

Observation of light scattering is an innovative tool in studying quantum optics, optical materials, and photon localization. Coherent backscattering (CBS) of light is an interference phenomenon that is observed when light rays propagate through random media where the particle size is comparable to the wavelength of the incident light. Light incident on such media can be scattered multiple times by its constituent particles. When two light rays follow time-reversed scattering paths, they interfere constructively only in the backscatter direction, causing an enhanced intensity cone with twice the magnitude as the incident light (Fig. 1; CBS signal). Coherent backscattering is considered “weak localization”, a precursor to the strong localization predicted by Anderson localization, and is reliant on the relationship between the transport mean free path and the scattering mean free path within the medium, key characteristics of the physical state of a scattered media. Thus, CBS has been used recently to detect the denaturation of milk caused by protein aggregation². CBS then has application in detection of physical state changes, where the size of and distance between the scattering centers of the medium change.

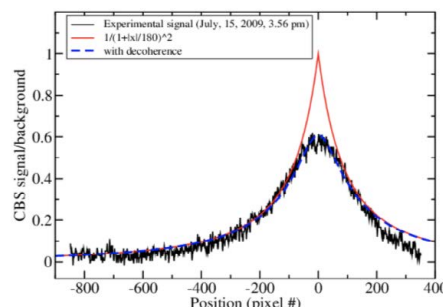


Figure 1. A typical CBS signal with the characteristic twice enhanced intensity peak. Experimentally detected signals are typically less acute due to residual scattered light¹.

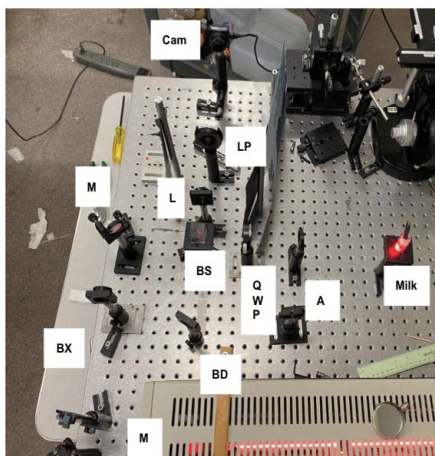


Figure 2. Optical alignment used. M-Mirror; BX- Beam expander (4x); BS- Beam splitter; L- Lens (f = 40cm); LP- Linear Polarizer; QWP- Quarter Wave Plate; BD- Beam Dump; A- Aperture

The experimental setup utilized to detect the CBS signal is displayed in Figure 2. Here, a sample of milk is used for initial detection, as milk’s scattering and suspension properties make it an ideal candidate for detecting the backscatter signal. Once the optical alignment is perfected, the sample can be easily swapped or manipulated. To improve the angular resolution of the apparatus, the laser beam diameter is quadrupled using a beam expander. The CBS signal will follow back along the incident laser path, which is then split at the beam splitter so that a portion of the light can be imaged by the CMOS camera. Detection of the signal is complicated by the presence of stray light, which can be eliminated by blocking any possible back reflections or diffuse light through careful stacking and placement of neutral density (ND) filters. Due to the faint nature of the CBS signal, detection with the CMOS camera requires subtraction of the background signal through image post-processing.

Coherent backscattering remains a promising method to detect physical state changes of random, scattered media. Future studies can further investigate the CBS signal’s response to physical state changes by adjusting the density, concentration, and content of the scattered media, and the detection apparatus can be further applied to assess protein denaturation in vaccines or reflectivity in materials, providing an innovative way to detect physical state changes and characterize physical properties.

¹ Müller, Cord, Delande, Dominique. (2010). Disorder and interference: localization phenomena. 10.1093/acprof:oso/9780199603657.003.0009.

² Verma, M., Singh, D. K., Senthilkumaran, P., Joseph, J., & Kandpal, H. C. (2014). Ultrasensitive and fast detection of denaturation of milk by Coherent backscattering of light. Scientific Reports, 4(1). doi:10.1038/srep07257.

Optimizing Brain Aneurysm Treatment with a Reverse Thermo-Responsive Liquid Embolic Agent

Ifeoluwatobi Alao^{1*}, Jessica Guo^{2*}, Matt Lim^{3*}, Chiara Mosca^{4*}, Hannah Tao^{5*}, Maya Vendhan^{6*}, Harriet Zu^{7*}, Aryan Roy^{8*}, Megha Gopal⁹, Varun Nimmagadda¹⁰, Tyler Shern¹¹, Robert Wong⁹, Miriam Rafailovich⁹

¹High Technology High School, Lincroft, NJ, 07738, ²Ward Melville High School, East Setauket, NY, 11733, ³Plainview-Old Bethpage JFK High School, Plainview, NY, 11803, ⁴East Islip High School, Islip Terrace, NY, 11752, ⁵Academy for Information Technology, Scotch Plains, NJ, 07076, ⁶Colorado Academy, Denver, CO, 80235, ⁷High School Affiliated to Renmin University of China, Beijing, China, ⁸Cherry Creek High School, Denver, CO, ⁹Department of Materials Science and Chemical Engineering, Stony Brook University, NY, 11790, ¹⁰University of Michigan, Ann Arbor, MI, 48109, ¹¹Columbia University, New York, NY, 10027

*Authors 1-8 contributed equally to this work

Brain aneurysms are weak-walled pathological dilations occurring at cerebral vasculatures. If left untreated, they can easily rupture, resulting in stroke or even death. Most of the current treatments show unfavorable primary outcomes in 20% to 30% of cases.^[1, 2] Therefore, the project goal is to optimize treatment by developing an injectable, reverse thermo-responsive, crosslinkable, shape-conforming, and biodegradable polymer system with proper mechanical strength and patient-specific healing as a novel treatment of brain aneurysms.

To synthesize the gel for the polymer system, Pluronic F127-DMA and F88-DMA were utilized because of their easy injectability, ability to form a physical gel at physiological temperatures, and crosslinking ability to form a strong, stable gel. The polymer solution was mixed with a catalyst (ammonium persulfate (APS), ascorbic acid, FeCl₂), water, and optionally, a contrast solution. Rheology was conducted to determine the gel's elastic modulus using a Bohlin Gemini 150 HR Nano rheometer via single-frequency time and amplitude sweeps.

With an expected crosslinked modulus of 200 kPa, there was significant trouble initiating sufficient crosslinking. To evaluate the APS as a possible problem, different concentrations and stocks of APS were used. Results indicated that the APS was likely not the problem and that the minimum APS amount needed to achieve a similar level of crosslinking at high concentrations was 30 mg. Subsequently, water solvents of different pH, water contamination, and the FeCl₂ component in the catalyst were investigated, but these also yielded little variation. An experiment was then run using two samples: one using the same F127-DMA from the previous experiments and one using F127-DMA from a previous stock (acquired around May)—the water and catalyst were kept constant (**Fig. 1**). The new F127-DMA only reached ~60% efficiency but began at a higher value. A similar trend was seen in the F88-DMA data, with the old sample reaching 143.47 kPa and the new sample reaching 75.2 kPa. It was concluded that the new polymer batch was the problem in the experiment, likely due to contamination. To briefly evaluate the relationship between polymer concentration and modulus, several early F88-DMA amplitude sweeps were plotted, resulting in a general positive correlation (**Fig. 2**). When testing fibrinogen adhesion to gel surfaces and imaging with the EVOS FL cell microscope, only F88 without and with fibrinogen yielded some minimal spots, likely due to fibrinogen contamination and ineffective adhesion, respectively. When testing fibrin formation on gel surfaces, both F88 with fibrinogen and F127 with fibrinogen yielded fibrinogen clumps but no fibrin, which would be indicated by the presence of strand-like structures. Since the gel was confirmed by this to not be thrombogenic, it is promising for future applications. One injection experiment was completed by injecting the known faulty F88 gel (35% before catalyst) into an animal model. The gel remained localized in the vessel upon injection; it did not dissolve in the water but only crosslinked to some extent, making it unable to block water flow. However, the trial was still a positive indication that this concentration with the injection experiment functions as expected.

While improvement is needed to further develop F127-DMA and F88-DMA as a brain aneurysm treatment, the polymers show potential. In the future, before moving to *in vivo* testing, additional components will be incorporated and optimized that would allow the polymer to promote endothelialization and biodegrade when triggered by patient-specific, naturally occurring enzymatic activity.

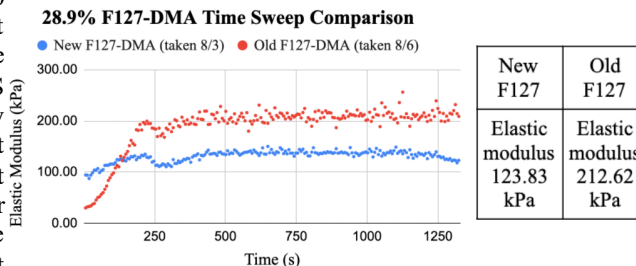


Figure 1: Time sweep and elastic modulus of old and new F127-DMA batches, at concentration 28.9%.

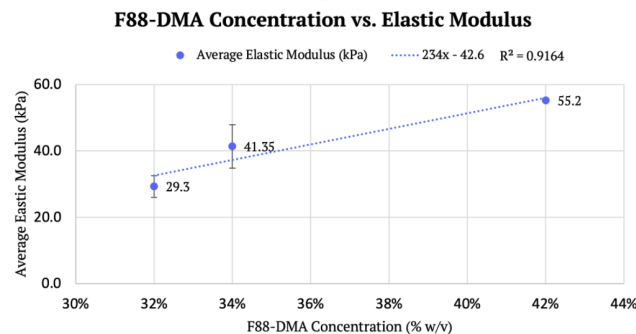


Figure 2: F88-DMA concentration vs. elastic modulus and linear regression model. Note: Since these data were taken with the faulty gel in its non-crosslinked state, they are lower than the actual cross linked modulus; however, the positive correlation remains.

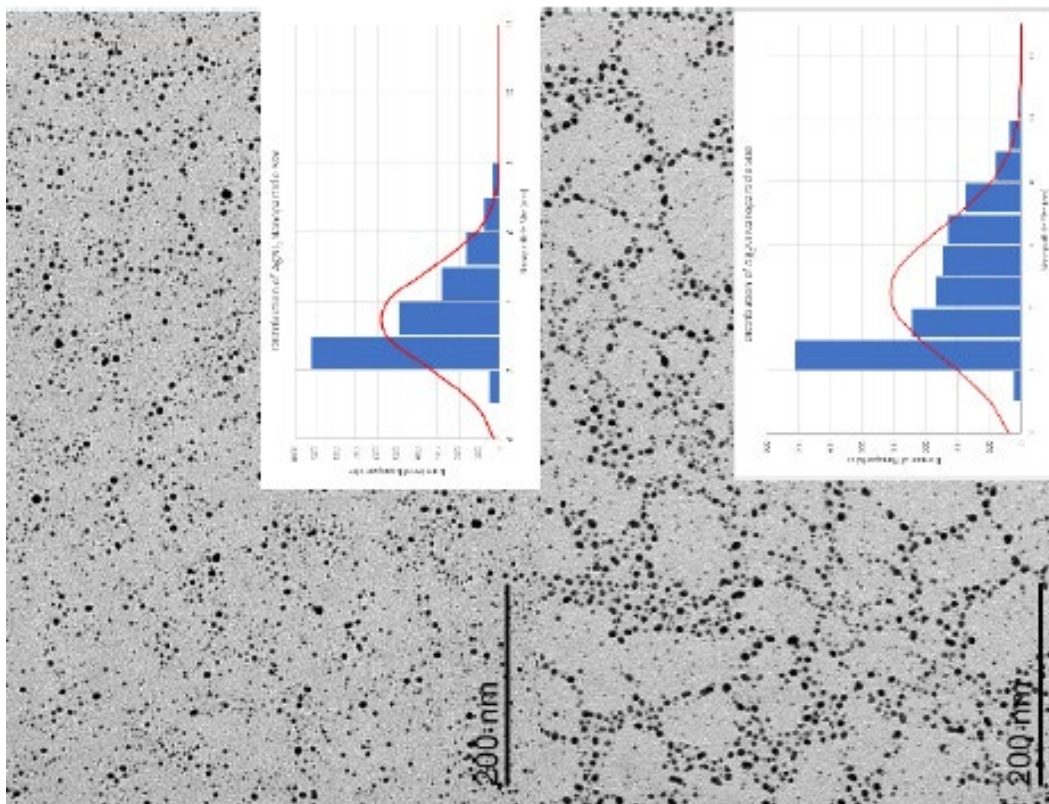
¹ Taschner CA, Chapot R, Costalat V, Machi P, Courtheoux P, Barreau X, et al. Second-Generation Hydrogel Coils for the Endovascular Treatment of Intracranial Aneurysms: A Randomized Controlled Trial. *Stroke*. 2018;49(3):667-74.

² Adeeb N, Moore JM, Wirtz M, Griessenauer CJ, Foreman PM, Shallwani H, et al. Predictors of Incomplete Occlusion following Pipeline Embolization of Intracranial Aneurysms: Is It Less Effective in Older Patients? *AJNR Am J Neuroradiol*. 2017;38(12):2295-300.

SESSION X:

Sustainable Energy

Mentors: Aniket Raut, Haoyan Fang, Yifan Yin, and Dr. Yuchen Zhou



Use of Partially Reduced Graphene Oxide to Increase Power Efficiency in AEM Fuel Cells

Miriam Rafailovich¹, Rebecca Isseroff¹, Aniket Raut¹, Haoyan Fang¹, John Calderon¹, Andrew Ahn², Abhinav Madabhushi³, Eyal Noy⁴, Audrey Zhan⁵, Alex Zhang⁶, Alan Zhu⁷

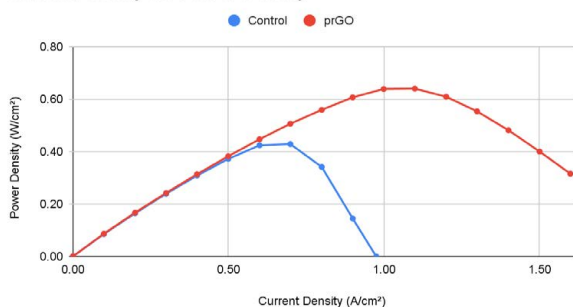
¹Stonybrook University, ²Fayetteville-Manlius High School, ³Chirec International School, ⁴Rochelle Zell Jewish High School, ⁵Westminster School, ⁶Newton North High School, ⁷Livingston High School

With the increasing concerns of overall energy consumption, researchers have been devoted to energy efficiency enhancement for long. Fuel cells, as an electrochemical facility that transfers chemical energy to electrical energy, have a fairly broad application in different industries. Among them, the alkaline anion exchange membrane fuel cell (AEMFC) is of promising potential, but necessitates platinum usage. Although the exploitation of platinum nanoparticles (NPs) is essential for catalysing oxygen reduction reactions, the high cost of Pt NPs manufacturing has been a critical obstacle for the AEMFC's wider application. This work examines the increase in power density of AEMFCs when we apply partially reduced graphene oxide (prGO) nanoparticles on the membrane. Given that the prGO can increase ion conduction while protecting the platinum catalyst on the gas diffusion layer, we expect to see an increment in power density output, which further leads to a platinum usage reduction in AEMFC without compromising power production.

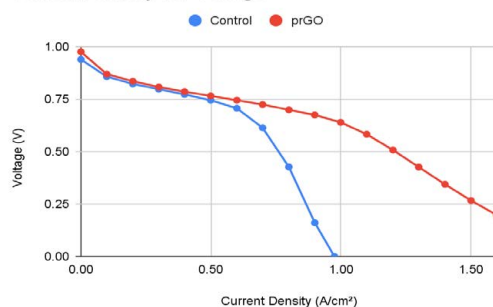
The prGO was prepared by placing 1.0 g graphite in 24 mL of 98% sulfuric acid, sonicating it, and stirring in 0.5 g sodium nitrate. While maintaining a temperature of 10°C, potassium permanganate was added. After slow heating and dilution, the solution was treated with 3% hydrogen peroxide and filtered through a glass filter funnel. Then, the precipitate was dispersed in 5 mL 37% hydrochloric acid, filtered, dispersed in water, filtered again, and then dehydrated at 45°C for 24 hours in a vacuum oven.

The control group had a 5 cm² active area of Sustainion[®] X37-50 grade RT membrane with 0.76 mg/cm² Pt nanoparticle catalyst, and the maximum power density of control is 0.42 W/cm². In the experiment group, an additional 1 µg/cm² prGO was added, which generated a maximum power density of more than 0.60 W/cm². This result exhibits the feasibility of reaching higher AEMFC power density output by adding a very small amount of low-cost prGO. Encouraged by the optimistic improvement potential of AEMFC, we have faith in its contribution to more efficient energy generations. For future researches, we will focus on the effect of adding GO reduced with AgNO₃ (1 mmol of AgNO₃ in prGO) to AEM fuel cells and the potential help in power efficiency enhancement.

Current Density vs. Power Density



Current Density vs. Voltage



Figures 1 & 2 (above): Polarization curves comparing the control with the experimental prGO cells

The Enhancement of AEMFCs using Bimetallic Ag₃Ni and AgNi₃ Nanoparticles

By: Andrew Ahn¹, Abhinav Madabhushi², Eyal Noy³, Audrey Zhan⁴, Alex Zhang⁵, Alan Zhu⁶, John Calderon⁷, Aniket Raut⁷, Haoyan Fang⁷, Miriam Rafailovich⁷

¹Fayetteville-Manlius High School, Manlius, New York 13104; ²Chirec International School, Sri Ram Nagar, Kondapur, Telangana 500084, India; ³Rochelle Zell Jewish High School, Deerfield, Illinois 60015; ⁴Westminster School, London, England SW1P 3PF; ⁵Newton North High School, Newton, Massachusetts 02460; ⁶Livingston High School, Livingston, NJ 07039; ⁷Stony Brook University, Stony Brook, New York 11794

The search for sustainable energy has shifted much research from proton exchange membrane fuel cells (PEMFCs) using a platinum catalyst to anion exchange membrane fuel cells (AEMFCs) with cheaper, more abundant metal catalyst alternatives. Prior research has already been conducted finding that nickel is a strong catalyst for the oxygen reduction reaction (ORR). Nickel alloys with zinc, molybdenum, and copper further improved the catalytic activity in AEMFCs¹. In our research, we continued investigating the efficiency of nickel alloy catalysts and tested two silver-nickel bimetallic nanoparticles, Ag₃Ni and AgNi₃. This work examines the change in power density of AEMFCs from two variables. First is the difference in size and mass of the bimetallic nanoparticles. Second is the application of the nanoparticles onto the anion exchange membrane, whether it was using a Point Zero Airbrush or a Langmuir-Blodgett Trough.

The nanoparticles were synthesized using the Brust method on AgNO₃ and Cl₂H₁₂NiO₆ with octanethiol in a 3:1 and 1:3 ratio. To find the optimal pressure to layer the nanoparticles onto the anion exchange membrane, an LB trough was used to graph the isothermal curves for both nanoparticles. From the isothermal curve, it was determined that both the AgNi₃ and Ag₃Ni nanoparticles began to form a monolayer at around 2 mN. The last step before testing was to determine the difference in size between Ag₃Ni and AgNi₃. The nanoparticle distribution for both Ag₃Ni and AgNi₃ was captured using transmission electron microscopy (TEM). The images were analyzed using ImageJ software and graphed in histograms depicting the size distribution and normal distribution curve of the nanoparticles (Figures 1 & 2). The data shows that the Ag₃Ni nanoparticles had a larger size range and a larger size in general.

The control group consisted of an AEMFC with a 5 cm² active area Sustainion membrane and 0.76 mg/cm² platinum catalyst. This produced a maximum power

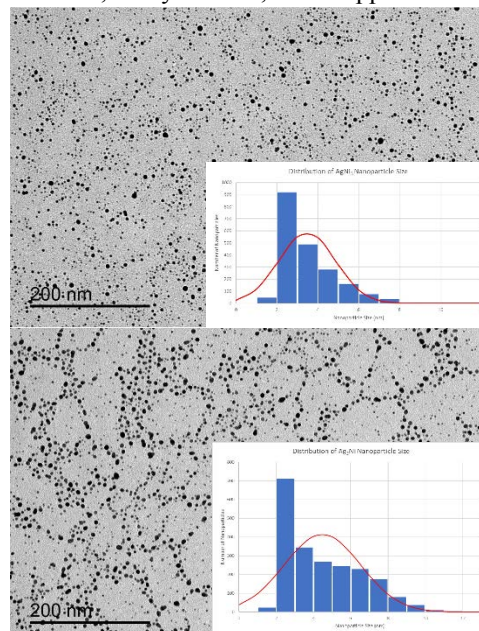


Figure 1 & 2 (above): TEM images and Histograms of AgNi₃ and Ag₃Ni Nanoparticles

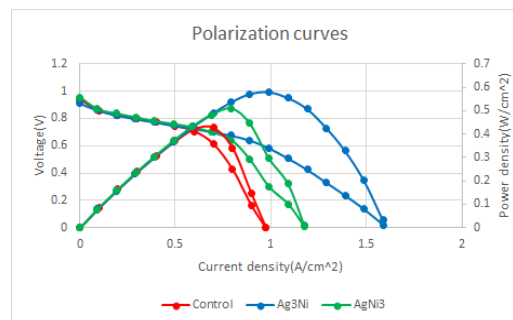
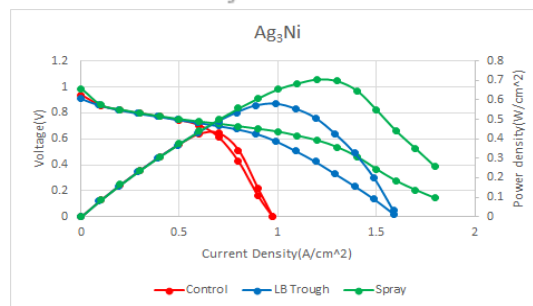


Figure 3 (left): Polarization curves comparing control, Ag₃Ni, and AgNi₃

Figure 4 (right): Polarization curves comparing control, spray using Point Zero Airbrush, and deposition using LB Trough



density of 0.42 W/cm². Sustainion membranes for each of the test variables were then prepared. Using the LB trough set to maintain 2 mN of surface pressure, a monolayer of Ag₃Ni was placed on both sides of a membrane and the process was repeated for AgNi₃. Using the area of Under the same control with a 5 cm² active area and 0.76 mg/cm² of platinum loading, AgNi₃ and Ag₃Ni both outperformed the control group with maximum power densities of 0.51 W/cm² and 0.58 W/cm² respectively (Figure 3). Thus, the larger and heavier 3:1 ratio of silver to nickel is the more efficient catalyst. For the sprayed nanoparticles, the mass of nanoparticles was kept the same as with the LB trough. A point Zero Airbrush was used to spray the nanoparticles onto both sides of a Sustainion membrane. Ag₃Ni gave significantly higher results when the nanoparticles were sprayed randomly compared to when monolayers were formed on the membrane with maximum power densities of 0.58 W/cm² and 0.71 W/cm² respectively (Figure 4). The performance of AgNi₃ when sprayed vs. deposited using an LB trough has not been tested yet. However, we expect it to follow in a similar pattern as Ag₃Ni with a maximum power density slightly under 0.71 W/cm².

With this research done on silver-nickel nanoparticles, AEMFCs are taking another big step towards widespread use. The current results indicate that the very cheap to produce Ag₃Ni nanoparticles, when sprayed onto a Sustainion membrane using a commercial airbrush, can provide a 169% increase in power density. The ease of access and sustainability of this procedure are sure to alter the direction of AEMFCs in future markets.

¹Aaron Roy. 2017. Anodic Catalysts for Anion Exchange Membrane Fuel Cells. [Madison(WI)]: University of Madison-Wisconsin

Optimization of Membrane Electrode Assembly Using Silver Nanoparticles in Anion Exchange Membrane Fuel Cells

Andrew Ahn¹, Abhinav Madabhushi², Eyal Noy³, Audrey Zhan⁴, Alex Zhang⁵, Alan Zhu⁶, John Calderon⁷, Aniket Raut⁷, Haoyan Fang⁷, Miriam Rafailovich⁷

¹Fayetteville-Manlius High School, Manlius, NY 13104; ²Chirec International School, Hyderabad, Telangana 500084, India; ³Rochelle Zell Jewish High School, Deerfield, IL 60015; ⁴Westminster School, Simsbury, CT 06070; ⁵Newton North High School, Newton, MA 02460;

⁶Livingston High School, Livingston, NJ 07039; ⁷Stony Brook University, Stony Brook, NY 11794

Recent climate change concerns have led to the desire for more sustainable energy sources, and fuel cells have demonstrated potential to be strong contenders in alternative clean energy. Among them, anion exchange membrane fuel cells (AEMFCs) have shown promise in being able to mitigate one of the primary drawbacks of fuel cell technology: cost. Platinum catalyst is required in AEMFCs due to the slow nature of the power-generating oxygen reduction and hydrogen oxidation reactions [1], but platinum's high cost has hindered widespread application of AEMFCs. It is thus crucial for the actuation of AEMFC potential in the energy industry for alternative catalysts to be investigated. As such, prior research has found that silver (Ag) exhibits similar catalytic properties to platinum in AEMFCs [2]. This work seeks to investigate the optimal size of Ag nanoparticles sprayed onto the membrane electrode assembly of AEMFCs for maximum AEMFC performance enhancement; through this, we seek to effectively decrease platinum content, thus cost, of the fuel cell without compromising power generation.

In order to find the optimal Ag nanoparticle size, the performance of AEMFCs modified with different Ag nanoparticle sizes were compared to each other and a control. The control to set a benchmark performance was an AEMFC with a Sustainion® X37-50 Grade RT membrane that had not been sprayed with Ag nanoparticles, with an active area of 10cm² and a platinum concentration of 0.5mg/cm². Ag nanoparticles were synthesized with either hexanethiol (C₆) or octanethiol (C₈) using the Brust nanoparticle synthesis method. Either Ag C₆ (Fig.1) or Ag C₈ (Fig.2) nanoparticles were then sprayed with a commercial airbrush onto both sides of the membrane of one of two identical AEMFCs (same specifications as control). These three AEMFCs were subsequently tested for power generation. The control AEMFC reached a peak power density of 0.300W/cm². 1 µg/cm² of AgC₆ nanoparticles sprayed onto the membrane of the AEMFC resulted in a peak power density of 0.440 W/cm², a 47% increase in performance, and 1 µg/cm² of AgC₈ nanoparticles sprayed onto the membrane of the AEMFC resulted in a slightly lower peak of 0.434 W/cm², a 45% increase in performance over the control (Fig.3). In addition, it is important to note that Ag C₆ reached max power output at 0.573 volts, while Ag C₈ reached it at 0.525 volts and the control reached it at 0.674 volts. In the future development of this work, we plan on testing Ag C₁₀ (Fig.4) nanoparticles in addition to more tests of the Ag C₆ and Ag C₈ nanoparticles. The results will be compared with the other thiol lengths and the control to determine the optimum thiol length for AEMFCs that will reduce platinum usage and fuel cell cost to increase the accessibility of AEMFC technology in the future.

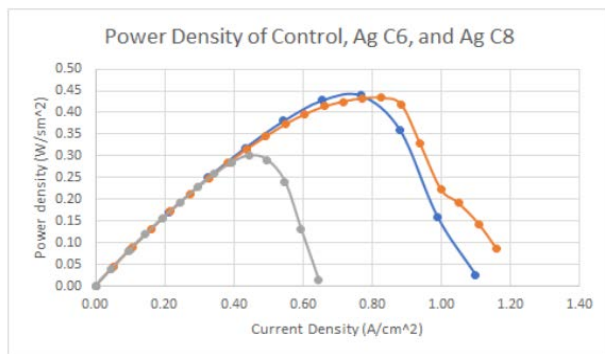
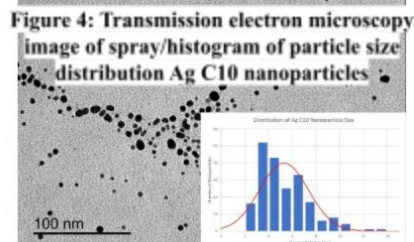
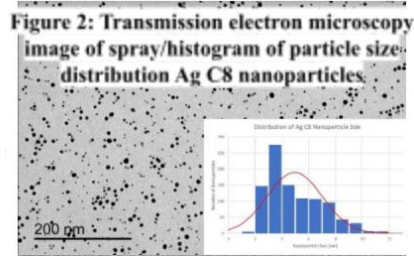
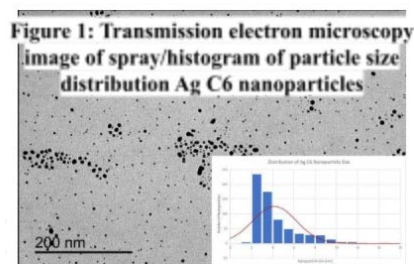


Figure 3: Power Output of AEMFCs With Ag C6 (blue), Ag C8 (orange), and no silver nanoparticles (gray).

¹Larminie, J., & Dicks, A. (2003). *Fuel cell systems explained*. John Wiley & Sons, Ltd., <https://doi.org/10.1002/9781118878330>

²Erikson, H., Sarapuu, A., & Tammeveski, K. (2018). Oxygen reduction reaction on silver catalysts in alkaline media: A minireview. *ChemElectroChem*, 6(1), 73-86. <https://doi.org/10.1002/celec.201800913>

Polymeric hole transport layer in perovskite solar cells

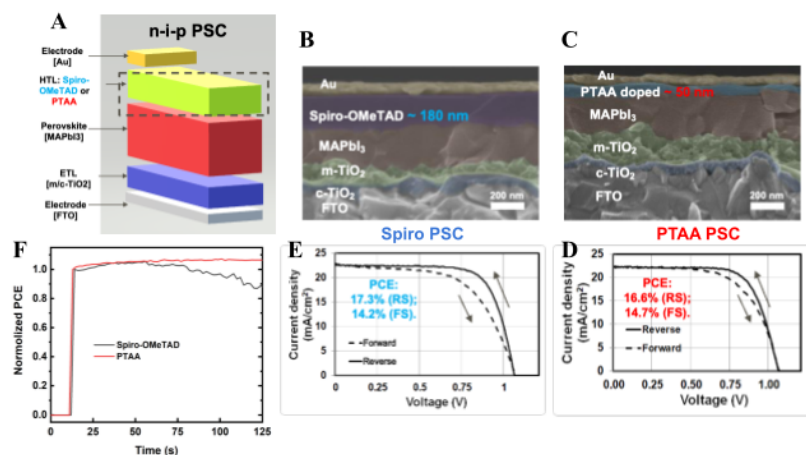
Miller Liao¹, Grace Kyoko Wong², Yifan Yin³, Yuchen Zhou³, Miriam Rafailovich³

¹Shenzhen Middle School, Shenzhen, China, ²St Paul's Girls' School, London, UK, ³Stony Brook University, NY 11794

Perovskite solar cells (PSC), which have experienced rapid development since they were first constructed in 2009, have become one of the most promising types of next-generation solar cell. In the past, PSCs with a Spiro-OMeTAD hole transport layer (HTL) have been shown to have poor device stability and current-voltage hysteresis in photovoltaic (PV) performance¹⁻³. In our study, we used PTAA as a substitute for Spiro-OMeTAD and compared the PV parameters along with the device stability of both PSCs. The PSC with Spiro-OMeTAD showed a power conversion efficiency (PCE) of 17.3% in reverse scan (RS) and 14.2% in forward scan (FS), while the PSC with doped PTAA had a PCE of 16.6% in RS and 14.7% in FS. Moreover, the continuous maximum power point (MPP) test in an ambient environment (humidity $\sim 70\%$) showed that the PTAA based PSC presented a more stable output compared to the Spiro-OMeTAD based PSC. Through our study, we suggest that the higher hydrophobicity of the PTAA, as compared to the Spiro-OMeTAD, could be the determining factor in improving its stability when exposed to high temperatures and humidity.

To compare the parameters between doped PTAA cells and Spiro-OMeTAD cells, we built up the regular structured device with FTO/c-TiO₂/m-TiO₂/MAPbI₃/HTL/Au (Fig. A). Three different hole transport layers were prepared via spinning : undoped PTAA, Li-TFSI doped PTAA and Spiro-OMeTAD. From the cross-section images using scanning electron microscopy (SEM), we found the Spiro-OMeTAD layer had a thickness of around 180 nm, while the thickness of the PTAA layer was around 50 nm (Figs. B and C). In addition, the doping of Li-TFSI did not change the thickness of the PTAA layer. The data for the current density-voltage curves were collected using a PV test station with a Xenon solar lamp. Although the Spiro-OMeTAD based PSC showed a slightly higher PCE in RS, the sample showed a greater hysteresis in comparison to the PTAA based one (Figs. D and E). The continuous MPP test in the ambient environment showed that the PCE of Spiro-OMeTAD based PSC started to drop within one minute, while the PTAA based PSC maintained a stable performance over a 2-minute scan (Fig. F). The hydrophobicity of the HTL was determined by measuring the water contact angle. The Spiro-OMeTAD film showed a contact angle of 69.8° and the PTAA film showed a contact angle of 88.2°, suggesting that the PTAA was more hydrophobic than the Spiro-OMeTAD. This may explain the improved stability of the

PTAA device.



Figures: (A) Structure of the PSCs; Cross-section SEM images of (B) Spiro PSC and (C) PTAA PSC, respectively; J-V curves of (D) Doped PTAA PSC and (E) Spiro PSC, respectively; (F) Continuous PCE of doped PTAA and Spiro-OMeTAD cells.

¹Kim, Jincheol; Park, Nochang; Yun, Jae S.; Huang, Shujuan; Green, Martin A.; Ho-Baillie, Anita W. Y. "An effective method of predicting perovskite solar cell lifetime-Case study on planar CH₃NH₃PbI₃ and HC(NH₂)₂PbI₃ perovskite solar cells and hole transfer materials of spiro-OMeTAD and PTAA." *Solar Energy Materials and Solar Cells*, vol. 162, April 2017.

²Mesquita, Isabel; Andrade, Luísa; Mendes, Adélio. "Temperature Impact on Perovskite Solar Cells Under Operation." *ChemSusChem*, vol. 12, issue 10, 21 May 2019.

³Wu, Bo; Fu, Kunwu; Yantara, Natalia; Xing, Guichuan; Sun, Shuangyong; Sum, Tze Chien; Matthews, Nripan. "Charge Accumulation and Hysteresis in Perovskite-Based Solar Cells: An Electro-Optical Analysis." *Adv. Energy Mater.*, vol. 5, issue 19, 7 October 2015.

Methylammonium Chloride Assisted Growth of High Quality FAPbI₃

Shiqi Cheng¹, Adin Moskowitz², Justin Shnayder³, Yifan Yin⁴, Yuchen Zhou⁴, Miriam Rafailovich⁴

¹Illinois Mathematics and Science Academy, Aurora, IL 60506, ²Hebrew Academy of Nassau County, Uniondale, NY 11553 ³Staten Island Technical High School, Staten Island, NY 10306, ⁴Department of Materials Science & Engineering, Stony Brook University, Stony Brook, NY 11794

As greenhouse gas emissions rise, solar cells, devices which convert sunlight into electricity through the photovoltaic effect, are regarded as a promising solution to the issue. However, the conventional silicon design is costly for commercial use. The use of perovskite as an alternative material has been investigated as it is both cost-effective and demonstrates similar efficiencies to its silicon counterpart [1]. The perovskites used as the photoactive layer in perovskite solar cells (PSCs) have an organic-inorganic halide structure ABX₃, with A indicating an organic cation, B indicating a metal cation, and X indicating a halide anion. Formamidinium lead iodide (FAPbI₃) and methylammonium lead iodide (MAPbI₃) are the two commonly used hybrid perovskites; while FA perovskites are favourable for optimal conversion efficiencies, their comparatively worse morphology makes them vulnerable to degradation. Previous studies have indicated that addition of methylammonium chloride (MACl) into the FAPbI₃ system can help improve the crystallinity and morphology of FAPbI₃ films [2]. Thus, the objective of this study was to develop a high quality FAPbI₃ film with reasonable photovoltaic efficiency by doping pristine-FA with varying concentrations of MACl (15%, 30%, and 45%).

The PSCs were prepared by spin casting c-TiO₂ and m-TiO₂ onto FTO glass followed by annealing in between the deposition of each substance to form the electron transport layer. Then, the substrates were transferred into the Ar-filled glove box. MA and FA perovskite precursors were spun casted onto separate substrates, followed by the dripping of the anti-solvent during spinning. Spiro-OMeTAD was then coated onto the device using spin-casting to form the hole transport layer. Finally, Au electrodes were deposited using physical vapor deposition (PVD).

Compared to pristine-FA, the FA-MACl samples featured larger average grain sizes in scanning electron microscopy (SEM) images (Figure 1A-B). While FA doped with 15% MACl and 45% MACl yielded imperfections such as rough patches, the 30% MACl yielded optimal results with large and compact grains. Further analysis revealed that FA doped with 30% MACl formed grains that were on average ~820 nm in size, double that of the MAPbI₃ grains which were on average ~370 nm in size. Afterwards, an analysis of photovoltaic performance was conducted. The reverse and forward scan of the pristine-FA revealed PCEs of 12.3% and 8.1% respectively (Figure 1C). Conversely, the reverse and forward scans of the FA with 30% MACl revealed high PCEs of 16.5% and 16.4% respectively. The improved PCE and negligible hysteresis from FA-based device indicates the improvement of the crystallinity and quality of the perovskite films, which was further confirmed with XRD analysis: pure FAPI exhibited a dominant photo-inactive δ -phase, and the addition of MACl (particularly at concentrations of >30%) increased the photo-active α -phase and reduced the photo-inactive δ -phase (Figure 1D). Last, UV-vis data revealed that FA perovskites have broader absorption spectra than that of MA perovskites (onset wavelength of ~780 nm compared to <750 nm) and that the addition of MACl did not affect this figure (Figure 1E). In conclusion, our data confirmed that addition of MACl as an additive, particularly at a concentration of 30%, produced a high quality FAPbI₃ film with high photovoltaic efficiency and low hysteresis.

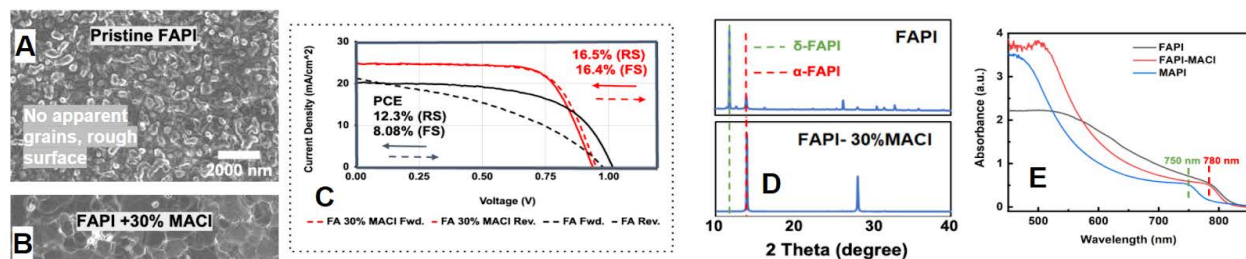


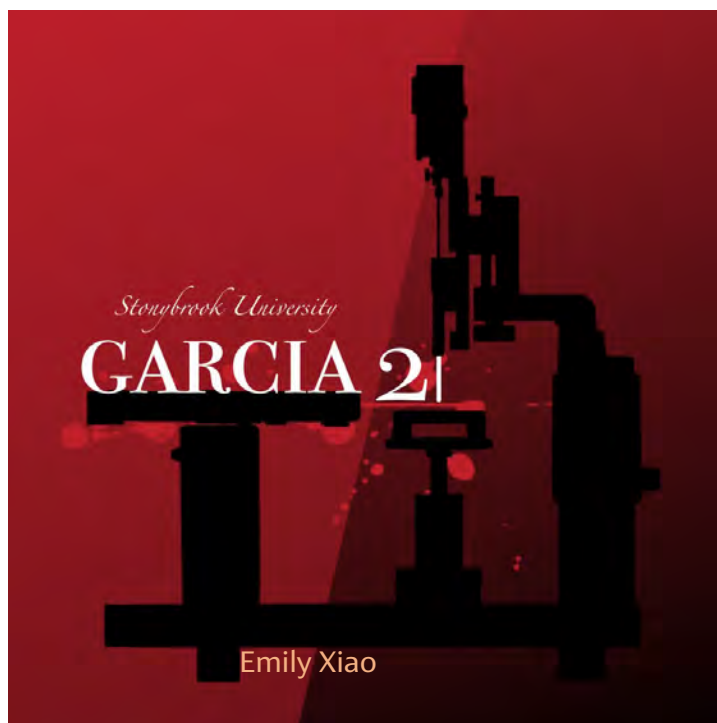
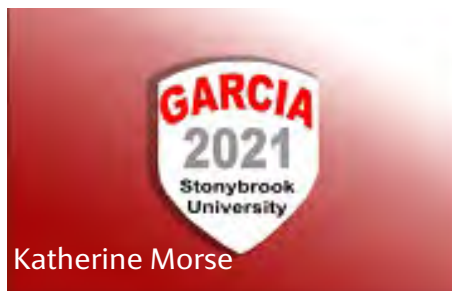
Figure 1: SEM image of the surface morphology of (A) FAPI with 30% MACl and (B) FAPI, respectively; (C) J-V curves of PCE of pristine-FAPI and FAPI with 30% MACl; (D) XRD analysis of pristine-FAPI and FAPI with 30% MACl; (E) UV-vis of MAPbI₃, FAPI, and FAPI-MACl.

¹Tang, H., He, S. & Peng, C. "A Short Progress Report on High-Efficiency Perovskite Solar Cells." *Nanoscale Res Lett* 12, 410 (2017). <https://doi.org/10.1186/s11671-017-2187-5>

²Kim, M., Kim, G., Lee, T.O., Choi, I., Choi, H.W., Jo, Y., Yoon, Y.J., Kim, J.W., Lee, J., Huh, D., Lee, H., Kwak, S., Kim, J., & Kim, D. (2019). Methylammonium Chloride Induces Intermediate Phase Stabilization for Efficient PSCs. *Joule*, 3, 2179-2192.



My designs include silhouettes of the Rudolph Research Auto El Ellipsometer and the Optical Contact Angle Goniometer, representing the polystyrene experiment from the beginning of the program. -Emily Xiao



In Acknowledgement



Jessica Hofflich, Editor



*David R-S
Videography
Consultant*



A wonderful time for all

**the Louis Morin Charitable
Trust for generous support**

Farewell to;



*Dr. Kao Li
who is returning
to China*



*Our hope: Virtual
communication,
Pandemic, Social
Distancing etc .*

We hope to see you in person next year!